5-2016

Model validation and transition to turbulence in orbiting culture dishes.

Jonathan Michael D. Thomas
University of Louisville

MODEL VALIDATION AND TRANSITION TO TURBULENCE IN ORBITING
CULTURE DISHES

By

Jonathan Michael D Thomas

B.S., University of Louisville, 2006

M.Eng., University of Louisville, 2007

A Dissertation Submitted to the Faculty of the J. B. Speed School of Engineering of the

University of Louisville in Partial Fulfillment of the Requirements of the Degree of

Doctor of Philosophy

In Chemical Engineering

Department of Chemical Engineering

University of Louisville

Louisville, KY

May, 2016

MODEL VALIDATION AND TRANSITION TO TURBULENCE IN ORBITING
CULTURE DISHES

By

Jonathan Michael D Thomas

B.S., University of Louisville, Louisville, KY, 2006

M.Eng., University of Louisville, Louisville, KY, 2007

A Dissertation Approved on

April 19, 2016

By the following Dissertation Committee:

_____
R. Eric. Berson (Dissertation Director)

_____
M. Keith Sharp

_____
Yongsheng Lian

_____
Joel Fried

_____
Xiaoan Fu

DEDICATION

This dissertation is dedicated to my amazing mother

Mrs. Glenda Thomas

My mother has been supportive of this endeavor since the beginning. She provided continuous moral support along the way and was there to provide whatever assistance possible when the work was not progressing well. Without her assistance, completion of this work would not have been possible.

ACKNOWLEDGEMENT

First I would like to thank God for all his help through my research and writing.

Dr. Berson's guidance as my PhD advisor has helped immensely with my dissertation progress and my growth as a person and researcher.

Dr. Sharp's knowledge of fluid dynamics has aided me in a greater understanding of this system and without his guidance completion of this work was not possible.

Dr. Shakerie taught me a great deal about PIV techniques and assisted in developing MATLAB code to analyze the experimental data.

Dr. Chakraborty was an invaluable resource as we learned the ropes of CFD together

Nate Johnson and Chuck Sites were life-savers on those days when the super computer decided to have a mind of its own and CFD simulations would not run.

ABSTRACT

MODEL VALIDATION AND TRANSITION TO TURBULENCE IN ORBITING
CULTURE DISHES

Jonathan Michael D Thomas

April 19 2016

Wall shear stress (WSS) is commonly accepted as the primary influence affecting characteristics of anchored endothelial cells when subjected to fluid flow. Orbital shakers are commonly used to study cellular responses due to their ease of use, ability to run several experiments simultaneously, and since they exert physiologically relevant oscillatory shear. These studies require comprehensive resolution of WSS, however the fluid dynamics inside orbiting culture dishes has not yet been well described since the flow is complex and difficult to quantify analytically.

A computational fluid dynamics (CFD) model of flow in an orbiting dish has been developed that yields detailed spatial and temporal resolution of WSS. The model was initially validated against primitive single point laser Doppler velocimetry data from the literature. A more comprehensive validation of the model was then performed here using both Particle Image Velocimetry (PIV) and a limited analytical solution that neglects wall effects. Average computational normalized velocity magnitudes varied by an average of just 0.3% from experimental PIV and from the analytical solution by 2.4%. WSS contours also compared very well qualitatively.

Turbulence intensities were generated from PIV for a wide range of Reynolds numbers, Froude numbers, Stokes numbers, and Slope Ratios in order to determine transition to turbulent flow. Froude number best defined the transition to turbulence with the transition occurring between 0.69 and 0.86. Velocity contours from PIV showed distinct patterns indicating laminar, transitional, and turbulent flow.

TABLE OF CONTENTS

LIST OF TABLES

LIST OF FIGURES

xiii

CHAPTER I

INTRODUCTION

The effects of hemodynamic forces on cellular responses have been studied for at least three decades, but the mechanisms linking cause and effect have not been concretely identified. Shear stresses are commonly accepted as the primary influence affecting characteristics of anchored cells subjected to fluid flow. For example, endothelial cells, lining the interior walls of arteries and veins experience shear exerted by the flow of blood and become aligned and elongated with the direction of flow and undergo other physiological and biochemical changes. The realization of the relationship between hemodynamic forces on the endothelium and the origins of atherosclerosis and vascular pathology, in general, has led to considerable attention focusing on the effects of these forces on cellular responses. Detailed, accurate information about the fluid forces acting on cells must be known in order to understand the cause and effect relationship between shear stresses and endothelial responses.

The system of study involves endothelial cell cultures grown in a Petri dish oscillating on a shaker platform. Orbital shakers are commonly used in the cell culture industry due to their ease of use, but the fluid motion inside such dishes have not been accurately modeled as the system is difficult to quantify analytically. Furthermore, it is desirable to understand how cultured cells respond to fluid forces on an orbiting platform under varying flow conditions.

1

As of yet, little effort has been made to experimentally determine fluid forces in an oscillating dish. Until now, because of the complexities in developing an accurate quantitative analysis, only oversimplified scalar functions have been used. To more accurately quantify the fluid dynamics in this system, a computational model was created here through the use of commercial computational fluid dynamics (CFD) software. The preprocessor GAMBIT was used to create the cylindrical-shaped geometry, and FLUENT solved the Navier-Stokes equations to create a complete representation of the flow field inside orbiting dishes including wall shear stresses imposed on cells in culture.

It is necessary to more thoroughly validate the computational model before further work can be completed. Until now, the best available experimental data for validation of the orbital system is wall shear stress (WSS) measured by Doppler velocimetry. This validation method is insufficient since it only measures one point at a time rather than providing complete spatial resolution at any given instant in time. Comprehensive validation from this work consists of two methods, comparing against analytical solutions and experimental particle image velocimetry (PIV). PIV provides complete spatial resolution by measuring flow over the entire bottom surface. Then, velocity magnitudes from PIV were compared with corresponding CFD simulations and analytical solutions.

Fluid forces in the dish are the combination of many properties of the system including: radius of orbit, orbital speed, dish diameter, viscosity, fluid height, density, and gravity. Identifying how each property affects fluid forces would require an extensive and cumbersome endeavor. To reduce the computational effort, the effects can be more easily determined by incorporating these seven variables into three dimensionless

parameters.. These parameters are the Slope Ratio, the Froude number, the Stokes number, and the Reynolds number.

The transition to turbulent flow has not been fully determined in orbital shaker systems, and little is understood about the effect of turbulence on WSS. Limited data on turbulence has been published, but the experiments were performed with larger dishes and higher fluid heights than are normally used in culture experiments. To determine the conditions that create turbulence, normalized turbulent intensities obtained from PIV can be analyzed against the dimensionless parameters. Velocity contours from PIV and CFD to view the free surface can then be examined to determine the physical changes that occur in turbulent flow conditions.

OBJECTIVES:

1. Employ CFD modeling to describe fluid behavior in orbiting culture dishes resulting from motion imparted by an orbital shaker apparatus.

2. Validate the model by comparing computationally derived results with experimental data obtained using PIV and with analytical equations.

3. Determine the transition to turbulence in orbital shaker systems, which dimensionless parameters affect the transition, and the effect of turbulence on WSS behavior.

CHAPTER II

LITERATURE REVIEW

2.1. SHEAR IN AN ORBITING DISH

2.1.1. Definition of Shear Stress

In Fluid Dynamics, shear stress is an important property of any gas or liquid that moves along a boundary. Shear stress is directly related to velocity. McCabe *et al*. (1993) show that when a fluid flows past a wall, the fluid sticks to the wall at their interface. This results in a velocity of zero at the interface of the wall and fluid. At distances from the wall, the velocity is not zero, however, and hence variations must occur in velocity. This results in a velocity field in the fluid where the velocity at a given point is a function of both location and time. The velocity gradient is the reciprocal of the slope of the velocity field. The local velocity gradient is also called the shear rate. Velocity gradient is defined as the change in velocity over the change in distance or:

$$\frac{du}{dy} = \lim_{\Delta y \to 0} \frac{\Delta u}{\Delta y} \tag{1}$$

A fluid resists shear so a shear force must exist wherever there is a shear rate. Shear forces act tangential to the plane in which the shear rate develops. Shear stresses are more commonly described than shear forces. Shear stress differs from normal stress in that shear stress is parallel or tangentially to a plane, where normal stress is perpendicular to the plane. Since shear stress varies with distance, a field is created that also varies with distance and time. Shear stress is defined as the force per unit area of the shearing plane or:

$$\tau = \frac{F_S}{A_s} \tag{2}$$

where

τ = shear stress

F_s = the shear force

A_s = the cross sectional area of the plane

Bird *et al*. (2002) show that equation (2) can be rearranged by substituting the velocity gradient as:

$$\tau_{xy} = -\mu \frac{du_x}{dy} \tag{3}$$

This equation is known as Newton's Law of Viscosity.

2.1.2. Experimental Methods to Determine Shear Stress

A number of experimental setups have been utilized to generate shear flow. The common approaches include parallel plate flow chambers, cone and plate apparatus, and orbital shakers. The parallel plate flow chamber generates controllable unidirectional shear easily, but the system is limited in that the width and length of the plates are substantially larger than the gap between them. Ohashi, *et al.* (2005) reviewed experimental and numerical approaches to model vascular endothelial cells exposed to shear stress from fluids. The discussion included the effects of fluid stress exerted on the endothelial cells generated by two configurations: parallel plate and cone and plate flow chambers. Levesque, *et al.* (1985) used a parallel plate flow chamber to exert laminar, steady unidirectional shear stress on bovine aortic endothelial cells to understand the effects of shear on cell morphology. By knowing the flow rate and gap between the plates, the authors developed an equation for shear stress in the parallel plate channel as follows:

$$\tau_\omega = \frac{6u^2}{\rho H^2} R_e \tag{4}$$

where

τ_ω = Shear stress

μ = Fluid viscosity

ρ = Fluid density

h = Height of the rectangular cross sectional channel of the flow chamber

R_e = Reynolds number.

This equation assumes that viscosity and density are that of water. Four key findings resulted from the experiments: endothelial cells orient with the flow direction under the influence of shear stress, a shorter time is required for cell elongation than cell alignment with flow, the degree of alignment is closely related to cell shape, and endothelial cells become more elongated when introduced to greater shear stresses. Parallel plate flow chambers were widely used thereafter as shear generating equipment for studying the effects of unidirectional shear on different biomedical responses (5-20).

Another method for determining shear stress entails generating a rotating flow field over a layer of cells attached at the base of each dish (21-23). Under this scheme, a cone or a flat plate rotates over a stationary surface where a layer of cells reside. The local relative velocity increases linearly with distance from the cone axis providing constant shear stress. Ley, *et al*. (1989) used a cone and plate apparatus to generate shear stress on endothelial cells to understand shear dependent inhibition of granulocyte adhesion to cultured endothelium by dextran sulfate. This study indicated that a uniform shear field over the entire cross-sectional area can be generated by a cone and plate flow chamber. Shear stress is easily calculated for the cone and plate apparatus since the rotation speed of the cone or flat plate and the length of

the gap between the rotating and stationary surfaces are known. The equation the authors show is:

$$\tau(a) = \frac{2\pi a f \mu}{H} \tag{5}$$

where

$\tau(a)$ = Shear stress

μ = Fluid viscosity

H = Height of fluid

f = Frequency of rotation.

The parallel plate channel flow device and cone and plate device described provide an accurate means of supplying predetermined shear stresses to a fixed layer of cells, but they are limited in that they only provide steady flows. They are further limited in that experiments must be performed successively as opposed to concurrently unless multiple devices are present.

Another apparatus was used by Owatverot, *et al.* (2005) to understand the effects of combined cyclic stretch and shear stress on endothelial cell morphology. They used a custom-built device to stretch cells, which were cultured on a silicone membrane, to generate laminar, steady, or oscillatory shear stress. The device had the ability to apply in plane, uniaxial deformation to the membrane's central region. Uniaxial deformation was maintained in the central region of the membrane due to its incompressibility. The device was developed to produce a Couette flow where shear stress is predicted by the equation:

$$\tau = \frac{\mu V}{h} \tag{6}$$

where

μ = Fluid viscosity

V = Belt velocity

h = Gap height

A novel multidirectional flow chamber was developed by Langerquist, *et al.* (2002) to investigate the endothelial cell morphology dependence on differential shear. The design of this flow chamber was centered on two flow conditions: Couette flow for the rotational component and Poiseuille flow for the axial component. The authors tested multidirectional flow with two ratios of axial and rotational shear stress magnitudes. Hsiai, *et al.* (2002) utilized bulk and surface micromachining techniques to fabricate a MEMS shear stress sensor which was operated on heat transfer principles. A value of shear stress was measured from the convective heat transferred from a heating element to the flowing fluid. They used a linear relation defined by Haritonnidis, *et al.* (1989):

$$\tau^{1/3} = \frac{V^2}{R} \tag{7}$$

where

τ = Shear stress

V = Fluid velocity

R = Radius of the cone

Chiu, *et al.* (2004) used a co-culture flow system to exert laminar, steady shear stress on vascular endothelial cells and smooth muscle cells. This system had the advantage that the chamber allowed direct observation of cells during the flow experiment via an observation window. The shear stresses observed by the authors in the chamber was calculated by the formula:

$$\tau = \frac{6\mu Q}{wh^2} \tag{8}$$

where,

τ = Shear stress

μ = Perfusate Viscosity

Q = Flow rate

w = Width of the channel

h = Height of the channel

Another method for generating shear was developed by Inoguchi, *et al*. (2007). The authors used a pulsatile circulatory apparatus that consisted of a centrifugal pump, a tube installer chamber, a compliance tank, a flow control valve, and a reservoir. They achieved steady flow at a fixed shear stress by adjusting the rotational speed on the centrifugal pump. The shear stress was determined by the equation:

$$\tau = \frac{4\eta Q}{\pi r^3}$$

(9)

Where

τ = Shear stress

η = Viscosity

Q = Flow rate

r = Tube Interior radius

Another apparatus for inducing flow on endothelial cells is the shaker flask. The shaker flask contains a suspended layer of cells with a magnetic bar that is agitated using a magnetic stirrer. Saarinen *et al*. (2000) compared production of recombinant secreted alkaline phosphatase protein in virally infected insect cells in a shaker flask to that in a rotating-wall vessel bioreactor. They showed that higher cell viability was detected in cultures grown in the rotating-wall vessel bioreactor compared to the shaker flask. The authors attributed this effect to lower shear stresses present in the rotating-wall vessel

bioreactor. Elias *et al*. (1995) conducted experiments with a spinner flask to determine the effect of turbulent shear stress. The authors found that varying orbital speed up to 7.5 rotations per second did not damage the cells. However above 2.5 rotations per second, the cells became unable to proliferate further.

An apparatus widely used for providing fluid motion to endothelial cells is the orbital shaker platform. Orbital shakers are prevalent in the cell culture industry because of their simplicity of use. A major disadvantage of the above systems of adding shear is that only one experiment can be conducted at a time causing extensive time requirements for large experimental arrays. Orbital Shakers are ideal for simultaneous cell culture experiments since several dishes can fit on a platform and are easily stackable. The most important aspect is that orbital shakers provide oscillatory flow, similar to that experienced by pulsing fluid movement in the human vasculature system.

Despite their popularity and simplicity of use, few researchers have attempted to apply the orbiting shaker as a means for correlating shear stresses to cellular responses. This is due to the complexity of accurately calculating shear stresses exerted by the fluid in this configuration. The movement of fluid in a cylinder that derives its motion from an orbiting shaker platform is oscillatory in nature. A wave develops whose peak rotates around the cylinder at an angular velocity corresponding to the orbital velocity of the cylinder. Depending on the properties of the fluid and the relative forces, the rotating wave may or may not be in phase with the orbiting motion of the cylinder. Simplified means have been used in estimating the magnitude of the shear in this system. Ley *et al*. (1989) investigated the shear dependence of endothelial cells in both orbital shaker and cone and plate experiments. The shear stresses they reported in the orbital shaker experiments were estimated analytically (24, 33) as

$$\tau_\omega = a\sqrt{\rho\mu(2\pi f)^3} \tag{10}$$

where

τ_ω = Shear stress

a = Cylinder radius

ρ = Density

μ = Viscosity

f = Frequency of rotation

Equation (10) is known as Stokes second problem solution which describes the orbital motion of a plate of infinite width having a thin layer of fluid. According to Stokes second problem, Equation (10) expresses a constant magnitude of shear. As such, it cannot predict the unsteady, oscillatory nature of shear or values of shear at various locations in the dish. Further the equation assumes no wall effects. The equation is limited to the specific condition of low Slope Ratio, low Froude number, high Stokes number and low Reynolds number.

2.1.3. Research Using Orbital Shakers for Generation of Shear

Shear Stress on the bottom of the dish in an orbital shaker apparatus is pulsatile and bidirectional, which mirrors the flow in the human vasculature system. Yun, *et al*. (2002) used an orbital shaker to generate shear stress to understand the effect of shear induced transcription factor Sp1 phosphorylation on membrane type 1-matrix metalloproteinase (MT1-MMP). The results illustrated the complex control MTI-MMP expression in endothelium in response to distinct environmental stimuli (cyclic strain versus shear stress), consisting of both the modulation of the specific transcription factor expression Egr-1 as well as transcription factor post-translational modification (serine phosphorylation of Sp1). Pearce, *et al*. (1996) used an orbital shaker to generate shear stress to study the effects of

shear on Cytosolic Phospholipase A2 (cPLA2) and MAP kinase in human endothelial cells. Kraiss, *et al*. (2000) employed an orbital shaker apparatus to study the effects of shear on a regulator of endothelial cell translation, p70/p85 S6 kinase.

Haga, *et al*. (2003) applied an orbital shaker to study the effects of shear on smooth muscle cell proliferation and Akt Phosphorylation. Dardik, *et al*. (2005) compared the effects of shear stress on endothelial cell responses between an orbital shaker apparatus and in a parallel plate chamber. They found that using the orbital shaker to generate shear stress increased cell proliferation by 29% compared to ECs in the parallel plate channel. They also observed that cells in the parallel plate chamber were aligned towards the direction of shear stress whereas cells in the center of the orbiting dish were not aligned, following the trend of cells not exposed to shear stress.

2.2. COMPUTATIONAL FLUID DYNAMICS AS A METHOD TO GENERATE WSS

2.2.1. Introduction to Computational Fluid Dynamics

Computational fluid dynamics (CFD) is a branch of fluid mechanics which uses numerical methods and algorithms in computational technology to solve and analyze fluid flow problems. Using CFD software, a virtual computational model is created to describe a system of interest. By applying the physics and chemistry of relevant fluid flow through the developed model, it is possible to predict the fluid dynamics and related phenomena of the system. CFD software uses computational modeling to accurately simulate the flow of gases and liquids, study heat and mass transfer, moving bodies, multiphase physics, chemical reactions, fluid-structure interaction, and acoustics. The physical aspects of fluid flow are governed by conservation of mass, Newton's second law, and conservation of energy. These governing equations are expressed in terms of partial differential equations solved numerically in CFD. The resulting values are advanced in space and/or time to obtain a numerical description of the flow field of interest (39). The basic methodology for solving

12

the partial differential equations used in CFD solvers are the finite difference method (FDM) and the finite element method (FEM). Both methods have been developed extensively for solving problems in fluid dynamics, heat transfer, and other applications (40).

As analytically calculating shear stress in the orbital system can be complicated, researches have used computational fluid dynamics software to better quantify the results. CFD has been used since the early 1930's with the advent of the Atanasoff automatic digital computer (Anderson *et al*., 1976). CFD began to develop further with the advent of digital computers in the early 1950s. The role of computerized flow modeling with CFD software in vasculature applications is rapidly increasing due to the advancement of high performance computers in addition to more powerful commercially available software. Advances of CFD and potential applications are directly related to the advances in computer hardware, especially processor speed and storage capacity (41). CFD software is used for simulating, analyzing, and visualizing any type of fluid flow. This provides a means to determine fluid properties that are difficult or impossible to determine in vivo.

The first major application of CFD was by Kopal, *et al.* (1947). The authors compiled tables of supersonic flow over a sharp cone by solving the governing differential equations numerically. These calculations were carried out by a primitive computer at the Massachusetts Institute of Technology. The first accurate and effective CFD solutions were not generated until the 1950s and early 1960s with the advent of high speed and more efficient computers. Researchers at that time applied CFD to solve solutions for high velocity and high temperature problems (43-46). Later CFD solutions involved the complex applications such as subsonic flow, supersonic flow, and viscous flow. These problems were not easily solved by applying a boundary layer approximation. As a result, the Navier-Stokes equations and time dependent techniques were incorporated in the mid-1960s (47). CFD

rapidly evolved into a popular and effective tool used to analyze a host of engineering problems. ANSYS gives several applications of its FLUENT CFD software (48-50):

- Aerospace and turbo machinery

- Process design and process equipment design

- Biomedical Science and Engineering

- Automotive

- Power generation and oil and gas industry

- Heat transfer and heat exchanger design

- Health care and water

- Electronics and semiconductor

- HVAC and appliances

- Materials processing including glass, plastic, and materials

- Space, defense, and marine

- Architectural design and fire research

- 16 especially important applications in chemical process industries in the design of various processes and process equipment.

The governing equations of any CFD solution in solving single or multiphase fluid flow are the Navier-Stokes equations. These partial differential equations are discretized by a FDM or a FEM. The discretization of the spatial domain into cells forms a computational grid or mesh, and an algorithm can then be applied to solve the governing equations numerically. With increasing demand of CFD solutions in varying applications, many effective CFD codes are now commercially available. Some of these popular codes generated by CFD development organizations are: ANSYS FLUENT, ANSYS FX, CD-

Adapco STAR-CD, CFDRC CFD-ACE, CHAM PHOENICS, Flow Science FLOW 3D, ADINA R&D Inc ADINA CFD, and EXA Power Flow.

2.2.2. Obtaining a CFD Solution

The fundamental method of solving a CFD solution consists of three predominant steps: preprocessing, CFD simulation, and post processing. In the preprocessing phase a geometry is created, it is checked for accuracy, flow volumes are extracted and a computation mesh is generated. In the CFD simulation phase, parameters are entered and a solution is generated. During post processing, the solution results are analyzed.

Preprocessing will now be described more in depth. Creation of a geometric domain and the associated flow region is as follows. The first step of CFD analysis is the definition and creation of geometry and a flow region. Creation of geometry for any CFD calculation allows fully developed flow over its computational domain.

Mesh generation occurs during preprocessing after the creation of a geometry. In order to solve physics the flow, it is required to subdivide the domain into smaller discrete cells called control volumes. The resulting mesh is the combination of each of these control volumes. The equations representing fluid flow through each computational cell are numerically solved to achieve discrete values of flow properties and other important transport parameters. The accuracy of a CFD solution strongly depends upon the arrangement of the mesh. Most commercial CFD solvers have a CAD interface to import a mesh from a solid modeling package. Popular modeling packages include GAMBIT, SOLIDWORKS, PARASOLID, SOLIDEDGE, PRO-ENGINEER and UNIGRAPHICS.

The mesh types available are 2D triangular/quadrilateral, 3D tetrahedral /triangular/ hexahedral/wedge/polyhedral, and mixed meshes. A mesh can be structured, unstructured, or a hybrid mesh of the two. For simple geometry, a structured mesh is preferred. This is characterized by regular connectivity and is expressed as a 2D or 3D array of a regular

distribution of rectangular cells. The major limitation of the structured mesh is the inability to generate a 2D quadrilateral mesh or a 3D hexahedral mesh. An unstructured mesh is favored for more complicated geometry. This mesh is categorized by its irregular connectivity's which are not easily expressed by simple 2D or 3D schemes. The advantage of an unstructured mesh is that it is automated meaning no code development is necessary and there is a short time requirement. It is also able to provide solutions for very large and complex problems in a short span of time. However, unstructured meshes have the drawback that the user cannot control the mesh layout. In a hybrid mesh there are characteristics of both structured and unstructured types of meshes. It takes advantage of the positive aspects of both structured and unstructured meshes but is difficult to use and requires an advanced level expertise in handling mesh properties.

The third step of preprocessing is defining a physical model. In this step, the governing equations are incorporated in the model. These include such equations as conservation of mass, conservation of energy and the equations of motion.

Appropriate boundary conditions must be integrated to model real interpretations of a fluid system of interest. Inflow and outflow boundary conditions for the system are utilized to understand the fluid behavior at the entrance and exit of the geometry. Boundary conditions are also essential for the external walls that define the flow geometry.

After the preprocessing step, a prepared mesh is exported to any commercial CFD solver through its graphical interface. After assigning the appropriate properties for the system, relevant residual values and a time step if necessary, the simulation can be initiated. Once started, the governing equations are solved iteratively until the residual values are met or a set number of iterations or time steps are completed. After completion of the flow simulation, a post processor is used to analyze and visualize the solution.

2.2.3. Basic Equations That Govern Glow in CFD

Computational models solve the complex Navier-Stokes equations that govern a system of interest. There are several basic equation that are used by a popular CFD modeler, FLUENT Flow Modeling Software, for laminar flow (51). The equations are as follows.

For conservation of mass:

$$\frac{\partial \rho}{\partial t} + \frac{\partial}{\partial x_i}(\rho u_i) = S_m \tag{11}$$

For conservation of momentum:

$$\frac{\partial}{\partial x_i}(\rho u_i) + \frac{\partial}{\partial x_j}(\rho u_i u_j) = -\frac{\partial P}{\partial xi} + \frac{\partial \tau_{ij}}{\partial x_j} + \rho g_i + F_i \tag{12}$$

Where the shear stress τ_{ij} is:

$$\tau_{ij} = \left[\mu\left(\frac{\partial u_i}{\partial x_j} + \frac{\partial u_j}{\partial x_i}\right)\right] - \frac{2}{3}\mu\frac{\partial u_i}{\partial x_i}\delta_{ij} \tag{13}$$

For conservation of energy:

$$\frac{\partial}{\partial t}(\rho h) + \frac{\partial}{\partial x_i}(\rho u_i h) = \frac{\partial P}{\partial x_i}\left(k\frac{\partial T}{\partial x_i}\right) - \frac{\partial}{\partial x_i}\sum h_j J_j + \frac{\partial P}{\partial t} + u_i\frac{\partial P}{\partial x_i} + \tau_{ij}\frac{\partial u_i}{\partial x_j} + S_h \tag{14}$$

Where h is given as:

$$h = \sum_i m_i h_i \tag{15}$$

And h_i is defined as:

$$h_i = \int_{T_{ref}}^{T} C_{pi} dT \tag{16}$$

For conservation of chemical species

17

$$\frac{\partial}{\partial t}(\rho m_i) + \frac{\partial}{\partial x_i}(\rho u_i m_i) = \frac{\partial}{\partial x_i}(J_{i,i}) + S_i \qquad (17)$$

Where

$$J_{i,i} = -\rho D_{i,i} m \frac{\partial m_i}{\partial x_i} \qquad (18)$$

After integration over the computational cells, the equations reduce to finite difference algebraic equations (52). The algebraic equations can be written in the common form:

$$\phi \sum_i (A_i - S_p) = \sum_i A_i \phi_i + S_c \qquad (19)$$

The summations occur over each of the neighboring finite difference cells. The A_i term is a coefficient which contains contributions from diffusive and convective fluxes. S_p and S_c are components in the linear source term:

$$S_\phi = S_c + S_p \phi_p \qquad (20)$$

A differentiating scheme utilizing the power law is utilized to calculate the derivatives of the flow variables and interpolate between grid points. The algebraic equations are solved using a semi-implicit iterative scheme. The scheme starts at a given set of initial conditions and converges to a correct solution after executing a given number of solutions and/or reaching a specified tolerance.

Each iteration of FLUENT software involves several steps (51). First, the u, v, and w, momentum equations are each solved using pressure to update the velocity field. Subsequently, the velocities calculated may not satisfy the continuity equation. As such, an equation resembling the Poisson is derived from the continuity equation and the momentum equations to correct for pressure. Solving this equation yields corrections for pressure and velocity fields that allow the conditions of the continuity equation to be satisfied. Then auxiliary equations such as the conservation of species are solved using the updated

18

velocities from the previous step. Next, the fluid properties are updated with the new complete set of values. Finally, the solver checks the set of equations for convergence. The steps are repeated until either the residual difference between iterations reaches a user-defined value, or a defined number of iterations is reached.

2.2.4. Methods of Discretization for Partial Differential Equations

The fundamental method behind any CFD solution is the discretization of the continuous problem domain. The velocity (v) in any continuous flow domain which can be expressed as:

$$v = v(x), 0 < x < 1 \tag{21}$$

The continuous domain is expressed in Figure 2.1.

Continuous domain
$$0 < x < 1$$

x=0   x=1
Associated with PDEs
and boundary conditions in
continuous variables
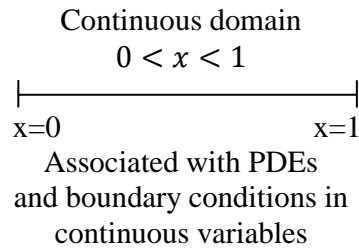
Figure 2.1. Continuous flow domain.

Considering the discrete domain where the flow variable is defined only at the grid points, the velocity will therefore be defined at an assigned number of grid points (say N) and can be expressed as

$$v_i = v (xi), \text{ where } I = 1, 2, ..., N \tag{22}$$

The discrete domain can therefore be expressed as shown in Figure 2.2.

x = x1 , x2 , ..., xN

x=0   x=1
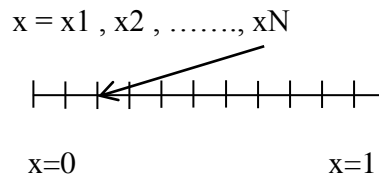
PDEs are converted in linear algebraic equation in discrete variables

Figure 2.2. Discrete domain.

19

Therefore, the finite difference method is necessary to discretize the Navier- Stokes equations into linear algebraic equations.

2.2.5. Finite Difference Method (FDM)

The fundamental approach in discretizing the governing equations in CFD is illustrated by considering a simple one dimensional equation (51):

$$\frac{du}{dx} + u^m; 0 \leq x \leq 1; u(0) = 1 \tag{23}$$

where the equation is linear with m = 1 and nonlinear with m = 2.

At m = 1, the discrete representation of the above equation will be in the grid in Figure 2.3 containing four equally spaced points with Δx = 0.33.
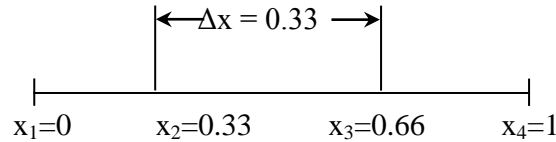
Figure 2.3. Discrete grid m=1.

At any grid point, the above governing equation will be:

$$\left(\frac{du}{dx}\right)_i + u_i = 0 \tag{24}$$

where the subscript i represents the value at any grid point x_i.

To obtain the expression of (du/dx) in terms of u at any given grid point, a Taylor's series expansion is employed with the expansion:

$$u_{i-1} = u_i - \Delta x \left(\frac{du}{dx}\right)_i + O\Delta x^2 \tag{25}$$

After rearranging,

$$\left(\frac{du}{dx}\right)_i = \frac{u_i - u_{i-1}}{\Delta x} - +O\Delta x^2 \tag{26}$$

The error, $O\Delta x^2$, in the series is a truncation error.

By eliminating the higher order terms in the above Taylor's series expansion, the following discrete equation can be achieved:

$$\frac{u_i - u_{i-1}}{\Delta x} + u_i = 0 \tag{27}$$

It is important to note that this differential equation is eventually converted into a linear algebraic equation. There are two methods widely used by most commercial CFD codes in performing a finite difference method depending on the types of flow past complex geometries: Finite Volume Method and Finite Element Method.

Finite Volume Method:

A Finite Volume Method (FVM) is used by the commercial CFD code, FLUENT. In this method, the quadrilateral grid is called a "cell" and the grid point is referred to as the "node". The cells are usually triangular in 2D, and tetrahedral, hexahedral, or prisms in 3D. In this method, the integral form of the conservation equations are applied to a control volume to get the discrete equations for each cell.

In practice, the integral form of the continuity equation for steady incompressible flow can be written as (51):

$$\int_S \vec{V}.\hat{n}dS = 0 \tag{28}$$

where, S is the surface of the control volume over which the integration occurs. The above equation implies that the net volume flow into the control volume is zero.
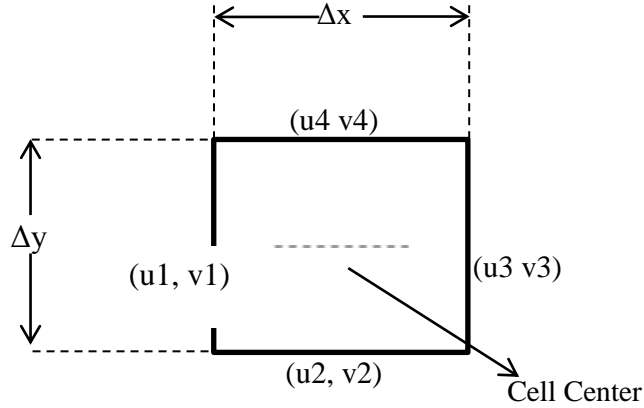
Figure 2.4. Illustration of finite volume method.

The velocity at any face *i* of above rectangle can be expressed as:

$$\vec{V_i} = u_i\hat{\imath} + v_i\hat{\jmath} \tag{29}$$

Applying the mass conservation from equation (28), the discrete form of the continuity equation can be achieved in the following form:

$$-u_1\Delta y - v_1\Delta x + u_3\Delta y + u_4\Delta x = C \tag{30}$$

Equation (30) indicates that the net mass flow throughout the control volume is zero, ensuring that mass is conserved in the cell. Other governing equations such as conservation of momentum and energy also can be discretized into simple linear algebraic equations by applying the finite volume method.

Finite Element Method:

The Finite Element Method (FEM) is another technique to discretize the governing partial differential equations of a system of interest into simple algebraic linear equations. It was originally developed to study stresses in complex airframe structures, but currently it is widely applied to the broad field of continuum mechanics and different fluid flow due to its specific advantages over the traditional finite difference (FVM) method. FEM is used to provide a pointwise approximation to the governing equations and it can be further extended in an array of grid points. Though it is a popular technique in treating difficult problems, it

cannot be used to model irregular geometries having unusual boundary conditions. FEM can overcome limitations of the finite difference method. Unlike the finite difference method which creates the solutions over an array of grid points, in FEM the solution regions are built up on many small, interconnected subregions or elements. The most common commercial finite element software providers are: ANSYS, ADINA FEA, ABAQUS, SDRD-ideas, RASNA, MSC/NASTRAN.

2.2.6. CFD Techniques for Analyzing Multiphase Flow

Modeling of different processes often requires analyzing multiphase flow. These flow include liquid-liquid, gas-liquid, and liquid-solid interactions. Proper multiphase flow modeling is essential for those cases to understand the fluid behavior on interfaces that are present. There are two available approaches to model multiphase flows numerically: the Euler-Lagrange approach and the Euler-Euler approach (51).

The Euler-Lagrange approach

The Euler-Lagrange approach is used to model the Lagrangian discrete phase. Using this model, the trajectory and state of individual particles can be tracked in space and time by integrating the equations of mass, motion, and energy for each particle of the system (52). It is to model systems which involve particles. Fluid flow is considered as having a continuous phase by solving the Navier-Stokes equations averaged over time. The dispersed phase is solved by tracking different types of particles, bubbles, or droplets. It exchanges the momentum, mass, and energy with the continuous fluid phase (49). The Euler-Lagrange method is applied to model an extensive variety of equipment and fluid flow involving the discrete phase. Applications of this model include modeling of spray dryers, coal, and fuel combustion.

The Euler-Euler approach

Modeling of multiple continuous phases utilizes the Euler-Euler approach (53). The different continuous phases are considered as mathematically interpenetrating fields. A volume fraction that is a continuous function of space and time is used by this model. This is since the volume of a phase cannot be carried into the other phase. The conservation equations of each phase are used to obtain a set of similar equations for all phases. Three Euler-Euler multiphase models are available depending on the modeling requirements.

The Volume of Fluid (VOF) model is a surface tracking technique that is applied to a fixed Eulerian mesh. In this model, a single set of momentum equations is shared by two immiscible fluids. The volume fraction for each fluid in each cell is tracked throughout the domain. This results in the same set of governing equations in a single phase flow being solved for the mixed flow. The VOF model is applied in modeling stratified flow, free surface flow, sloshing, fluid motion after breaking of a dam, prediction of a jet break up, etc. The basic equations related to a VOF model are described below:

$$\rho = \sum_i \rho_i \, \alpha_i \tag{31}$$

$$\mu = \sum_i \mu_i \, \alpha_i \tag{32}$$

$$c_p = \sum_i \frac{(c_p)_i \rho_i}{\rho} \alpha_i \tag{33}$$

Where

α_i = volume fraction

ρ_i = density

μ_i = molecular viscosity

$(c_p)_i$ = specific heat of the ith phase.

The transport of volume fraction is described by the following conservation equation:

$$\frac{d}{dt}\int_V \alpha_i dV + \int_S \alpha_i(v - v_g)\, da = \int_V s_{\alpha_i}\, dV \qquad (34)$$

Where s_{α_i} is the source or sink of the ith phase.

The Mixture model is designed for two or more phases and solves the mixture momentum equation to predict a dispersed phase. It is applied to model bubbly flows, sedimentation, and cyclone separators etc.

The Eulerian model solves a set of momentum and continuity equations for each phase. It is generally applied to model the granular flows, where the properties are obtained from kinetic theory. Flows through bubble columns, fluidized beds, and particle suspensions are modeled by this method.

2.2.7. Application of CFD in Quantifying Wall Shear Stress

A host of intricacies arise when quantifying WSS while studying its effects on the human vasculature and the associated cellular responses. Fluid flow is complex due to the complicated arrangements of different parts of the human vasculature and varying physiological conditions. In the vasculature steady and unidirectional, oscillatory and unidirectional, pulsatile and unidirectional, and oscillatory and bi-directional flow types are observed. Flow can be steady and unidirectional or unsteady and pulsatile depending on the location. The character of WSS exerted by flow is different in different parts of the human vasculature due to this.

To fully understand the effects of WSS on cellular responses, WSS must be quantified both experimentally and analytically, a difficult endeavor. No previous studies have reported measured pulsatile bi-directional WSS either experimentally or analytically. To reverse this deficiency, CFD is utilized to model the fluid flow and quantify WSS. With CFD software, a model can be generated that provides complete spatial and temporal

resolution of flow conditions inside the dish. The CFD model has the further benefit of allowing the system to be examined as unsteady state; WSS values can be observed during oscillation. CFD also allow various parts of the human vasculature to be modeled and the fluid flow simulated by mimicking the same vascular physiological conditions. As a result, an accurate quantification of different types of WSS can be achieved by simulated fluid flow.

Early attempts using CFD software to solve the Navier-Stokes equations dealt with steady flow problems as applied to flow over a surface of cells. Sakurai *et al.* (1991) used CFD to study flow over cultured endothelial cells. A preliminary result of the three dimensional computation of the flow field around cultured EC has been reported there. Using a wavy surface representing endothelial cells, Satcher *et al.* (1992) assumed local, linear shear flow in modeling the arterial endothelium to understand the effects of shear stress on endothelial cells. In another study, Yamaguchi, *et al.* (1987) applied CFD for the shear stress measurement over cultured endothelial cells. They found that the shear stress values varied greatly with the cell configuration.

Other CFD studies incorporate pulsatile flow into simulations and, in a number of cases, compare the CDF predictions with experimental data obtained from physical models. Weston, *et al.* (1998) compared steady and pulsatile flow in a pipe with CFD simulations of flow through the pipe. Velocity in the pipe was measured by MRI technique whereas wall shear stresses were determined by CFD. The morphology of cultured endothelial cells under shear loading was investigated by Yamaguchi, *et al.* (2000). Banerjee, *et al.* (2000) evaluated the hemodynamic implications of coronary artery balloon angioplasty with CFD. Berthier, *et al.* (2002) compared blood flow patterns calculated in a CFD modeled coronary vessel by three different methods. The results showed that pressures, shear stress, and velocity profiles obtained by computational simulation were harshly affected by geographical modification. Papathanasopoulou, *et al.* (2003) found good agreement between MRI

technique and CFD simulations when comparing velocity measurements in a physiologically realistic model of human carotid bifurcation with pulsatile flow. A mechanism for morphological remodeling of endothelial cells induced by blood flow was studied by Fukushima, *et al.* (2003). The authors used CFD to measure the shear stress distributions using a simulated flow field. They examined how shear on the surface of a group of cells changed. The results showed on some cells shear stress was increased and morphological changes of each cell was not always adaptive.

More recent CFD studies have further expanded the depth of research in flow over cell systems. Using CFD, Marshall, *et al.* (2004) studied the generation generate pulsatile flows. In this study, the experimental flow pattern and derived WSS were compared with the CFD prediction. Buschmann, *et al.* (2005) performed an analytical and numerical analysis of the steady, laminar, flow in a 3D system of a Newtonian fluid at low Reynold's number to investigate the response of endothelial cells to fluid shear stress in the oscillatory region of the distal vessel. Van Tricht, *et al.* (2006) compared the hemodynamics in hemodialysis grafts by CFD methods. A 3D model was developed to simulate the flow to understand how differential arterial anastomotic geometries result in different hemodynamics at the arterial (AA) and venous anastomosis (VA) in the two graft types – 6 mm graft (CD) and 4-7 mm graft (TG). By analyzing the hemodynamic parameters that includes shear stress, shear stress gradient, and pressure gradient, the simulation showed that TG did not show a better outcome compared to the CD. Morbiducci, *et al.* (2007) applied CFD while investigating the existence of a relationship between helical flow structures and vascular wall indexes of atherogenesis in aortocoronary bypass models with different geometric features. The results established that helical flow constitutes an important flow signature in vessels and its strength as a fluid dynamic index for risk stratification in the activation of both mechanical and biological pathways leads to fibrointimal hyperplasia. Smith, *et al.* (2006) used 2D CFD to

27

calculate the shear stress in left coronary artery bifurcation for pulsatile flow. Results showed that the magnitude of shear stress has a large influence on the development of coronary arterial disease; selection of a blood viscosity model is a key factor in adequately simulating the flow via CFD. Brown, *et al.* (2007) studied the flow conditions in a parallel plate bioreactor by using CFD. The authors characterized the system experimentally using a computer controlled flow regulation device and associated flow visualization techniques. Jung, *et al.* (2008) used three phase analytical to model blood flow. A three phase CFD approach is used to numerically simulate the local hemodynamics this regime. Tokuda, *et al.* (2008) studied 3D numerical simulation of blood flow in the aortic arch to understand mechanism of stroke during cardiopulmonary bypass. A finite element method was applied to simulate the blood flow numerically. The results showed that blood flow during a cardiopulmonary bypass can be modeled and simulated by applying CFD and a finite element method. Dong, *et al.* (2008) used CFD in the design and manufacture of a bioreactor. CFD simulations of different circular bioreactors with various parameters were executed in this effort and concentrations of glucose and lactate in different time and shear stresses were obtained here. Dehlagi, *et al.* (2008) analyzed the shear stress in stented coronary artery using a 3D CFD model. The results showed that the analyses of shear stress between stent struts, pre, and post stent regions are essential in stent design. Nanduri, *et al.* (2009) utilized CFD techniques to simulate biological flow. A simple MATLAB based grid generation technique suitable for CFD of external and internal biological flows (blood flows, respiration, and flows around the human body) was therefore proposed in this study.

More recently, CFD has been used to gain a better understanding of the orbital shaker system. Berson *et al.* (2008) developed the first computational model of the orbital shaker system. The model allowed investigation of WSS over the entire surface of a dish. With the ability to provide complete spatial resolution of WSS, CFD has been used to examine the

28

effects of hemodynamic forces on cellular responses in different flow patterns and shear ranges. Zhang *et al*. (2009) used CFD to examine how the free surface changes as the dish RPM and the resting fluid height was varied and the associated oxygen saturation constant at each of these flow conditions. Sargent *el al*. (2010) used CFD to understand the hydrodynamic properties on areas of embryoid body growth. Warboys *et al*. (2010) used CFD to determine WSS in a culture dish to aid in finding the effects of prolonged shear. Thomas *et al*. (2011) compared the CFD model developed by Berson *et al*. (2008) to experimental laser Doppler velocimetry data and an analytical solution with good agreement. Potter *et al*. (2011) used CFD to aid in the study of the effect of chronic heterogeneous shear stress on endothelial cell morphology and gene expression. Chakraborty *et al*. (2012) used CFD to study WSS and develop a direction of oscillating shear (DOSI) index to aid in quantifying the direction of shear. The DOSI index was used to examine how shear affected cell proliferation and morphology.

2.3. PARTIVLE IMAGE VELOCEMITRY TO VALIDATE THE CFD MODEL

2.3.1. PIV Background

In 1904, Ludwig Prandtl was the first person to use particles to study fluids in a methodical way (Rotta, 1990). He designed and utilized flow visualization techniques in a water tunnel to study aspects of unsteady separated flows behind wings and other objects. Flow in the tunnel was visualized by suspending mica particles on the surface of the water giving Prandtl insight into many basic features of unsteady flow phenomena. However, Prandt was only able to get qualative assessments of flow with the technology available at the time.

The first modern predecessor to PIV was Laser Doppler Velocemitry, developed in the 1960's At the Research Laboratories of Brown Engineering Company, with the advent of the helium-neon laser (Foreman *et al*., 1965). Soon after its development, it was shown that

fluid flow measurement could be made from the Doppler Effect on a He-Ne beam scattered by very small polystyrene spheres entrained in the fluid. The roots of modern PIV lie with Speckle Interferometry developed by several groups in the late 1970's (Grant, 1994).

It wasn't until the 1980's that PIV began to develop (Raffel, 1998). Researchers found it beneficial to decrease the particle concentration to levels where individual particles could be viewed. This lead to the further finding that flows were easier to characterize if they were split into small interrogation areas that could be examined individually, generating one velocity per interrogation area. Images at this time were recorded using analog cameras that were slow and took immense amounts of computing time and power to be analyzed.

As technology in optics, lasers, electronics, video and computers developed flow measurement evolved from a quantitative flow visualization system into a technique that can be utilized for quantitative measurement of complex instantaneous velocity fields. Thanks to digital cameras with a CCD chip and increasingly powerful computers, PIV has become the primary technique for analyzing flow fields.

2.3.2. Introduction to Particle Image Velocimetry

2.3.2.1. Overview

A PIV system (TSI, Inc., www.tsi.com) determines velocity by tracking fluorescent particles within a flow regime. Dual lasers equipped with spherical and cylindrical lenses to give a light sheet to excite the fluorescent particles. Laser light illuminates a plane in the flow, in which the position of each particle is recorded using a digital camera. A fraction of a second later, another laser pulse illuminates the same plane, creating a second particle image. The difference between the two images, a function of particle displacement, gives velocity across the examined surface. Scheimpflug hardware, rotating mounts for each camera, and an optical rail system support the cameras. The Scheimpflug mounts rotate about the CCD plane to achieve best focus, as well as to maintain constant field of view.

2.3.2.2. Seeded Tracer Particles

PIV is based on the direct determination of the two fundamental dimensions of velocity: length and time (Raffel *et al*., 1998). However, it measures velocity indirectly as it measure particle velocity as opposed to fluid velocity directly. Therefore it is important to check the properties of the particles to avoid major discrepancies between fluid and particle motion. A primary source of error occurs when the fluid density and particle density do not match, due to the influence of gravitational forces. If the particles are approximated as spherical and of very low Reynolds number, then the ability of the particles to follow the fluid's flow is directly proportional to the difference in density between the particles and the fluid and directly proportional to the square of the particles' diameters. If there is a sufficient difference in properties, the PIV results will not be considered precise as the particles will not follow the flow well enough.

Another important characteristic of particles is their light scattering behavior. Since the obtained particle image intensity, and therefore the contrast of the PIV recordings, is directly proportional to the scattered light power, it is generally more effective to increase the image intensity by properly choosing the particle size than by increasing the laser power (which could result in purchasing a new, expensive laser). For spherical particles with diameters larger than the wavelength of the laser light, the scattered light from the particles is dominated by Mie scattering and so is also proportional to the square of the particles' diameters (van de Hulst, 1957).

Based on the physical properties and light scattering ability of seeding materials, there is a range of usable diameters for each material. Table 3.1 shows mean particle diameters for liquid flows. As for optimal particle sizing, the particles should be sufficiently large to scatter a sufficient amount of light, but also small enough so that the particles' response time to the fluid motion is quick enough that it follows the flow pattern accurately.

31

Table 2.1. <u>Mean diameter of tracer particle materials</u>.

Type	Material	Mean diameter in μm
Solid	Polystyrene	10 – 100
	Aluminum	2 – 7
	Glass spheres	10 – 100
	Granules for synthetic coatings	10 – 500
Liquid	Different oils	50 – 500
Gaseous	Oxygen bubbles	50 – 1000

2.3.2.3. Light Sources

Lasers are used widely in PIV applications because of their ability to emit a single wavelength of light with high energy and in short pulses. Quick pulses allow for short exposure times. Generally, a laser is devised of three components: the laser material, the pump source and a mirror arrangement. The laser material consists of a semiconductor solid material or gas inside of a bulb. The pump source presents chemical or electromagnetic energy that excites the laser material. Oscillation of the laser material is allowed by the mirror arrangement.

There are several types of lasers that are commonly used: Helium-Neon, Copper-vapor, Argon-Ion, semiconductor, Ruby and Nd:YAG. Helium-Neon lasers are the most efficient lasers in the visible range are also the most commonly used lasers. They have a wavelength of 633nm and their power generally ranges from 1 mW to 10 mW. Typically for PIV applications, they are used for evaluation of images rather than for illuminating flow. Copper-vapor lasers are characterized by a high average power level of typically 1-30 W and a wavelength of 510 or 578 nm within the yellow and green range. They cannot achieve continuous operation, but can perform pulse operation with repetition rates in the kHz range. Argon-Ion lasers are quite complicated, but they can supply high power with over 100W at 514 nm and 60 W at 488 nm. They are frequently used for Laser Doppler velocemity and are often used for low speed PIV due to their availability. Semiconductor lasers have the

advantage of being a compact system. Since heating is greatly reduced due to higher efficiencies, semiconductor lasers can produce a beam as high as 100 mW for continuous operation. Ruby lasers were the first working laser type developed. They operate at a wavelength of 694 nm. While they are highly inefficient, they are usable for pulse mode operations.

Nd:YAG lasers are the most important solid state laser for PIV applications. In these lasers, the Nd^{3+} ion is incorporated into yttrium-aluminum-garnet (YAG) crystals. These lasers have a high amplification and good mechanical and thermal properties and operate at a 532 nm wavelength. In PIV applications, with the inclusion of a quality switch (Q switch) the laser can be operated in a triggered mode from an external source. The Q switch allows for large single pulses to be generated from the laser. ND:Yag lasers usually operate in a repetitive mode; suitable and consistent beam properties are only possible with a nominal repetition rate and flashlamp voltage. The beam quality is very poor compared to other laser types when only single pulses are used. Most ND:YAG systems lasers used in PIV systems use a double-oscillator set up to allow the ability to adjust the separation time between the two illuminations of the tracer particles independently of the pulse strength.

2.3.2.4. Light Sheet Optics

Using optics, laser light can easily be bundled into a thin light sheet that can illuminate the tracer particles in a desired plane. Optics are thoroughly defined by (Hecht *et al.*, 1974) For Nd:YAG lasers, several lenses are required in order to generate a thin light sheet. Optics for the laser consists of a spherical and cylindrical lens grouping. The spherical lens concentrates the laser into a thin beam and the cylindrical lens converts the thin beam into a sheet of light. This is critical as the PIV technique cannot generally measure motion normal to the laser sheet and so this is eliminated by maintaining an entirely 2-dimensional laser sheet. However, the spherical lens cannot compress the laser sheet into an actual 2-

dimensional plane. The minimum thickness is on the order of the wavelength of the laser light and occurs at the focal point of the spherical lens which is a finite distance from the optics setup.

2.3.2.5. Digital Image Recording

In order to characterize fluid flow by PIV, the camera must take two exposures as the laser fires to create an image pair. A high speed digital camera using CCD or CMOS chips can capture two images with a time on the order of nanoseconds between frames. High speed CCD or CMOS cameras are expensive, but normal digital cameras cannot achieve the speeds necessary to take high speed image pairs. The speed of subsequent images is limited since the previous image pair must be transferred to the computer before the next pair can be captured.

CCD's (coupled-charge device) are much more widespread in PIV applications than CMOS's. A CCD sensor is composed of a square or rectangular array of many individual CCD's. An individual CCD element is called a pixel and is usually 10 x 10 μm^2. A CCD at its core is an electronic sensor that converts light photons into electrons. A CCD has a complex cross section; it is built on a semiconducting substrate, with metal conductors on the surface, an insulating oxide layer, an anode n-later and a cathode p-layer.

A CCD functions as follows. A small voltage applied between the conductor and p-layer creates an electric field in the semiconductor. This creates a lack of electrons in the pixel known as a potential well, which will store image information for that pixel. When a photon enters the p-n junction on the semiconductor, an electron-hole pair is generated by the photoelectric effect. As the hole is absorbed by the p-layer, the generated electron migrates to the potential Well where it is stored. Electrons accumulate in the well for the duration of the pixels exposure to light. Typical CCD's have a capacity of 10,000 to 100,000 electrons

per pixels and the number of electrons stored compared to the capacity determine the brightness of that pixel in the image.

2.3.2.6. Synchronizer

The camera and laser are connected to the computer software that controls the PIV system through a synchronizer. It controls the timing between image exposures and also permits image pairs to be acquired at various times along the flow. The synchronizer is the external trigger for both the laser and the camera. Set from computer software, the synchronizer controls the timing of each image of the CCD camera's image pair while also with the firing of the laser at 1 ns precision. It is ideal to have a displacement of 8 pixels between image pairs for accurate PIV analysis. Controlling the time of both the laser and camera at such small increments makes for the accurate measurements needed for number of flow conditions.

2.3.3. Basic Equations Governing PIV

2.3.3.1. Overview

A detailed mathematical description of statistical PIV evaluation was first proposed by Adrian (1988). This work focused on auto-correlation methods and the group expanded their work to cross-correlation analysis in 1992 (Keane and Adrian, 1992). Statistical PIV was no longer a desirable method as digital PIV techniques became available. In 1993, Westerweel (1993) developed a thorough mathematical evaluation of digital PIV. Raffel *et al*. (1998) developed a simplified mathematical model of the recording and the subsequent statistical evaluation of PIV. They described the two-dimensional spatial estimator for cross-correlation of double exposed PIV used normally in modern PIV systems. Necessary equations for PIV are developed in the section below.

2.3.3.2. Particle Image Location

PIV recordings are subdivided into interrogation windows of a predetermine pixel size during evaluation. Due to the inherent thickness of the laser sheet, the interrogation window can also be referred to as an interrogation volume. The two interrogation volumes of the image pair together define the measurement volume. A single image pair will consist of a random distribution of particles among its many interrogation volumes which corresponds to the pattern of N particles inside the flow:

$$\Gamma = \begin{pmatrix} X_1 \\ \vdots \\ X_n \end{pmatrix} \text{ with } X_i = \begin{pmatrix} X_i \\ Y_i \\ Z_i \end{pmatrix} \tag{35}$$

This equation is the position of a tracer particle in a 3N-dimensional space. Γ describes the state of the ensemble at a given time. X_i is the positional vector of the particle i at time t. Lower case letters refer to the image plane such that

$$x = \begin{pmatrix} x \\ y \end{pmatrix} \tag{36}$$

is the image position vector in this plane. The assumption must be made that particle position and image position are related by a constant magnification factor M from the camera lens giving:

$$X_i = x_i/M \text{ and } Y_i = y_i/M \tag{37}$$

2.3.3.3. Image Intensity Field

It is important to develop a mathematical representation of the intensity distribution in the image plane. The image is best described by a convolution of the geometric image and the impulse response of the imaging system, which is known as the point spread function. The assumption is made that the point spread function of the imaging lens $\tau(x)$ is Gaussian versus x and y. The convolution product of $\tau(x)$ with the geometric image of the particle at the position x_i describes the image of a single particle at position X_i. The Dirac delta-

function shifted to the position xi describes the geometric part of the particle image. Therefore, the image intensity field of the first image is expressed by:

$$I = I(x, \Gamma) = \tau(x) * \sum_{i=1}^{N} V_0(X_i)\delta(x - x_i) \tag{38}$$

where $V_0(X_i)$ is the transfer function giving the light energy of the image of an individual particle i inside the interrogation volume V_I and its conversion into an electric signal and $\tau(x)$ is identical for every particle position.

The following assumptions become important: Z is the viewing direction, light intensity in the interrogation window in only a function of Z, light intensity in the interrogation window is only a function of Z, and the image intensity depends on X and Y due to the weight function. Hence, $V_0(X)$ describes the shape, extension, and location of the actual interrogation volume:

$$V_0(X) = W_0(X, Y)I_0(Z) \tag{39}$$

where $I_0(Z)$ is the intensity profile of the laser sheet in the Z direction and $W_0(X, Y)$ is the interrogation window function geometrically back projected into the light sheet. $I_0(Z)$ is described as:

$$I_0(Z) = I_Z \, exp\left(-8\frac{(Z-Z_0)^2}{\Delta Z_0^2}\right) \tag{40}$$

This equation may be used to describe the Gaussian intensity profile of the laser light sheet where ΔZ_0 is the thickness of the light sheet and I_Z is the maximum intensity of the light sheet. $W_0(X, Y)$ can be described by a Gaussian window function with maximum weighting W_{XY} at the location X_0, Y_0 by:

$$W_0(X, Y) = W_{XY} \, exp\left(-8\frac{(X-X_0)^2}{\Delta X_0^2} - 8\frac{(Y-Y_0)^2}{\Delta Y_0^2}\right) \tag{41}$$

If there is no particle overlap between interrogation windows in the selected image pair then the assumption is made that $\tau(x) * \delta(x - x_i) = \tau(x - x_i)$ and equation X for image intensity field simplifies to:

$$I(x, \Gamma) = \sum_{i=1}^{N} V_0(X_i)\, \tau(x - x_i) \tag{42}$$

2.3.3.4. Cross-Correlation of an Image Pair

PIV data is evaluated by locally cross-correlating both frames of an image pair. For cross-correlation, the constant displacement D of all particles in the interrogation window is assumed so that the particle locations during the second image at time $t' = t + \Delta t$ are (Papoulis, 1991):

$$X_i' = X_i + D = \begin{pmatrix} X_i + D_X \\ Y_i + D_Y \\ Z_i + D_Z \end{pmatrix} \tag{43}$$

And particle displacements in the image pair are given by:

$$d = \begin{pmatrix} MD_X \\ MD_Y \end{pmatrix} \tag{44}$$

The image intensity field for the second image is described by the following:

$$I'(x, \Gamma) = \sum_{j=1}^{N} V_0'(X_j + D)\, \tau(x - x_j - d) \tag{45}$$

where $V_0'(X)$ is the interrogation volume of the second image. Since the light sheet and interrogation are assumed to be the same for both images, the cross-correlation function of two interrogation windows is:

$$R_{II}(s, \Gamma, D) = \frac{1}{a_I} \sum_{i,j} V_0(X_i) V_0(X_j + D) \int_{a_I} \tau(x - x_i)\tau(x - x_j + s - d)\, dx \tag{46}$$

where s is the separation vector in the correlation plane. By distinguishing the terms $i \neq j$ which represent the correlation of different images and hence the noise in the plane and the $i = j$ terms which are the correlation of each image with itself the equation can be separated to:

$$R_{II}(\mathbf{s}, \mathbf{\Gamma}, \mathbf{D}) =$$

$$\frac{1}{a_I}\sum_{i \neq j} V_0(X_i)V_0(X_j + D) \int_{a_I} \tau(x - x_i)\tau(x - x_j + s - d)dx + \frac{1}{a_I}\sum_{i=j} V_0(X_i)V_0(X_i +$$

$$D) \int_{a_I} \tau(x - x_i)\tau(x - x_i + s - d)dx \tag{47}$$

Each interrogation window can be decomposed into three parts:

$$R_{II}(\mathbf{s}, \mathbf{\Gamma}, \mathbf{D}) = R_C(\mathbf{s}, \mathbf{\Gamma}, \mathbf{D}) + R_F(\mathbf{s}, \mathbf{\Gamma}, \mathbf{D}) + R_D(\mathbf{s}, \mathbf{\Gamma}, \mathbf{D}) \tag{48}$$

where $R_C(\mathbf{s}, \mathbf{\Gamma}, \mathbf{D})$ is the convolution of mean intensities of I and $R_F(\mathbf{s}, \mathbf{\Gamma}, \mathbf{D})$ is the noise component resulting from all $i \neq j$ terms. $R_D(\mathbf{s}, \mathbf{\Gamma}, \mathbf{D})$ is the cross-correlation peak at (0,0) that corresponds to the correlation of each particle image with itself (i.e $i = j$). For a Gaussian particle image intensity distribution:

$$\tau(x) = K \ exp\left(-\frac{8|x|^2}{d_\tau^2}\right) \tag{49}$$

The auto-correlation $R_T(\mathbf{s})$ is developed by plugging $\tau(x)$ into $R_D(\mathbf{s}, \mathbf{\Gamma}, \mathbf{D})$ assuming a Gaussian width of $\sqrt{2}d_\tau$ and setting it equal to the exponential and integral terms such that:

$$R_T(\mathbf{s}) = \ exp\left(-\frac{8|s|^2}{(\sqrt{2}d_\tau)^2}\right)\frac{1}{a_I}\int_{a_I} \tau^2\left(x - x_i + \frac{s}{2}\right)dx \tag{50}$$

Simplifying yields a cross-correlation function for $i = j$ of:

$$R_D(\mathbf{s}, \mathbf{\Gamma}, \mathbf{D}) = R_T(\mathbf{s} - \mathbf{d})\sum_{i=1}^{N} V_0(X_i)V_0(X_i + D) \tag{51}$$

Therefore, for a given distribution of particles inside the flow, the displacement correlation peak reaches a maximum for $\mathbf{s} = \mathbf{d}$. Hence, the location of this maximum gives the average displacement in the laser sheet plane and consequently the U and V components of the velocity inside the flow.

2.3.4. Experimental Measurements in Orbiting Petri Dishes

An early experimental evaluation of the orbiting dish was performed by Dardik *et al.* (2005). They collected experimental WSS values using a one-dimensional optical Doppler velocimetry probe, in this case aligned to measure the tangential component. Dardik *et al.*

(2005) reported scatter plots of Doppler shifts from the ultrasonic velocity probe for a single case for many orbits. The Doppler velocimetry system used by Dardik *et al*. (2005) provided measurements at only a single point in the dish. For more thorough experimental examination, measurements with greater spatial resolution were needed.

Particle Image Velocimetry (PIV) represents a whole-field technique capable of detecting spatial flow structure. Kim and Kizito (2009) used PIV to study flow in the XY and XZ plane. They observed several vortex patterns in the XZ plane over differing flow regimes. Salek *et al*. (2011) observed a horizontal plane 2 mm from the bottom of a 17.5mm radius six-well culture plate. They performed a comparison with CFD with good agreement, but due to system limitations they were not able to get results within 5 mm of the side walls. Weheliye *et al*. (2013) also studied fluid dynamics in an orbital shaker with PIV. They examined both horizontal XY and vertical XZ slices or vorticity inside the dish to determine the physical effects of varying dish parameters. An in phase and out of phase flow condition was observed and examined for several rpms resting fluid eights. Free surface height ratios were plotted versus Froude number to develop a scaling law for the orbital shaker system. Rodriguez *et al*. (2013) used PIV to calculate normalized kinetic energies in the XY and XZ plane. They examined kinetic energy contours in both planes and plotted them versus Froude number. Mixing time was also examined versus Froude number in effort to make a correlation between mixing time and kinetic energy. They determined that insertion should be made closer to the wall near high wall shear stress regions to facilitate mixing. Reclari *et al*. (2014) used PIV to examine the development of the free surface wave forms and observed several patterns including single and multiple crested waves and breaking waves.

Klöckner *et al*. (2012) used temperature sensors and torque measurements to calculate volumetric power input for the orbital shaker system. They developed correlations for 10L and 50L containers and validated them with containers at 200L and 2000L, much

larger than typical laboratory scale. They plotted power data versus a broad number of dimensionless parameters to get a better understanding of the system. This led to the development of new empirical correlations for power input in the system.

Thomas *et al.* (2016) used PIV to validate a CFD model orbital of an orbiting petri dish. They found velocity vector components for one complete orbit differed between CFD and PIV by less than 5%. Computational velocity magnitudes averaged over the interior 20% radius, the region where the analytical solution is most applicable, were 0.3% higher than the analytical values while the experimental values in the same region were 2.4% higher. Thomas *el al.* (2016) described four dimensionless parameters that simplify describing the flow regime of the orbital shaker. These are the Slope Ratio:

$$Sl = \frac{Ra\omega^2}{gH} \tag{52}$$

Froude number:

$$Fr = \frac{R\omega}{\sqrt{gH}} \tag{53}$$

Stokes number:

$$St = H\sqrt{\frac{\omega\rho}{\mu}} \tag{54}$$

and Reynolds number:

$$Re = \frac{HR\omega\rho}{\mu} \tag{55}$$

They showed that three of the parameters have observable physical effects when the value becomes high. At a high Slope Ratios, the free surface of the wave changes from linear to concave as the shallow portion approaches the bottom of the dish. At high Froude numbers, the leading edge of the wave changes from smooth to a crashing hook wave. At high Stokes

numbers, the wave becomes out of phase. This work will utilize these four dimensionless parameters to aid in defining turbulence in the orbital shaker system.

2.3.5. Turbulence Transition in Oscillatory Flow

The defining early work on turbulence in oscillatory flow was performed by Hino *et al*. (1976). They used a piston to generate oscillatory flow in a series of straight pipes with bell ends for smooth transitions to create of matrix of amplitude of the cross-sectional mean velocity over a range of dimensionless parameters. Hino *et al*. (1976) compared velocity amplitude to three parameters: the Reynolds number, the Stokes number, and Stokes Reynolds number. The Stokes Reynolds number is the Reynolds number based on Stokes layer thickness and was defined as the Reynolds number divided by two times the Stokes number. Both Reynolds number and Stokes number were shown to have an effect on the turbulence transition in oscillatory flow.

A number of subsequent works have investigated turbulence in oscillatory flow at the transition region expanding on the work by Hino *et al*. (1976). Arkhavan *et al*. (1991) measured velocity in a pipe with a laser-Doppler anemometer over a series of Reynolds and Stokes numbers to examine the transition. Eckmann and Grotberg (1991) used laser-Doppler velocimetry to analyze velocity in oscillatory flows in a circular tubes. They found the transition to turbulence to be based on Stokes Reynolds number and that turbulence was greatest in areas with greater Stokes-layer thickness. Zhao and Cheng (1996) looked at velocities in a copper tube under oscillating flow. They looked at turbulence in terms of Reynolds number and an oscillation of the fluid parameter.

Vittori and Verzicco (1998) simulated 3-D oscillatory flow by means of the Navier-Stokes equations. Differing from earlier studies, they calculated turbulent kinetic energy to detect turbulence. Turbulent energies were compared with Stokes Reynolds number to determine transition. Sherwin and Blackburn (2005) examined transition to turbulence in

42

four flow types in a stenotic tube, including oscillatory flow. They calculated turbulent kinetic energies for a numerical solution of the flows and compared them with Reynolds numbers to determine the turbulence transition. Trip *et al*. (2015) used PIV to examine the turbulence transition in oscillatory flow in a straight pipe. They compared turbulence intensity to Reynolds number. Turbulence intensity is a parameter widely used to describe turbulence. It is defined by:

$$I \equiv \frac{u'}{U} \tag{56}$$

where u' is the root-mean-square of the turbulent velocity fluctuations and U is the mean velocity and intensity in a 2D flow is described by:

$$I \equiv \frac{\sqrt{\frac{1}{2}\left(\langle u'^2 \rangle + \langle v'^2 \rangle\right)}}{U} \tag{57}$$

Much less effort has been expended examining the transition to turbulence in the oscillatory flow occurring in an orbital shaker device. Gardner and Tatterson (1992) injected die in the system and visually observed the dye in flow to detect turbulence. They calculated a homogenization number based on rotational speed and mixing time and compared it with Reynolds number. They found 3 flow patterns, a laminar pattern, a transitional pattern, and a turbulent flow pattern is the. Ducci *et al*. (2014) used PIV to examine the turbulence transition inside a dish on an orbital shaker. They used tall dishes and fluid heights to facilitate getting data in the XZ plane. Using a modified version of turbulence intensity, they looked at the turbulence transition versus Reynolds number and Froude number and found better agreement versus Froude number. The transition to turbulent has not been fully described for the oscillatory flow in orbital shaker systems, and little is understood about the effect of turbulence on WSS.

CHAPTER III

THEORY

3.1. THEORETICAL DEVELOPMENT OF ANALYTICAL SOLUTION OF SHEAR IN AN ORBITING DISH

3.1.1. Analytical Solution for Shear in Viscous Flow

For low Stokes number, low Froude number, low Slope Ratio, and low Reynolds number, flow far from the sides of the dish is that of a viscous fluid layer responding to two-dimensional oscillation of a flat plate (Berson *et al*., 2006). The Navier-Stokes equation in an inertial reference frame orbiting with position $\mathbf{R} = R(\cos \omega t, \sin \omega t)$ is

$$\frac{D\mathbf{V}}{Dt} - \mathbf{R}\omega^2 = -\frac{1}{\rho}\nabla p^* + \nu\nabla^2\mathbf{V} \qquad (58)$$

where $p^* \equiv p - \rho g z$ and g is the acceleration of gravity. For this problem, the height H of the free surface is assumed constant. The plate below the fluid orbits with the coordinate system, for boundary conditions at $z = 0$ of $\mathbf{V}(0,t) = 0$. At the free surface $z = H$, shear is zero $\frac{\partial \mathbf{V}}{\partial z} = 0$

. For the infinite fluid layer, $w = 0$ and $\frac{\partial u}{\partial x} = \frac{\partial u}{\partial y} = \frac{\partial v}{\partial x} = \frac{\partial v}{\partial y} = \frac{\partial p^*}{\partial x} = \frac{\partial p^*}{\partial y} = 0$. For quasi-steady flow, the Navier-Stokes equation simplifies to

$$\mathbf{R}\omega^2 = -\nu\nabla^2\mathbf{V} \qquad (59)$$

44

Now assuming a separable solution $\mathbf{V} = V_0(z)\mathbf{R}(t)$ gives

$$R\omega^2 = -v\frac{\partial^2 V_0}{\partial z^2} \tag{60}$$

Integrating twice with the stated boundary conditions gives

$$V_0 = -\frac{R\omega^2 h^2}{2\upsilon}\left(\frac{z^2}{h^2} - 2\frac{z}{h}\right) \tag{61}$$

thus the components of horizontal velocity become

$$\mathbf{V}(z,t) = -\frac{R\omega^2 h^2}{2\upsilon}\left(\frac{z^2}{h^2} - 2\frac{z}{h}\right)(\cos\omega t, \sin\omega t) \tag{62}$$

This velocity is shown in Figure 3.1 for time $t = 0$. Wall shear stress is

$$\vec{\tau}_w = \mu\vec{\gamma} = \rho R\omega^2 h(\cos\omega t, \sin\omega t) \tag{63}$$

and resultant wall shear stress is

$$\tau_w = \mu\acute{\gamma} = \rho R\omega^2 h \tag{64}$$
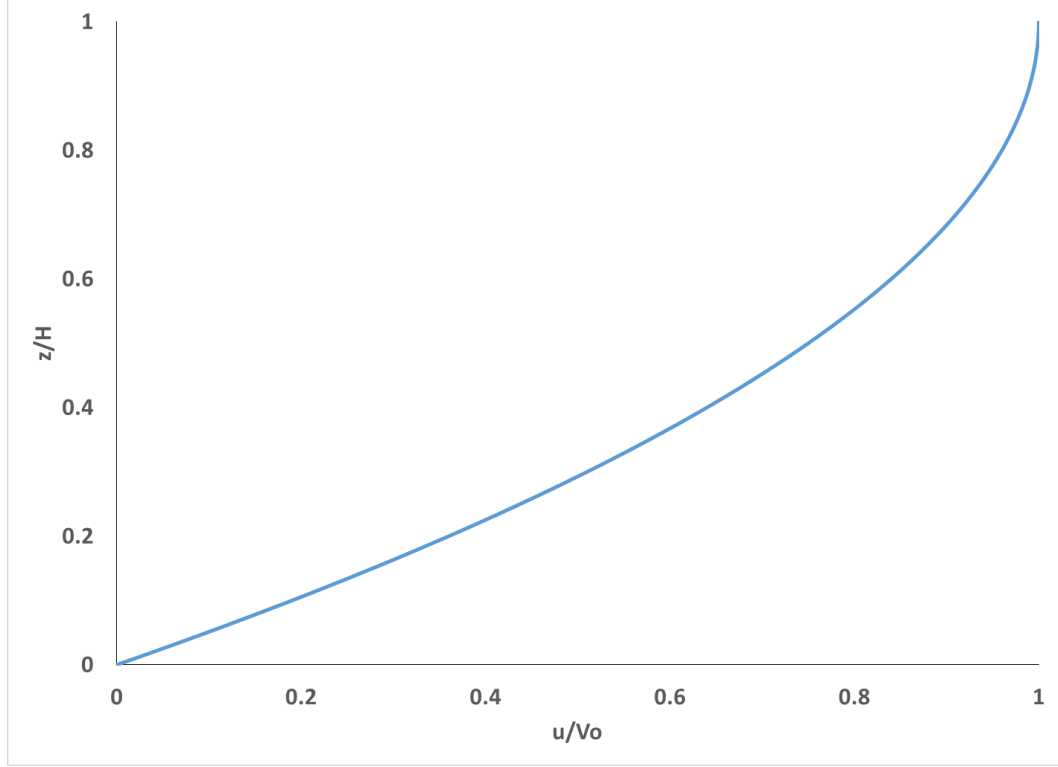
Figure 3.1. Viscous profile velocity relative to the dish versus normalized fluid height at time
$t = 0$.

3.1.2. Analytical Solution for Shear in Unsteady Flow

For high Stokes number, low Froude number and low Slope Ratio, low Reynolds number flow far from the sides of the dish is described by an extension of Stokes second problem to two-dimensional oscillation of a flat plate (Berson *et al.*, 2006). Where the plate motion imposed at $z = 0$ in a fixed (non-inertial) reference frame is $\mathbf{V}(t) = U(-\sin\omega t, \cos\omega t)$ and $U = R\omega$ is the amplitude of the plate velocity, the absolute velocity of the fluid above the plate is given by

$$\mathbf{V}(z,t) = U\exp\left(-\sqrt{\frac{\omega}{2\upsilon}}z\right)\left[-\sin\left(\omega t - \sqrt{\frac{\omega}{2\upsilon}}z\right), \cos\left(\omega t - \sqrt{\frac{\omega}{2\upsilon}}z\right)\right] \qquad (65)$$

thus the velocity relative to the orbiting plate is

46

$$\mathbf{V}(z,t) = U \exp\left(-\sqrt{\frac{\omega}{2\upsilon}}z\right)\left[-\sin\left(\omega t - \sqrt{\frac{\omega}{2\upsilon}}z\right), \cos\left(\omega t - \sqrt{\frac{\omega}{2\upsilon}}z\right)\right]$$

$$+ U\left(\sin \omega t - \cos \omega t\right)$$

(66)

The components of relative velocity are shown in Figures 3.2 and 3.3 for time $t = 0$.
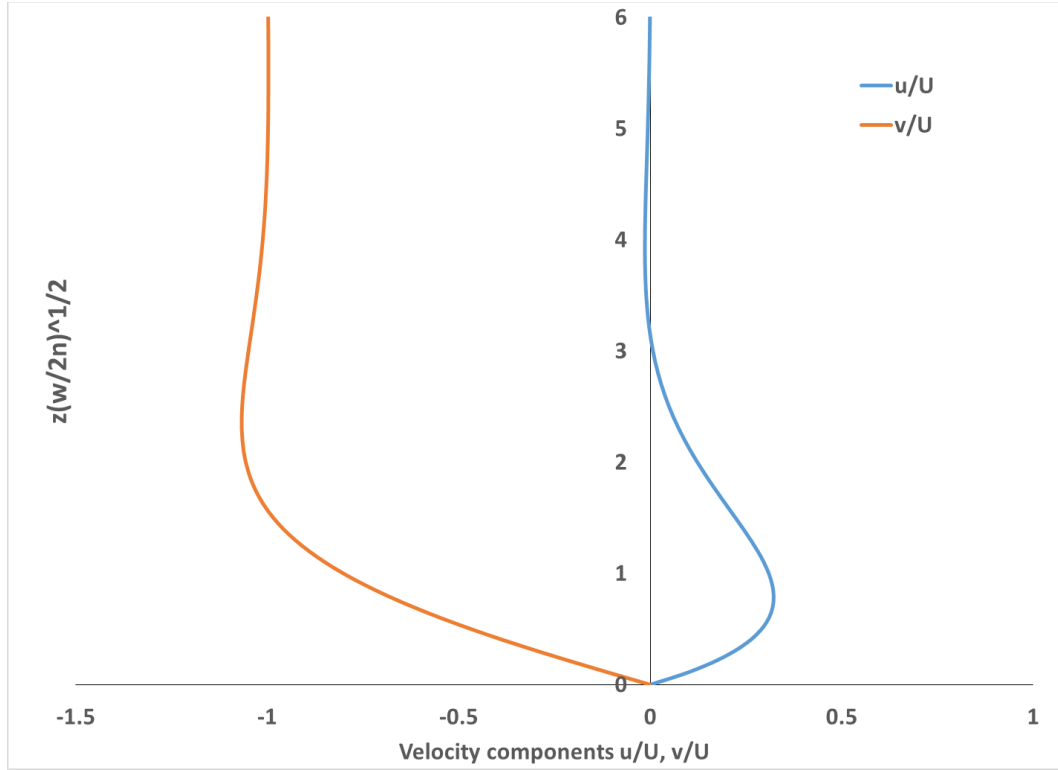
Figure 3.2. Inertial velocity component profiles versus normalized fluid height at time $t = 0$.
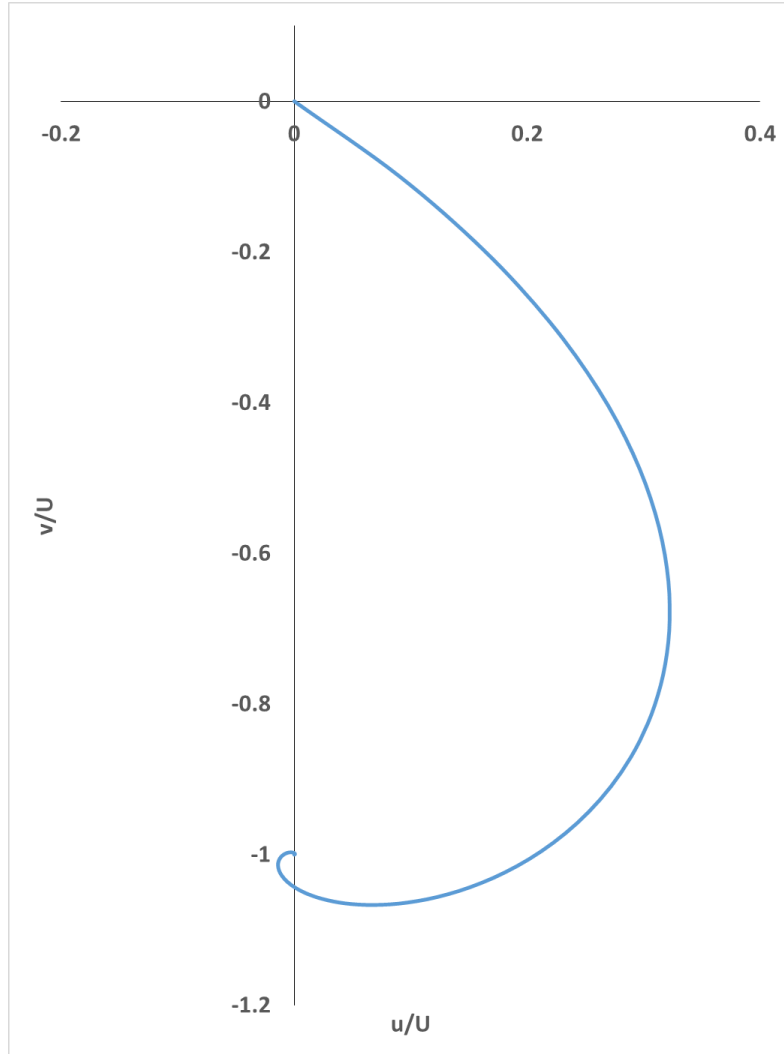
Figure 3.3. Inertial velocity profile viewed from above the plate at time t = 0.

The velocity gradient becomes

$$\frac{\partial \vec{v}(z,t)}{\partial z} = U\left(\sqrt{\frac{\omega}{2\upsilon}}\right)\exp\left(-\sqrt{\frac{\omega}{2\upsilon}}z\right)\left\{\begin{array}{l}\cos\left(\omega t - \sqrt{\frac{\omega}{2\upsilon}}z\right) + \sin\left(\omega t - \sqrt{\frac{\omega}{2\upsilon}}z\right), \\ \sin\left(\omega t - \sqrt{\frac{\omega}{2\upsilon}}z\right) - \cos\left(\omega t - \sqrt{\frac{\omega}{2\upsilon}}z\right)\end{array}\right\} \tag{67}$$

so that at the wall the velocity gradient is

48

$$\breve{\gamma} = \frac{\partial \vec{v}(z,t)}{\partial z}\bigg|_{z=0} = U\sqrt{\frac{\omega}{2\upsilon}}\left(\cos\omega t + \sin\omega t, \sin\omega t - \cos\omega t\right) \tag{68}$$

Now using the dish velocity magnitude $U = R\omega$, wall shear stress is

$$\vec{\tau}_w = \mu\vec{\breve{\gamma}} = R\sqrt{\frac{\rho\mu\omega^3}{2}}\left(\cos\omega t + \sin\omega t, \sin\omega t - \cos\omega t\right) \tag{69}$$

and the (scalar) resultant wall shear stress is

$$\tau_w = \mu\acute{\gamma} = R\sqrt{\rho\mu\omega^3} \tag{70}$$

This is Ley's result (Ley *et al.*, 1989).

49

CHAPTER IV

MATERIALS AND METHODS

4.1. OVERVIEW OF WORK PLAN

This work sought to describe fluid behavior in orbiting culture dishes resulting from motion imparted by an orbital shaker apparatus through CFD modeling. Validation of the CFD model was performed in the first part of this work. The model was first compared with limited experimental Doppler velocimetry data published by Dardik (2005) and an analytical solution. To more comprehensively validate the model, velocity vectors were measured using PIV and compared with velocities from CFD and an analytical solution.

Conditions that define the transition to turbulence is highly beneficial to understanding fluid behavior in an orbiting culture dish. In the last part of this work, turbulence intensities were determined from PIV measurements and plotted against Reynolds, Stokes, Stokes-Reynolds, Slope Ratio, and Froude numbers to determine which dimensionless parameter best defined the turbulence transition.

4.2. CFD MATERIALS AND METHODS

4.2.1. Simulation Setup

4.2.1.1. Simulation Hardware

Simulations were performed using Speed School of Engineering's Adelie Computer network, a 64 bit Linux cluster parallel system based on the AMD Opteron processor. The system consisted of 6 nodes with a total of 12 processors yielding 43 Gigaflops of aggregate

processor speed. Adelie contained 24 GigaBytes of memory, and 2.2 TeraBytes of disk storage. The operating system for Adelie was SUSE LINUX 9.1 Professional Edition.

4.2.1.2. Generation of Orbital Motion

FLUENT version 12.1.2 is a commercial CFD software package that models fluid flow for any geometry. FLUENT was written in the C computer language but uses an interactive, menu driven interface for user access to the functions required to generate a solution and display results. The FLUENT solver was capable of modeling: 2D or 3D, steady state or transient, laminar or turbulent, incompressible or compressible, and Newtonian or non-Newtonian flow. The program solved the equations for conservation of mass and momentum which were previously described in equations (11) and (12).

While fluid motion was periodic and separable, a more prudent approach was adopted in developing the model as an unsteady laminar flow problem in FLUENT 12.1.2. The orbit of the dish was specified in a user-defined function (UDF) in terms of the orbital frequency and orbital radius. Simulating flow in a dish required a dynamic grid that moved through space. The dish geometry and mesh of the dish were created in the preprocessor GAMBIT. Free surface tracking was accomplished with the (VOF). Figure 4.1 indicates the orbital motion in a Petri-dish throughout one orbit.
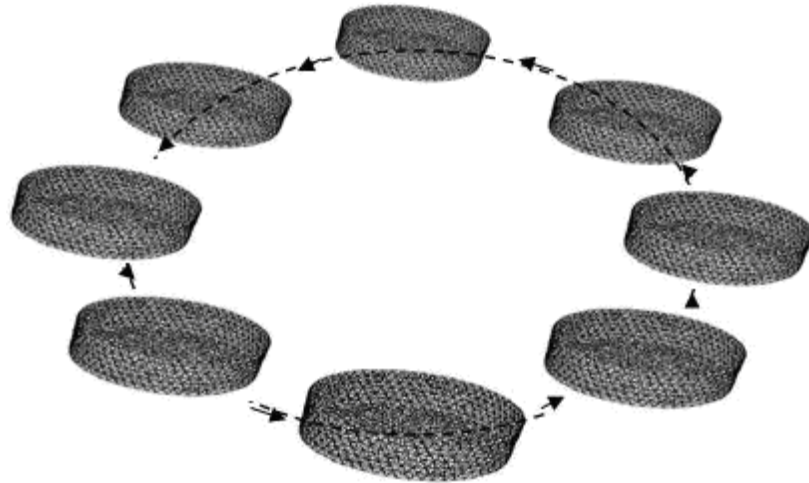
Figure 4.1. Model of Orbital Motion of Dish.

4.2.1.3. Mesh Generation

Opened the GAMBIT preprocessing software. The Petri dish was modeled as a closed cylinder. The diameter of the cylinder was predetermined from dimensionless parameters used for the case. The height was arbitrarily set as the lowest value where fluid will not strike the top of the cylinder (note that too shallow of a dish will develop an unsolvable model because the fluid will hit the top and too tall a dish will increase computational time as computational effort is wasted on the air region where nothing important occurs). Create a cylinder in GAMBIT by opening the Volume menu by left clicking the Volume Command Button in the Geometry menu. In the Volume menu, right click on the Create Volume button and selecting cylinder. Set Height and Radius 1 to predetermined values and click Apply; Radius 2 was ignored in the cylinder creation.

Once the cylinder was created, a mesh was applied to allow calculations to occur in FLUENT. Approximately 300,000 cells were used for good accuracy at a reasonable calculation time (note that the exact number of cells will vary slightly from case to case). The use of 300,000 cells was determined from FLUENT's recommendation that increasing the cell count until a further increase by five percent changes the results by less than or equal to 0.1 percent. The mesh was created in three steps to allow control of the cells based on

52

height to diameter ratio. Mesh controls are accessed by left clicking the Mesh Command Button. First, a mesh was applied to the radial edge of the cylinder. The Mesh Edges menu was activated by left clicking the Edge Command Button in the Mesh menu. A Mesh Edges window appeared below the Edge menu. Select the base of the cylinder; edge.1 showed up in the yellow Edge window. Under spacing, right click on the tab that displays Interval Size and select Interval Count. The exact Interval Count required was initially unknown and trial and error was utilized to find an Interval Count to yield approximately 300,000 cells. Input the Interval Count and then left click Apply to apply the edge mesh to the base.

Next, a mesh was applied across the curved outer surface of the cylinder. The Mesh Faces menu was triggered; left click the Face Command Button in the Mesh menu. Selected face.2, the curved face on the dish. Input the desired projected intervals into the newly appearing Projected Intervals input box. The Projected Interval was selected from an algorithm based on cylinder height and diameter (the algorithm is located the Appendix). Left click Apply to apply the face mesh to the curved face. Finally, the complete volume mesh was created. The Mesh Volumes menu was activated; by left click the Volume Command Button in the Mesh menu. Select the cylinder volume and click Apply to complete the volume mesh.

Examined the number of mesh volumes in the Transcript. If the value was not close to 300,000, click the Undo button in the Global Control Menu until all layers of the mesh were removed and then repeat with an adjusted interval count on the base edge. Once an acceptable mesh was created, it was exported to a file type usable by FLUENT.   To export the mesh, click on File, Export, and then Mesh. Type a name in new Export Mesh File window and click Accept to export the mesh. GAMBIT now was closed.

4.2.1.4. Case Set-up Procedure

Open the 3D version of FLUENT software. To import the mesh created in GAMBIT, click File, Read, and then Case; a Select File window opened. Under Files, left click on the .msh file and then left click on OK. While the Petri dishes used here was measured in centimeters, Fluent defaults all length units to meters. Default units were changed by clicking on Grid and then Scale. In the Scale Grid window: click on the down arrow, select "cm", click on Change Length Units, click on Scale and click Close to close the window. The solver must be set to unsteady state to operate properly. Click Define, Models, and then Solver to open the Solver window. Under Time, click Unsteady and then click OK to close the window.

The cylinder contained both air and water so Fluent must be set to multiphase operation. Click Define, Models, and Multiphase to open the Multiphase Mod window. Under Model, click Volume of Fluid and then click OK (note that several forms will appear, but they may be ignored). The materials in the dish must be specified. Air was preloaded, but liquid water has to be added. Click Define and then Material to open the Materials Window. Click Fluid Database to open the Fluid Database Materials window. Scroll down under Fluent Fluid Materials and select water-liquid, click Copy and then click Close. Click on Close to close the Materials window.

With materials selected, they needed to be assigned to the respective phases. Clicked Define and then Phases to open the Phases window. For most efficient calculation, set the primary phase as air and the secondary phase as water. To set a phase, selected the Phase and then clicked Set; a window for either the Primary or Secondary phase will appear. Selected the desired material from the Phase Material drop down box and type its name in the Name box. Clicked OK to set the phase. When both phases were set, click Close.

Now that the phases were set, operating conditions in the cylinder were then set. Click Define and then Operating Conditions to open the Operating Conditions Window. Under Reference Pressure Location, type a value just less than the height of the dish in the z direction (for example if a dish is 6 cm tall, set at 5.9 cm; set at top so reference pressure region was always occupied by air). Click Gravity in the Gravity menu to open the Gravitational Acceleration form. Input -9.81 m/s^2 for the z component then click OK.

Now that the operating conditions were set on the cylinder, motion could be added. Motion was created as a User Defined Function (UDF) in C++ code. After a UDF was created, it was loaded into Fluent. An example of the UDF used is in the Appendix; the only portion of the code which changes is the orbital speed (ω) in radians per second (note that in the code w is used in place of ω). To load the UDF, click Define, User-Defined, Functions, and then Compiled to open the Compiled UDF Window. Under Source Files, click Add to open the Select File window. Select the UDF file and click OK. Next to Library Name type mdmlib_ followed by a descriptive term for the case and then click Build to construct the library e.g. mdmlib_slope.1. The mdm library must be in the same directory that FLUENT is running from or the motion will not be utilized during computation. After the library is built, click Load to load the library.

The motion was now attached to the mesh. First, the Dynamic Mesh was activated. This was accomplished by clicking Define, Dynamic Mesh, and then Parameters to open the Dynamic Mesh Parameters Window. Click Dynamic Mesh under Models and click OK. Now the motion was attached to the fluid and to the cylinder. Click Define, Dynamic Mesh, and then Zones to activate the Dynamic Mesh Zones window. Under Zone Names selected fluid, check that the motion is present under Motion UDF/Profile and click Create. Repeat for the wall zone and click Close.

The interior of the cylinder initially contains air throughout its interior. A separate region was created to represent the fluid; the fluid was introduced as a volume patch. To patch a volume to a region, first the solver was initialized. To initialize the solver, click Solve, Initialize, and then Initialize to open the Solution Initialization window. Click Init and then Close to initialize the solver. Now select the region to change to fluid by clicking Adapt and then Region to open the Region Adaptation window (Figure 4.2). Under Input Coordinates, on X Min and Y Min input the negative cylinder radius, and input the cylinder radius for X Max and Y Max. Z Min remained 0 and Z max was the predetermined mean height of the fluid. Click Mark and then close to mark this region. The new marked region was now set as liquid. Click Solve, Initialize, and then Patch to open the Patch Window. Under Phase, click the down arrow and select water and then under Value type one. Under Registers to Patch select hexahedron-r0 then click Patch to patch the liquid to the base of the cylinder.
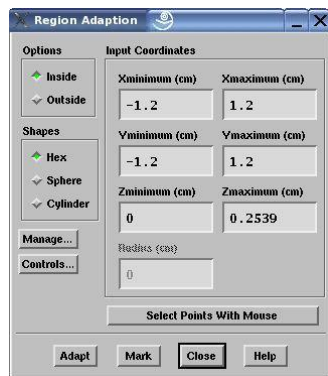
Figure 4.2. Region Adaptation menu in FLUENT.

Calculation parameters were now adjusted. The time step was set to allow for accurate computation. To adjust the time step, open the Iterate window by clicking Solve then Iterate. To set the time step, type 0.001 after Time Step Size and click Apply and then Close. This value was chosen for the time step because convergence problems occurred at larger increments. The methods the solver used to calculate the solution were adjusted in the

Solution Controls menu. This menu was accessed by clicking on Solve, Controls and then Solution. The parameters were set as follows: each of the Under-Relaxation factors were set at 0.3, the Pressure-Velocity Coupling was set as PISO, the Discretization for pressure was set as Body Force Weighted, and the Discretization for momentum was set as QUICK. Click OK to close. The Solution Controls menu can be seen in Figure 4.3. Lastly, the convergence criteria were set. Click Solve, then Monitor, then Residual to open the Residual Monitors window. Set the Residual for Continuity and x, y, and z velocities all at 0.0001. This value was determined by varying the residuals to find the quickest convergence without affecting the results.
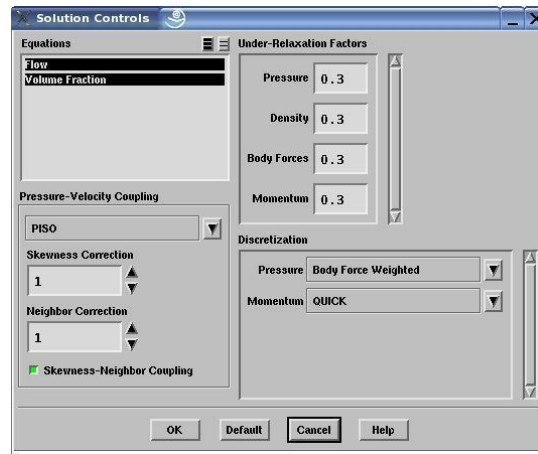
Figure 4.3. Solution Controls menu in FLUENT.

Before saving, the auto save feature was activated to allow investigation of the progress of a simulation while it was running. This feature tells FLUENT to save case and data files at predetermined intervals. The Autosave Case/Data window was open by clicking on File, Write, and then Autosave. Autosave Case File Frequency and Autosave Data File Frequency were equal, determined from the equation:

$$ASF = \frac{784.5}{\omega} \tag{71}$$

Enter an arbitrary value under Maximum Number of Each File Type. A large number was desired so that all time steps were saved. Finally, the Case and Data File were saved. Click File, Write, then Case and Data to open the Select File menu. Type a descriptive name for the case and click OK to save. Closed Fluent.

4.2.1.5. Batch Processing

To expedite convergence of case files, they were run in a batch mode on dedicated nodes on the Adelie supercomputer. Two files were needed to run a FLUENT case file in batch mode, a batch file and an input file. The batch file opened FLUENT and initialized it to run on a batch node. The sixth line of the batch file indicated the directory from where FLUENT reads the input file, and the seventh line dictated to which directory the output from FLUENT was read. Once FLUENT was initialized, operational commands were given in the input file. Lines one and two loaded the initial case and data file for the simulation. Line five set the number of time steps, and line six set the number of iterations per time step. To set the maximum number of iterations per time step for maximum convergence speed, it was usually advantageous to run a small number of time steps (five to ten) and then set the maximum roughly five iterations greater than the maximum observed. FLUENT bases the time allocation for a time step on the total number of iterations, therefore a large excess in iterations slowed down the process. Lines seven and eight recorded the final case and data files once the simulation was complete. An example of the batch and input file are located in the Appendix.

4.3. Dimensionless Parameters

4.3.1. Development of Dimensionless Parameters

To analyze how shear stress develops in an orbital shaker apparatus, seven dimensional independent parameters would be required: a is the cylinder radius, h is the static height of the fluid in the cylinder, R is the radius of orbit, ω is the angular velocity of orbit, g

is the acceleration of gravity, μ is the fluid viscosity, and ρ is the fluid density. A dish labeled with these seven parameters is seen in Figure 4.4. If cases were set up to view the effects of a change in each parameter at a low, medium, and high value, the total number of cases to view each combination of parameters would be 840. It would take an unreasonable computational effort to study this number of cases.

The challenge was to reduce the number of variables to decrease computational effort. Rance and Warren (1968) demonstrated that a dimensional analysis can reduce seven independent variables to four dimensionless parameters. You (1997) used this principle in studying sheet flow in oscillatory flow. Using experimental data, he reduced a model of oscillatory flow in a sediment bed containing seven variables to a dimensionless equation containing only four variables. By taking one of the variables as constant the dimensionless model was reduced to three independent dimensionless parameters.
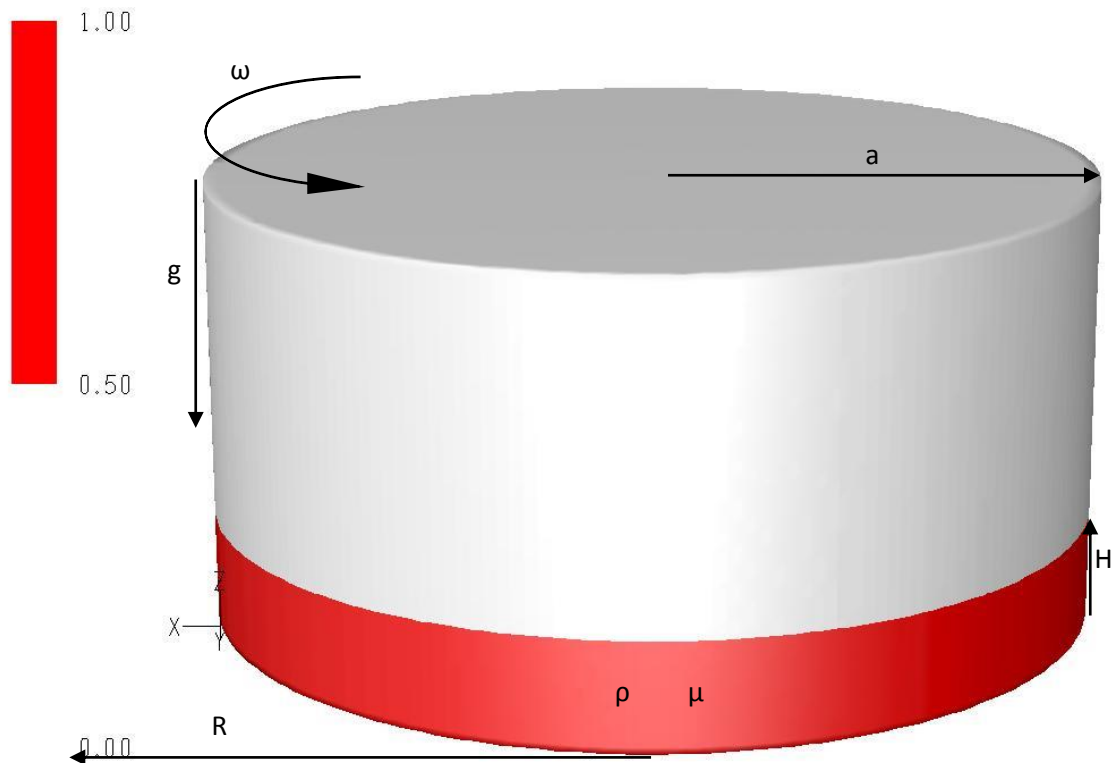
Figure 4.4. Dish with seven parameters labeled.

The system of study here can also be reduced to three dimensionless parameters. A dimensional analysis of the seven parameters yields four dimensionless parameters: the Reynolds number, the Stokes number, The Froude number and the Slope Ratio. Flow in the orbital shaker apparatus was assumed to be laminar flow at low Reynolds numbers as described by Hino *et al*. (1973). Therefore, a constant Reynolds number was used to reduce the number of parameters that affect how shear stress develops in an orbital shaker apparatus to three. With three independent dimensionless parameters, a detailed study can be created with only 27 cases.

4.3.2. Stokes Number

Irish mathematician George Gabriel Stokes defined the Stokes number. Stokes was a prolific force in the scientific community who co-developed the Navier-Stokes equations, one of the foundations of fluid dynamics. Starting in 1842, he began an interest in the field of hydrodynamics by studying motion of incompressible fluids (Wilson, 1987). In 1845 Stokes began investigating friction on fluids in motion. He furthered his research in 1850 to examine the effects of the internal friction of fluids on the motion. His findings explained many natural phenomena such as the suspension of clouds in air, and the subsidence of ripples and waves in water. As part of his studies on hydrodynamics, he calculated the terminal velocity for a sphere falling in a viscous medium. This calculation became known as the Stokes Law, which defined the frictional force exerted on spherical objects in a viscous fluid. Stokes examination of spheres in fluid also led to the development of the dimensionless Stokes number. Hinds (1998) states that the most common use of the Stokes number is in the aerosol industry where it is defined as the ratio of the stopping distance of a particle to a characteristic dimension of the obstacle, or:

$$St = \frac{\tau u}{d_c} \qquad (72)$$

For the system at hand, the Stokes number has a modified definition where it is defined as the ratio of inertial forces from the dish versus viscous forces from the fluid, or:

$$St = H\sqrt{\frac{\omega}{\nu}} \qquad (73)$$

In determining the Stokes transition, it is desired to understand the effects of low and high Stokes number on flow. For a low Stokes number, the fluid motion will be viscous dominated and the fluid wave will oscillate in phase with the cylinder motion. For high Stokes number, the flow will be inertially dampened, and the phase of the wave will lag behind the cylinder motion.

4.3.3. Froude Number

The Froude number was originally defined by English engineer William Froude in his Law of Comparison in 1868 (Brown and Lambert, 2004). Froude began studying the stability of ships in a seaway in 1861. He used a sequence of 3, 6, and 12 foot scale models to measure the resistance each model offered when towed at a given speed. The Froude number is the quantification of the resistance of floating objects and was developed so the results of small-scale tests could be used to predict the behavior of full-sized hulls.

The Froude number compares inertial and gravitational forces and is defined as a ratio of speed/length or:

$$Fr = \frac{u}{\sqrt{gH}} \qquad (74)$$

In an orbiting dish, the magnitude of the Froude number determines the steepness of the leading edge of the wave. For an extremely low Froude number, the leading edge has the same slope as the rest of the leading edge of the wave. As the Froude number increases

toward the transition, the slope of the leading edge becomes greater until a vertical wall is achieved. For high Froude numbers, the wave front becomes unsteady and develops into a perpetual standing wave similar in appearance to an ocean wave as it crashes on a beach and may eventually crash.

4.3.4. Slope Ratio

Slope is used to measure the steepness of a straight line, with a larger slope value signifying a deeper slope. In its most basic form, slope is defined as rise over run or (Finney, 2003):

$$m = \frac{\Delta X}{\Delta Y} \tag{75}$$

where slope is part of the equation of a line:

$$y = mx + b \tag{76}$$

For the system of study, the Slope Ratio is defined as the ratio of the quasi-steady free surface slope and the aspect ratio of the fluid at rest or:

$$Slope\ Ratio = \frac{Ra\omega^2}{gH} \tag{77}$$

The Slope Ratio affects the slope of the wave, with a greater slope resulting in a steeper wave. A small Slope Ratio represents a uniform slope across the trailing edge of the wave. When a large Slope Ratio is achieved, the slope of the trailing edge of the wave will become so great that part of the base of the cylinder will become dry. To counteract the drying, gravitational forces cause the trailing edge to extend to cover as much dry area as possible. The wave will no longer be uniform as the trailing edge of the wave becomes concave. The fluid is considered to have a high Slope Ratio when concavity is present.

4.4. VALIDATION AND TURBULENCE EXAMINATION MATERIALS AND METHODS

4.4.1. PIV Test Facility

The experiments were carried out in two 50 mm high cylindrical acrylic dishes: 38.1 mm and 76.2 mm in diameter. Both dishes were attached to an optically clear 304.8 mm x 304.8 mm x 3.2 mm acrylic sheet. The desired sheet was bolted to four 571.5 mm rods that were in turn attached to the platform of a Pro Scientific VSOS-4P orbital shaker. The orbital radius of the shaker is 0.95 mm. The optical rail that holds the camera was clamped to the side of the support structure. The test fluids were water with a viscosity of 0.001003 kg/m-s and a 5% (v/v) Tween80/water mixture with a viscosity of 0.0105315 kg/m-s. A schematic drawing of the dish and the shaker is shown in Figure 4.5.
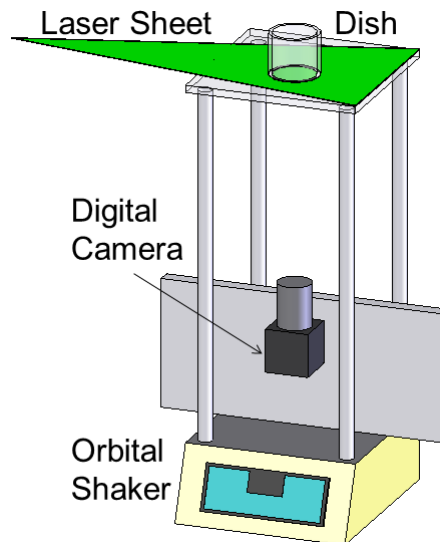
Figure 4.5. Schematic of orbital shaker apparatus for PIV.

4.4.2. PIV System

The PIV system records the fluid velocities at a horizontal plane inside the dish in a moving reference frame. The light source for the imaging system was created by a 600 mJ/pulse double-pulsed Nd-YAG laser (NewWave Research) operating at a wavelength of 532 nm. The laser was mounted on a stationary platform next to the shaker such that

the middle of the horizontal light sheet passed through the dish at a height of 0.5 mm. The laser illuminated neutrally buoyant 15 μm diameter fluorescent particles that were seeded into the fluid at a volumetric concentration of 0.2%. A TSI PowerviewPlus 4MP high-resolution digital camera, which was mounted on the optical rail, imaged the fluorescent particles in the plane of the laser sheet through the bottom of the dish. The camera was set to record two consecutive 2048 × 2048 pixel images with a temporal separation of 1.5-30 ms at a frame rate of 0.5 to 2.5 image pairs per second. A LaserPulse™ computer controlled synchronizer provided trigger signals for laser flashlamps and Q-switches, cameras, and frame grabbers.

Before performing experiments, a calibration target with black dots with known spacing was placed in the plane of the light sheet, and a picture of the target was taken with the high-resolution camera. These calibration images were then used to transform points in the image plane into the physical plane (plane of the light sheet), via an interpolation technique.

Velocity fields were sampled multiple times at 360 degree intervals of orbital phase so that each was in the same phase to allow for averaging of images. The field of view of the camera was about 45 mm × 45 mm yielding a nominal spatial resolution of 0.35 mm for the displacement data points. Images taken by the high-resolution camera were transferred to a desktop computer for processing.

Each set contained 79 image pairs. Insight3G software (TSI Inc.) was used to control all parameters of each PIV run. Once data collection was complete, Insight 3G was used to process the particle images and generate vector fields as .vec files. Post-processing was performed using several programs developed in MATLAB. The code

uses the vector files generated from Insight 3G along with calibration target information and the delta t between image pairs to calculate velocity or turbulent intensity.

4.4.3. Validation Work Plan

4.4.3.1. Comparison with Doppler Velocimetry from Dardik et al. (2005)

Dish dimensions, fluid properties, and orbital radius of the shaker were all defined equal to the same experimental parameters used by Dardik *et al.* (2005) since their work represents the limited experimental data that is currently available in the literature. A 3-D cylinder with a height of 20 mm and a radius of 17.5 mm was created in the pre-processor, GAMBIT, and then a mesh with 305,200 hexahedral computational cells was applied to the volume. The liquid in the dish was assigned a density of 997.3 kg/m^3 and a viscosity of 0.00101 kg/m-s. The air above the liquid had a density of 1.225 kg/m^3 and a viscosity of 1.7894*10-5 kg/m-s. The initial height of liquid in the dish was 2 mm. WSS was calculated for six cases covering the following orbital speeds: 60, 90, 120, 150, 180, and 210 RPM. At each rpm, that experimental data was compared with WSS from Fluent and WSS from Stokes Second Problem solution.

4.4.3.2. Validation with PIV

The experimental conditions were chosen to allow validation with respect to the Stokes second problem solution, which is valid for high Stokes number, low Slope Ratio, low Froude number and low Reynolds number. The resting fluid height, orbital speed, and fluid viscosity of the experiments were chosen to meet this requirement. The orbital speed was varied in 15 RPM increments from 30 RPM to 105 RPM. The resting fluid height for each case was 10 mm. Water had a viscosity of 0.001003 kg/m-s and density of 998.2 kg/m^3. The corresponding dimensionless parameters for each RPM are shown

in Table 4.1 as cases A through F. The Stokes number is high and each other parameter is low at these conditions.

Table 4.1. Water 10 mm dimensionless parameters for validation cases.

Case	RPM	Stokes	Slope	Froude	Reynolds
A	30	17.68	0.018	0.191	595.61
B	45	21.66	0.041	0.287	893.41
C	60	25.01	0.073	0.382	1191.22
D	75	27.96	0.114	0.478	1489.02
E	90	30.63	0.164	0.573	1786.83
F	105	33.08	0.223	0.669	2084.63

A case was setup in Fluent corresponding to each of the 6 cases. A 3-D cylinder with a height of 50 mm and a radius of 19.05 mm was created in the pre-processor, GAMBIT, and then a mesh with 303,347 hexahedral computational cells was applied to the volume. The liquid in the dish was assigned a density of 998.1 kg/m^3 and a viscosity of 0.001003 kg/m-s. The air above the liquid had a density of 1.225 kg/m^3 and a viscosity of 1.7894*10-5 kg/m-s. Normalized velocity vectors averaged over the entire surface are compared from PIV, CFD, and Stokes second problem solution.

4.4.4. Turbulence Assessment Work Plan

It was important to cover a wide range for each of the dimensionless parameters listed in section 4.3 to ensure that data was collected for laminar, transition, and turbulent regions for each of the parameters. A case can be made for each of the dimensionless parameters to be the governing parameter for turbulence. Hino *et al*. (1973) showed the Stokes number, Reynolds number, and Stokes Reynolds number to all have an effect on the turbulence transition in oscillatory flow so each of these parameters will be inspected against turbulence intensity. Froude number was shown in the literature to have strong correlation with data collected in the orbital shaker system. It is known that at high

Froude numbers crashing waves develop in the dish indicating turbulence. It imperative to also Froude number compare with turbulence intensity. There has been little investigation of the effects of varying the Slope Ratio, so it is unknown how it will describe turbulence. The free surface has been shown to change at high Slope Ratios which literature has shown can be an indicator of turbulence. It is prudent to also investigate Slope Ratio against turbulence intensity.

To determine where turbulence is present in the orbital shaker system, four parameters were varied in the PIV setup: resting fluid height, orbital velocity, dish size, and fluid viscosity to get a range of turbulence intensities. These parameters give a broad range of Froude numbers, Slope Ratios, Stokes numbers, and Reynolds numbers to examine. The test fluids were water with a viscosity of 0.001003 kg/m-s and a 5% (v/v) Tween80/water mixture with a viscosity of 0.0105315 kg/m-s. Three initial fluid heights were examined: 4 mm, 7 mm, and 10 mm. The two dishes had radii of 19.1 mm and 38.2 mm. The 12 sets of data from these fluids, fluids heights and dishes each have the orbital speed varied in 15 RPM increments from 30 RPM to 150 RPM. CFD cases at were also ran at these parameters so the free surface could be examined to further the turbulence investigation.

Turbulence intensities from the PIV experiments were examined as a function of dimensionless parameters to check for trends in turbulence. The Froude number, Slope Ratios, Stokes numbers, and Reynolds number for each case are shown in Tables 4.2-4.5 below. Stokes numbers are equal for both dish sizes, grow proportionally with fluid height, and are larger for water by a factor of 3.24. Stokes numbers range from 2.18 to 39.54. Slope Ratios are twice as large for the larger dish, grow inversely proportional

with fluid height, and are the same for each fluid. Slope Ratios range from 0.018 to 2.276. Froude numbers are twice as large for the larger dish, grow inversely proportional to the root of fluid height, and are the same for each fluid. Froude numbers range from 0.191 to 3.021. Reynolds numbers are twice as large for the larger dish size, grow proportionally with fluid height, and are larger for water by a factor of 10.5. Reynolds numbers range from 23 to 5956. This matrix of dimensionless parameters covers a wide variety of flow conditions and should allow viewing each parameter at low and high values.

Efforts were made to make error as minimal as possible in the PIV measurements. For each of the 108 experiments, data was collected at several delta t's to find the optimal time between exposures of the image pair to reduce noise and yield strong resolution. Temperature of the experiment was set constant to ensure consistent density and viscosity throughout each of the experiments. Particles were seeded slowly for each dish size to find the ideal particle density that gives strong resolution, but not seed too densely as to increase noise.

Table 4.2. <u>Dimensionless Parameters for turbulence assessment – 19.1 mm dish, water</u>.

	4 mm				7 mm				10 mm			
RPM	St	Sl	Fr	Re	St	Sl	Fr	Re	St	Sl	Fr	Re
30	7.1	0.05	0.30	238	12.4	0.03	0.23	417	17.7	0.02	0.19	596
45	8.7	0.10	0.45	357	15.2	0.06	0.34	625	21.7	0.04	0.28	893
60	10.0	0.18	0.60	476	17.5	0.10	0.46	834	25.0	0.07	0.38	1191
75	11.2	0.28	0.76	596	19.6	0.16	0.57	1042	28.0	0.11	0.48	1489
90	12.3	0.41	0.91	715	21.4	0.23	0.69	1251	30.6	0.16	0.57	1787
105	13.2	0.56	1.06	834	23.2	0.32	0.80	1459	33.1	0.22	0.67	2085
120	14.2	0.73	1.21	953	24.8	0.42	0.91	1668	35.4	0.29	0.76	2382
135	15.0	0.92	1.36	1072	26.3	0.53	1.03	1876	37.5	0.37	0.86	2680
150	15.8	1.14	1.51	1191	27.7	0.65	1.14	2085	39.5	0.46	0.96	2978

Table 4.3. Dimensionless Parameters for turbulence assessment – 19.1 mm dish, tween.

	4 mm				7 mm				10 mm			
RPM	St	Sl	Fr	Re	St	Sl	Fr	Re	St	Sl	Fr	Re
30	2.2	0.05	0.30	23	3.8	0.03	0.23	40	5.5	0.02	0.19	57
45	2.7	0.10	0.45	34	4.7	0.06	0.34	60	6.7	0.04	0.29	85
60	3.1	0.18	0.60	45	5.4	0.10	0.46	79	7.7	0.07	0.38	113
75	3.5	0.28	0.76	57	6.0	0.16	0.57	99	8.6	0.11	0.48	142
90	3.8	0.41	0.91	68	6.6	0.23	0.69	119	9.5	0.16	0.57	170
105	4.1	0.56	1.06	79	7.2	0.32	0.80	139	10.2	0.22	0.67	199
120	4.4	0.73	1.21	91	7.6	0.42	0.91	159	10.9	0.29	0.76	227
135	4.6	0.92	1.36	102	8.1	0.53	1.03	179	11.6	0.37	0.86	255
150	4.9	1.14	1.51	113	8.5	0.65	1.14	199	12.2	0.46	0.96	284

Table 4.4. Dimensionless Parameters for turbulence assessment – 38.2 mm dish, water.

	4 mm				7 mm				10 mm			
RPM	St	Sl	Fr	Re	St	Sl	Fr	Re	St	Sl	Fr	Re
30	7.1	0.09	0.60	476	12.4	0.05	0.46	834	17.7	0.04	0.38	1191
45	8.7	0.21	0.91	715	15.2	0.12	0.69	1251	21.7	0.08	0.57	1787
60	10.0	0.36	1.21	953	17.5	0.21	0.91	1668	25.0	0.15	0.76	2382
75	11.2	0.57	1.51	1191	19.6	0.33	1.14	2085	28.0	0.23	0.96	2978
90	12.3	0.82	1.81	1429	21.4	0.47	1.37	2502	30.6	0.33	1.15	3574
105	13.2	1.12	2.12	1668	23.2	0.64	1.60	2918	33.1	0.45	1.34	4169
120	14.2	1.46	2.42	1906	24.8	0.83	1.83	3335	35.4	0.58	1.53	4765
135	15.0	1.84	2.72	2144	26.3	1.05	2.06	3752	37.5	0.74	1.72	5360
150	15.8	2.28	3.02	2382	27.7	1.30	2.28	4169	39.5	0.91	1.91	5956

Table 4.5. Dimensionless Parameters for turbulence assessment – 38.2 mm dish, tween.

	4 mm				7 mm				10 mm			
RPM	St	Sl	Fr	Re	St	Sl	Fr	Re	St	Sl	Fr	Re
30	2.2	0.09	0.60	45	3.8	0.05	0.46	79	5.5	0.04	0.38	113
45	2.7	0.21	0.91	68	4.7	0.12	0.69	119	6.7	0.08	0.57	170
60	3.1	0.36	1.21	91	5.4	0.21	0.91	159	7.7	0.15	0.76	227
75	3.5	0.57	1.51	113	6.0	0.33	1.14	199	8.6	0.23	0.96	284
90	3.8	0.82	1.81	136	6.6	0.47	1.37	238	9.5	0.33	1.15	340
105	4.1	1.15	2.12	159	7.2	0.64	1.60	278	10.2	0.45	1.34	397
120	4.4	1.47	2.42	182	7.6	0.83	1.83	318	10.9	0.58	1.53	454
135	4.6	1.84	2.72	204	8.1	1.05	2.06	357	11.6	0.74	1.72	511
150	4.9	2.28	3.02	227	8.5	1.30	2.28	397	12.2	0.91	1.91	567

CHAPTER V

VALIDATION OF CFD MODEL

5.1. OVERVIEW OF VALIDATION

Validation was performed in stages. Preliminary validation was first performed on the earliest available experimental data in literature. CFD simulations were run to correlate experimental conditions of the work by Dardik *et al*. (2005). Computational WSS capabilities of the model were explored and compared with an analytical solution and WSS data generated from Doppler velocimetry. Doppler velocimetry provided WSS measurement at a single point on the dish at a time providing poor spatial resolution. Next, more comprehensive validation of the CFD model was obtained by comparing the computational results to both PIV and an analytical solution. PIV was utilized to measure the velocity field over an entire plane near the bottom of the dish. The computational and experimental results were also compared with an extension of Stokes second problem solution.

5.2. PRELIMINARY EXPLORATION OF MODEL AND VALIDATION WITH PREVIOSULY PUBLISHED DATA AND A LIMITED ANALYTICAL SOLUTION

5.2.1. Examination of WSS as a Function of Radius and Orbital Time

Oscillating resultant WSS magnitudes on the bottom of the cylinder are shown in Figure 5.1 for the 210 RPM case at radial locations of 16.4 mm, 12.8 mm, and 4.25 mm from the center of the dish for one complete orbit. Near the center of the dish (inside the inner circle in the WSS contour to the right of the plot), WSS magnitudes were relatively constant throughout a complete orbit. The amplitude of oscillation increased with increasing radius, reaching a peak in amplitude, as well as magnitude, near the side wall. Finally, in a narrow

band very close to the side wall (in the outer annular region in WSS contour), WSS decreased in response to the viscous layer on the side wall.
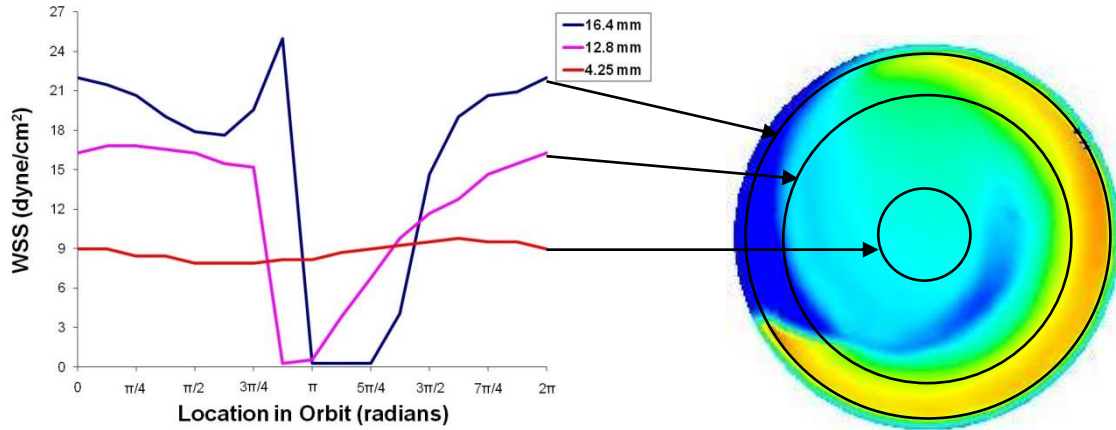

Figure 5.1. Resultant WSS magnitude for different radii at 210 RPM throughout one orbit (2π radians). The arrowheads indicate the radial position for each curve.

The overall non-uniformity of WSS across the dish found in these simulations correlates with differences previously observed in cellular responses based on location in the dish. For example, Dardik *et al*. (2005) measured increased cell proliferation and apoptosis rates, increased intercellular molecule adhesion expression, reduced Akt phosphorylation, and reduced E-selectin down-regulation for endothelial cells seeded in the center compared to endothelial cells seeded in the periphery of a dish. Levesque and Nerem (1985) observed rounded cells in the center of the dish (where WSS is low) and elongated cells near the edge of the dish (where WSS is high).

5.2.2. Examination of WSS as a Function of Orbital Velocity

Oscillating resultant WSS magnitudes are presented for low, medium, and high orbital velocities (60, 150, and 210 RPM) at three radii on the bottom of the dish in Figure 5.2 a-c. Values are plotted for one complete orbit. For a given radius, amplitudes of oscillation increased with increasing RPM, and were greater at radial locations farther from the center of the dish. At 60 RPM, WSS was nearly constant at about 0.4 dyne/cm^2 at all three radii. At 150 RPM, the peak WSS was ~ 6.5 dyne/cm^2 at 4.25 mm, ~ 9.5 dyne/cm^2 at

71

12.8 mm, and ~ 16 dyne/cm² at 16.4 mm. At 210 RPM, the peak WSS was ~ 9.5 dyne/cm² at

4.25 mm, ~ 17 dyne/cm² at 12.8 cm, and ~ 25 dyne/cm² at 16.4 mm. Shear values near zero

are present since the free surface is substantially thin at these locations and they lie on the

trailing edge of the wave were velocities are lower. Here, the free surface also falls below

the bottom most computation cell. However other areas that fall below the bottom most cell

report high shear values.
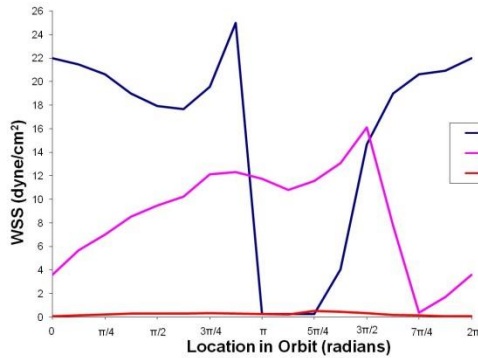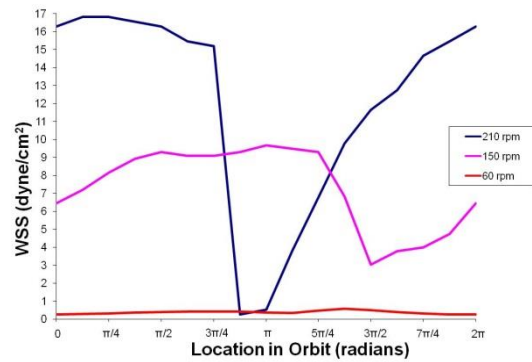
Figure 5.2-a   Figure 5.2-b
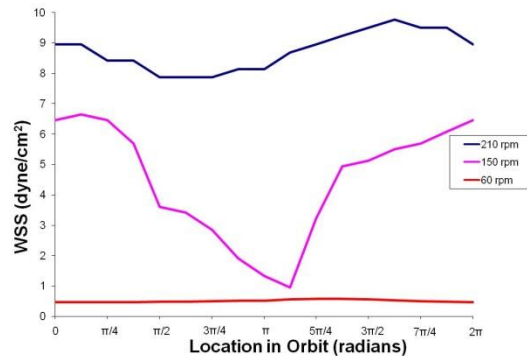
Figure 5.2-c

Figure 5.2. Resultant WSS magnitude as a function of radius and orbital velocity at radial
locations of 16.4 mm (a), 12.8 mm (b), and 4.25 mm (c) throughout one orbit.

5.2.3. Comparison with Analytical Solution

The Stokes second problem solution (as quantified in Equation 10) provides an

estimate for the (constant) resultant WSS magnitude for regions of the flow that are not

influenced by the sides of the dish. To best match the conditions for which Stokes second

problem is valid, listed in chapter II, the WSS magnitudes at the center of the dish were

selected from the computational model and compared with the analytical solution (Figure

5.3). The area average WSS magnitudes from the computational model were also compared with the analytical solution. WSS values obtained using Equation (10) followed a similar trend to the computational center WSS magnitudes throughout the range, but were $0.99 \pm$ 0.42 dyne/cm^2 higher. At 60 and 90 RPM, the center WSS magnitudes matched the area average WSS values. At 120 RPM and higher, wall effects cause the area average WSS magnitudes to be greater than the center WSS values. The area average WSS magnitudes were also slightly higher than values from the Stokes second problem solution in this range. The area average WSS magnitudes were 0.10 ± 1.02 dyne/cm^2 higher than the Stokes second problem solution over the full range of orbital speed.
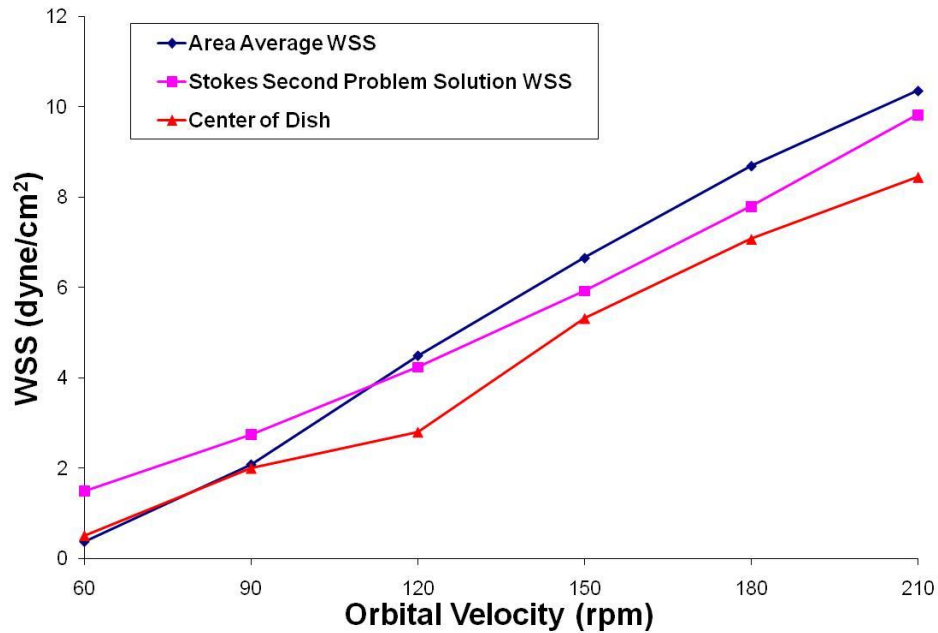
Figure 5.3. Comparison of area average WSS magnitude from the computational model with values from the analytical solution.

5.2.4. Comparison with Experimental Oscillatory WSS

The model was next compared to existing experimental WSS values (Dardik, *et al.* 2005) collected using a one-dimensional optical Doppler velocimetry probe, in this case aligned to measure the tangential component. Since the probe did not distinguish between positive and negative Doppler shifts, calculated WSS values were all positive. Dardik, *et al.*

73

(2005) reported scatter plots of Doppler shifts (all interpreted as positive) from the ultrasonic velocity probe for a single case (210 RPM) for many orbits. (Shear stress calculated from individual Doppler shift values was not reported.) The scatter plot data converted to WSS, is presented here for comparison with the computational data. The computationally determined oscillating tangential WSS magnitude for one orbit is superimposed over the WSS scatter plots in Figures 5.4 and 5.5. The scatter plots encompass 1400 orbits for the 12 mm radial measurement position and 1183 orbits for the 1 mm position. The sampling rates for these measurements provided one data point every 12.6 orbits at 1 mm from the center of the dish and one data point every 17.7 orbits at 12 mm from the center of the dish.

In Figure 5.4, the experimental minimum and maximum WSS at 12 mm from the center of the dish were 6 and 16 dyne/cm^2, respectively, whereas WSS generated from the computational model ranged from 0.5 to 14 dyne/cm^2. These match reasonably well in the upper range, but not as well in the lower range. Part of the discrepancy in the maximum value could arise since the experimental WSS values were collected in a region where the model predicts a sharp gradient in WSS in the radial direction. For instance at 210 RPM, using the simulated gradient at 12 mm, a 8 % (1 mm) error in measured radial position could result in a 16 % (1.9 dyne/cm^2) error in measured WSS.

Figure 5.4. Comparison of computational and experimental tangential WSS magnitudes at 12 mm from center of dish and 210 RPM.

With regard to the minimum values, the sampled computational WSS magnitudes extend nearly to zero, and with greater resolution the zero crossing could be found, while the experimental WSS magnitudes plateau much higher. There are two possible reasons for this phenomenon. First, with such a sparse sampling rate, it is possible the lowest point actually present in the experiment was not recorded during the sampling time. Second, it is also possible that the experimental probe did not pick up very low values that occur when the liquid layer was shallow over the probe. At these times, the number of TiO_2 particles over the Doppler probe would be small and scattering of the signal by the free surface would be strong enough that perhaps the signal could not be distinguished from noise and hence was not recorded by the experimental software.

In Figure 5.5, the measured minimum and maximum tangential WSS magnitudes at 1 mm from the center of the dish were 3 and 7 dyne/cm^2, respectively. The computational WSS magnitudes vary from 0.5 to 8.5 dyne/cm^2. The computational WSS values from 0 to $\pi/8$ and $5\pi/4$ to 2π are rectified negative values. These values do not match quite as well as

75

those from Figure 5.4. There are several possible reasons for the larger differences. First, both low and high WSS measurements may have been missed due to sparse sampling. Second, an error in locating the probe measurement volume, as discussed for the data in Figure 5.4, may have contributed to a reduction in average WSS, as well as WSS amplitude.
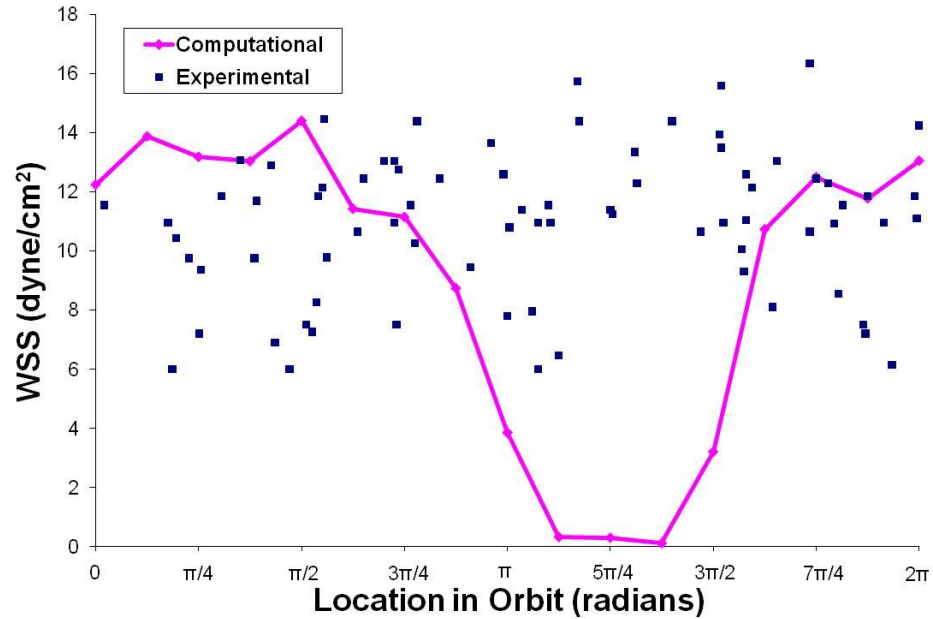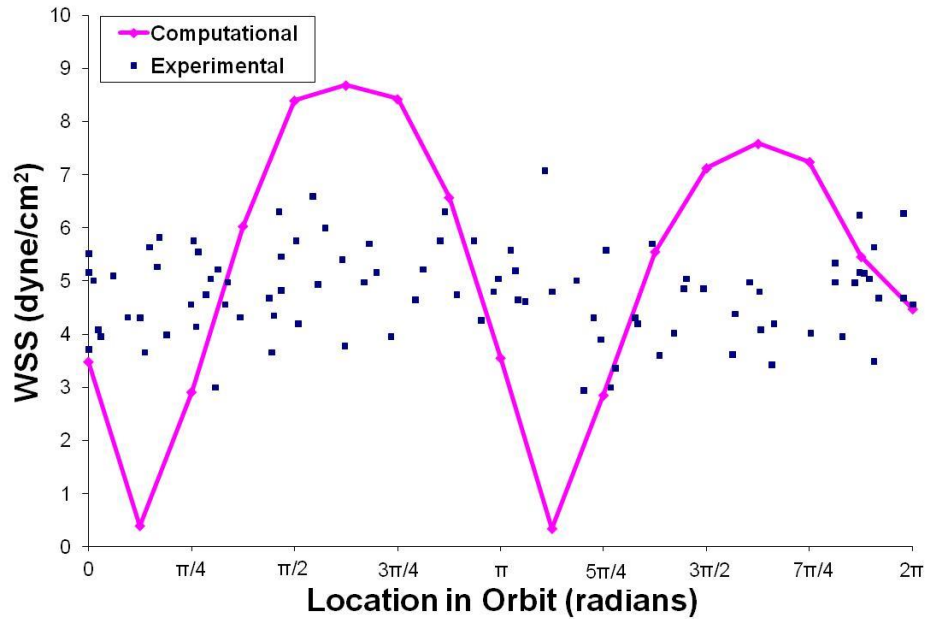

Figure 5.5. Comparison of computational and experimental WSS magnitudes at 1 mm from center of dish and 210 RPM.

5.3. VALIDATION WITH DATA OBTAINED FROM PIV

5.3.1. Comparison of CFD and PIV Velocity Magnitude Contours

CFD images show good qualitative agreement with the experimental results. The 60 RPM case is displayed in Figure 5.6. In each of the cases from A to F there is a large high velocity area near the center in an oval shape and lower values toward the edges. Velocity magnitudes extracted from the contours are plotted throughout one complete orbit for three radial locations in Fig. 5.7. The velocity magnitudes in Fig. 5.7 are normalized by the dish velocity magnitude $R\omega$. The values show close agreement throughout with average deviations between CFD and PIV of just 0.71 % at 10 % of the radius from the center of the dish, 1.74 % at 50 %, and 4.74 % at 70 %.

76
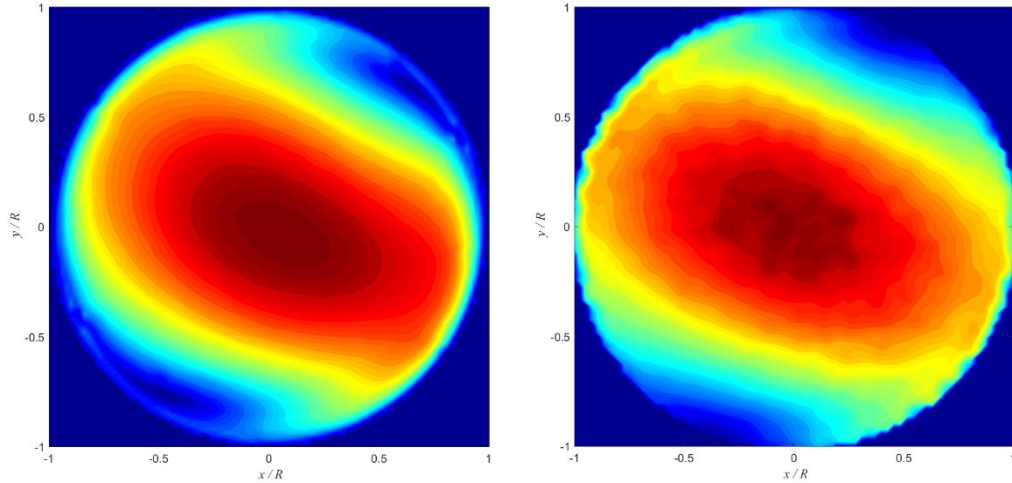
Figure 5.6. 60 RPM velocity magnitude contour - CFD (left) and PIV (right).
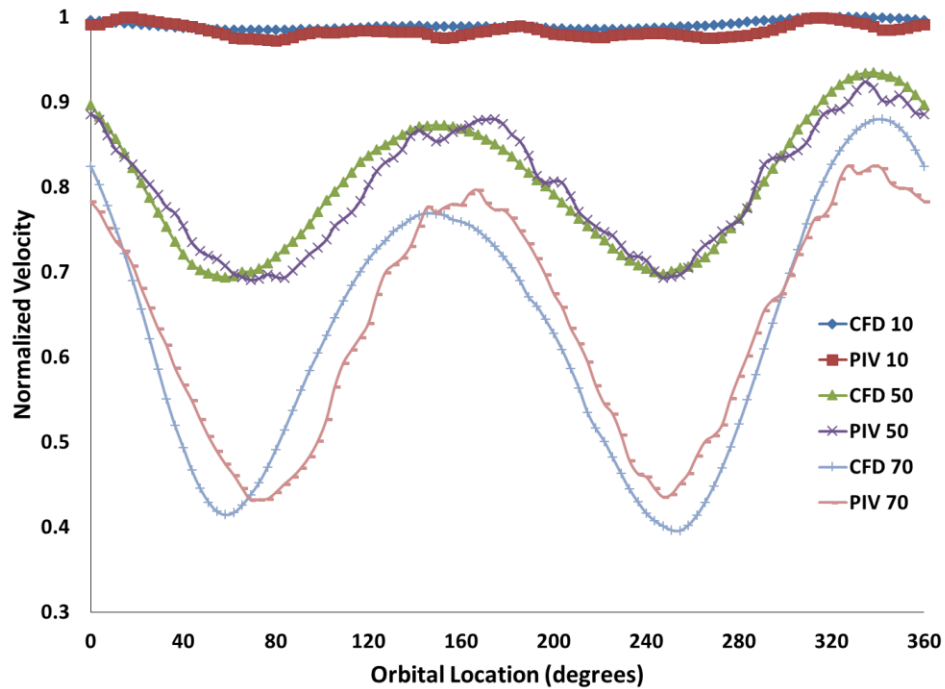
Figure 5.7. Comparison of normalized CFD and PIV velocities at 10 %, 50 %, and 70 % of the radius throughout one complete orbit for 60 RPM.

5.3.2. Comparison to Analytical Velocity Magnitude

The Stokes second problem velocity magnitude at z = 0.5 mm (determined from Equation 66) was used to normalize average velocity magnitudes from the inner 20 % of the radius at the same distance from the bottom of the dish from both the computational model and experimental data. Results from the three methods are compared in Figure 5.8. Error bars

in Figure 5.8 represent the standard deviation of experimental measurements from 79 randomly selected points from within 20 % of the radius.

Velocities from Equation 66 range from 2.98 cm/s at 30 RPM to 10.45 cm/s at 105 RPM. Computational central normalized velocity magnitudes were on average 0.21 ± 0.91 cm/s or 7.5 % higher while experimental central normalized velocity magnitudes were on average 0.35 ± 1.16 cm/s or 9.8 % higher (Table 5.1). The PIV and CFD velocities varied from each other over the range of orbital speeds on average by 8.4 %. Between 60 RPM and 105 RPM the CFD values were 12.1 % closer than PIV to the analytical solution, while varying from the analytical solution by an average of 16.9 %. For 30 RPM, the PIV value was 1.7 % closer than CFD to the analytical solution, while varying from the analytical solution by 10.6 %. For 45 RPM, the CFD velocity was 1.2 % higher than the analytical solution, and 6.6 % lower than PIV.
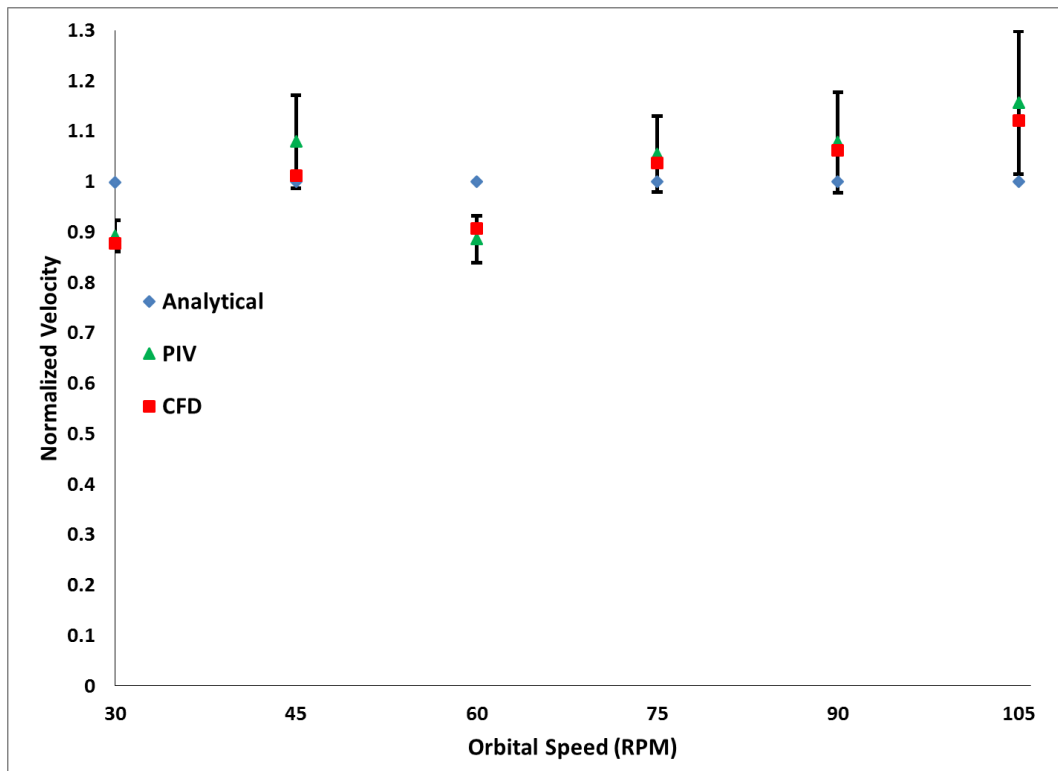
Figure 5.8. Comparison of analytical solution to CFD and PIV over six cases matching criteria for Stokes second problem solution.

Table 5.1. Error Between CFD, PIV, and Analytical Solution for Stokes second problem solution conditions.

Case	PIV - CFD	CFD - Analytical	PIV - Analytical
30 RPM	1.7%	-12.1%	-10.6%
45 RPM	6.6%	1.2%	7.9%
60 RPM	-2.3%	-9.3%	-11.4%
75 RPM	1.7%	3.7%	5.4%
90 RPM	1.4%	6.2%	7.7%
105 RPM	3.1%	12.2%	15.6%
Overall	8.1%	20.8%	25.2%

5.3.3. Velocity Profile Comparison

Figure 5.9 and 5.10 show normalized analytical and computational velocity components u/U and v/U, respectively, spanning normalized height $z(\omega/2v)^{1/2}$ from 0 to 10.44. This region near the wall is of interest as it has the most bearing on WSS and cell culture operations. The computational velocities were taken at the center of the dish. Both the analytical and computational velocities satisfy the no-slip boundary condition at $z(\omega/2v)^{1/2}$ of 0. In Figure 5.9, u/U values from the six computational cases follow a similar trend to the analytical equation with maximum values around a $z(\omega/2v)^{1/2}$ of 0.58 and u/U values that trend back near 0 at a $z(\omega/2v)^{1/2}$ of 3.57. The u/U values for the six cases vary from the analytical solution on average by -0.00046 ± 0.0015. In Figure 5.10, v/U values from the six computational cases also show good agreement to the analytical equation with maximum values around a $z(\omega/2v)^{1/2}$ of 2.32 and u/U values that trend back near -1 at a $z(\omega/2v)^{1/2}$ of 4.63. The v/U values for the six cases vary from the analytical solution on average by 0.0038 ± 0.0084.
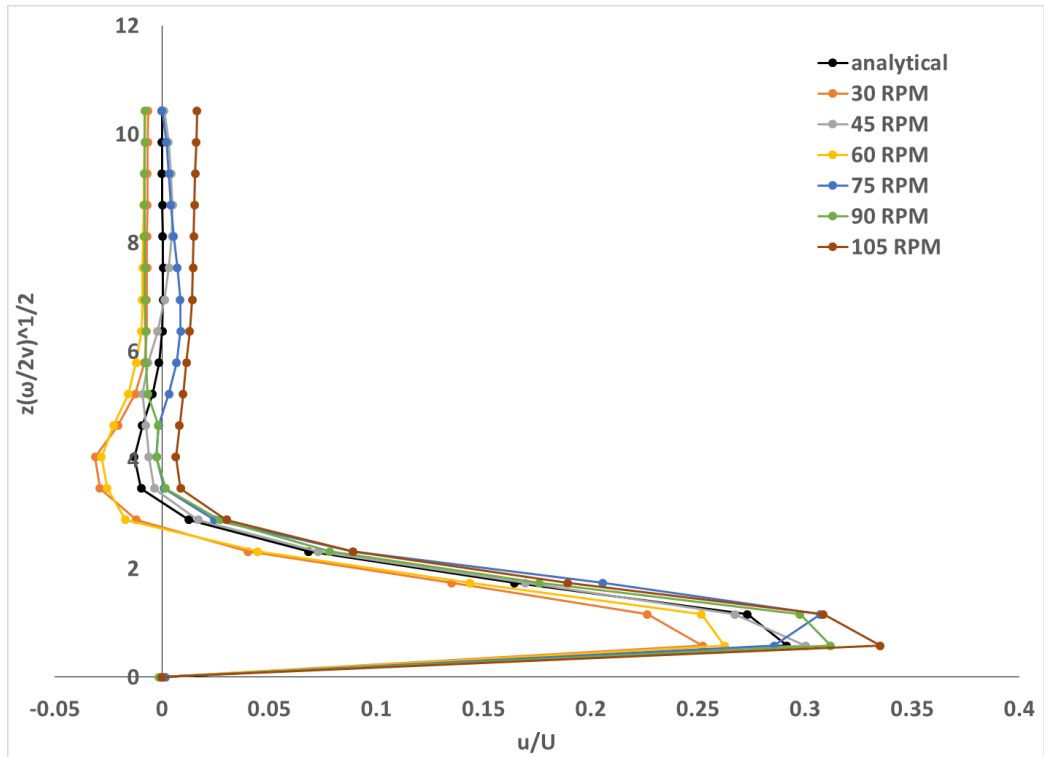
Figure 5.9. Comparison of analytical solution to computational u/U for each case from $z(\omega/2v)^{1/2}$ of 0 to 10.44.
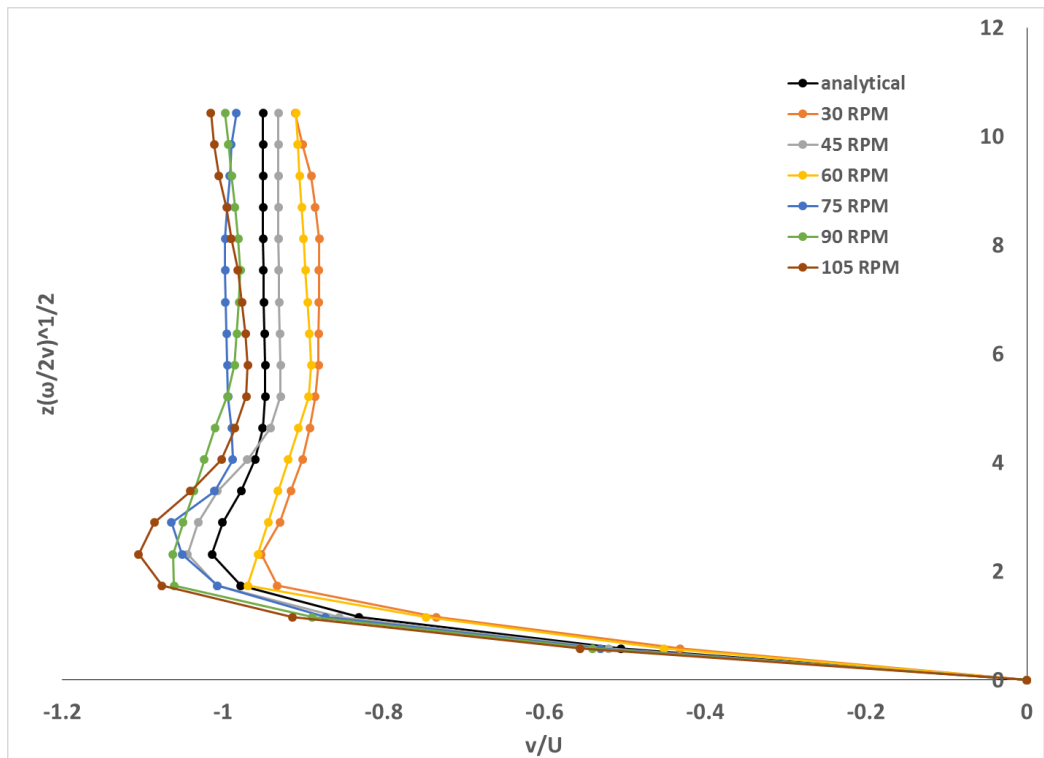
Figure 5.10. Comparison of analytical solution to computational v/U at for each case from $z(\omega/2v)^{1/2}$ of 0 to 10.44.

CHAPTER VI

TURBULENCE TRANSITION FOR FLOW IN AN ORBTING DISH

6.1. OVERVIEW OF TURBULENCE INVESTIGATION

A matrix with a wide range of dimensionless parameters was chosen for investigation into the turbulence transition and turbulence intensities calculated for each case. Turbulence intensity was plotted versus five dimensionless parameters in attempt to quantify turbulent conditions. CFD was utilized to examine if dimensionless parameter transitions and free surface shape had an effect on the turbulence transition. Lastly, other turbulence data published in literature for different flow conditions in the orbital shaker system were plotted against these same parameters as an additional means to examine transition over a broader range of conditions.

6.2. EXAMINATION OF TURBULENCE INTENSITIES

Using MATLAB, vector data from 108 cases was processed to give average turbulence intensities for each of the 79 image pairs that were collected for that test. Examining each of the nine plots of turbulence intensity versus image number for one data set gave an initial glimpse of the possibility of turbulence in those tests.

In these plots, a laminar case should exhibit steady low magnitude oscillations while turbulent cases should exhibit much higher magnitudes and more randomness in values. Figure 6.1 shows ones of the 12 sets of turbulence intensities versus image number data; nine cases for 19.1 mm, tween, and seven mm height. The intensity scales are equivalent on the ordinate of each plot. The Froude number for the cases increased from 0.23 to 1.14 for this

data set as RPM was increased. Case's (a) through (e), Froude numbers of 0.23 to 0.69, on Figure 6.1 all showed turbulence intensities with a somewhat similar amplitude. The maximum and minimum range of intensities for these cases were all between 0.005 and 0.05. This was a strong indication that these cases were in laminar flow. At case (f), Froude number of 0.8, the turbulence intensity oscillated less frequently than the lower Froude cases and the maximum turbulence intensity increased to 0.08. Looking at cases (g) through (i), as Froude number was increased, the maximum and average turbulence intensities increased and the variance between cases became more chaotic. The data indicate the presence of turbulence in this flow regime, and for this set of conditions flow became turbulent at a Froude number between 0.69 and 0.80.

(a) Fr=0.23   (b) Fr=0.34   (c) Fr=0.46

(d) Fr=0.57   (e) Fr=0.69   (f) Fr=0.80

(g) Fr=0.91   (h) Fr=1.03   (i) Fr=1.14
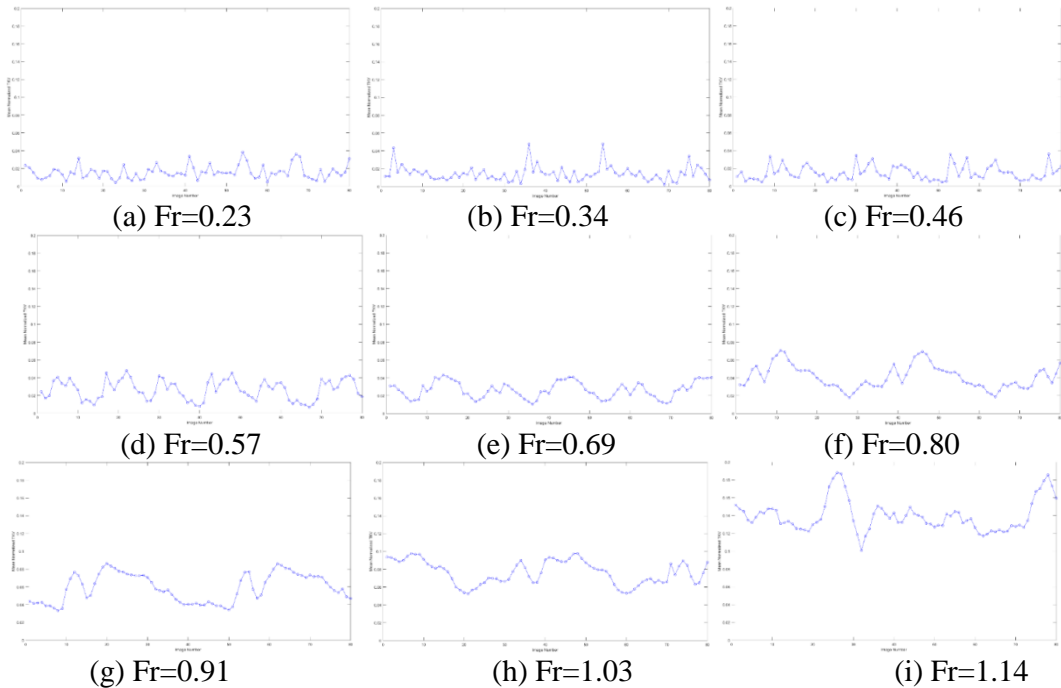
Figure 6.1. Average turbulence intensity raw data from 19.1 mm, tween, and 7 mm height.

6.3. DIMENSIONLESS ANALYSIS OF THE TURBULENCE TRANSITION

6.3.1. Analysis of Dimensionless Parameters

In the previous section, a transition from laminar to turbulent was observed in the orbital shaker system for the single data set of 19.1 mm, tween, and seven mm height. The

next step was to determine the effect, if any, each dimensionless parameter had on turbulence and the turbulence transition by plotting normalized turbulence intensities from each of the 12 data sets versus each of the four dimensionless parameters described in section 4.3: Stokes number, Reynolds number, Froude number, and Slope Ratio, as well as the Stokes Reynolds number which was derived from these. Hino *et al*. (1976) showed Reynolds number, Stokes number, and Stokes Reynolds number to strongly correlate with the turbulence transition for oscillatory flow in a pipe. Froude number was used as a defining dimensionless parameter often in experiments using orbital shakers for oscillatory flow, but its effect on the turbulence transition has not been investigated. Slope Ratio has not been examined for flow in orbital shakers, and its effects on turbulence transition are yet unknown.

The Reynolds's number has long been used to describe the transition to turbulence in fluid flows of all types, including oscillatory flows, so it was examined first. Figure 6.2 shows normalized turbulence intensity versus Reynolds number. There does not appear to be a correlation between normalized turbulence intensity and Reynolds number. There were six sets of data bunched together by fluid type and resting fluid height; the 19.1 mm dish had a much lower magnitude and Reynolds number range for each set than the 38.2 mm dish. These six sets varied in range of Reynolds number from 23 to 227 on the low end, to 625 to 5956 on the high end. The lower resting fluid heights and higher viscosity tween material had lower Reynolds numbers and, hence, these data fell on the left of the plot.
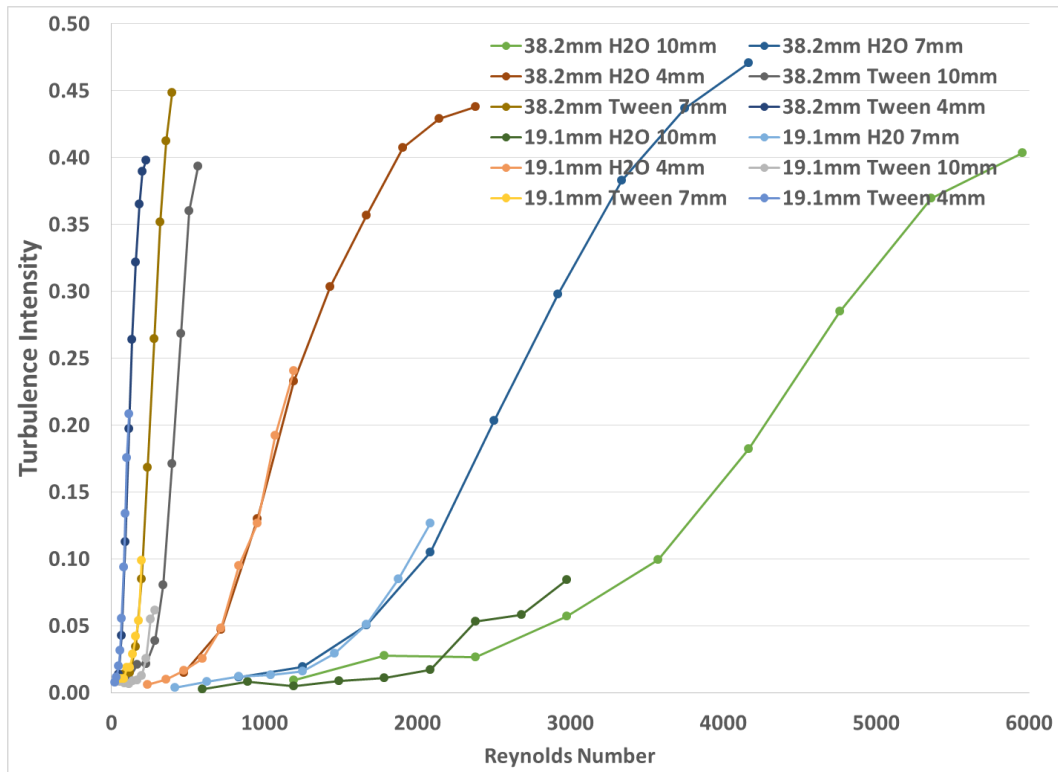
Figure 6.2. Turbulence intensity versus Reynolds number for 12 data sets.

Hino *et al*. (1976) showed that in oscillatory flow in a pipe that Stokes number strongly correlated with the turbulence transition. Figure 6.3 shows turbulence intensity versus Stokes number. As with Reynolds number, turbulence intensity does not appear to correlate with Stokes number. The six data sets with matching resting fluid height and material shared Stokes numbers for both dish sizes. However, the magnitude of turbulence intensity for the larger dish was much larger. These six sets varied in Stokes number range from 2.2 to 4.9 on the low end, to 17.7 to 39.5 on the high end. Similar to the Reynolds number, the lower resting fluid heights and tween material had lower Stokes numbers and, hence, these data fell on the left of the plot.
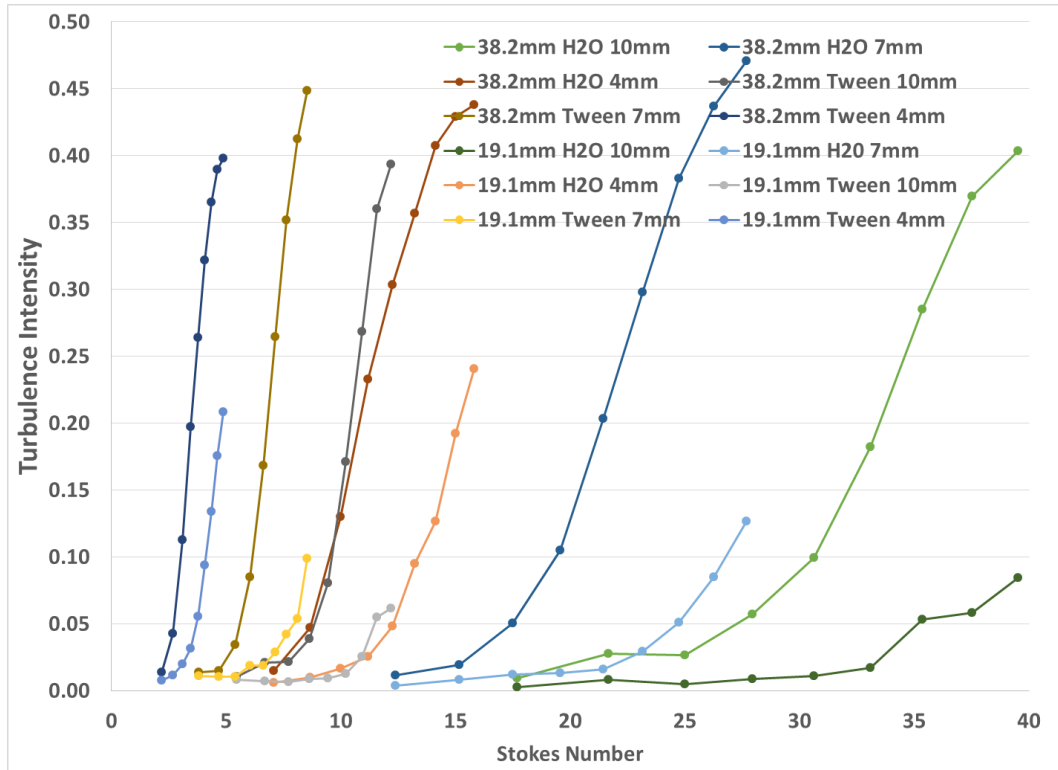
<u>Figure 6.3</u>. Turbulence intensity versus Stokes number for 12 data sets.

The Stokes Reynolds number best correlated with turbulence intensity and defined transition to turbulence of the three dimensionless parameters that Hino *et al*. (1976) investigated for oscillating flow in a pipe. Figure 6.4 shows turbulence intensity versus Stokes Reynolds number. As with the Reynolds number and Stokes number, the Stokes Reynolds number also showed poor correlation with turbulence intensity. Combinations of the same dish size and fluid seem to be grouped with the similar Stokes Reynolds number for each of the nine RPMs examined. Left to right on Figure 6.4 were the smaller dish with tween, larger dish with tween, smaller dish with water, and the larger dish with water. The Stokes Reynolds numbers varied from 5.2 to 11.6 on the low end, to 33.7 to 75.3 on the high end.
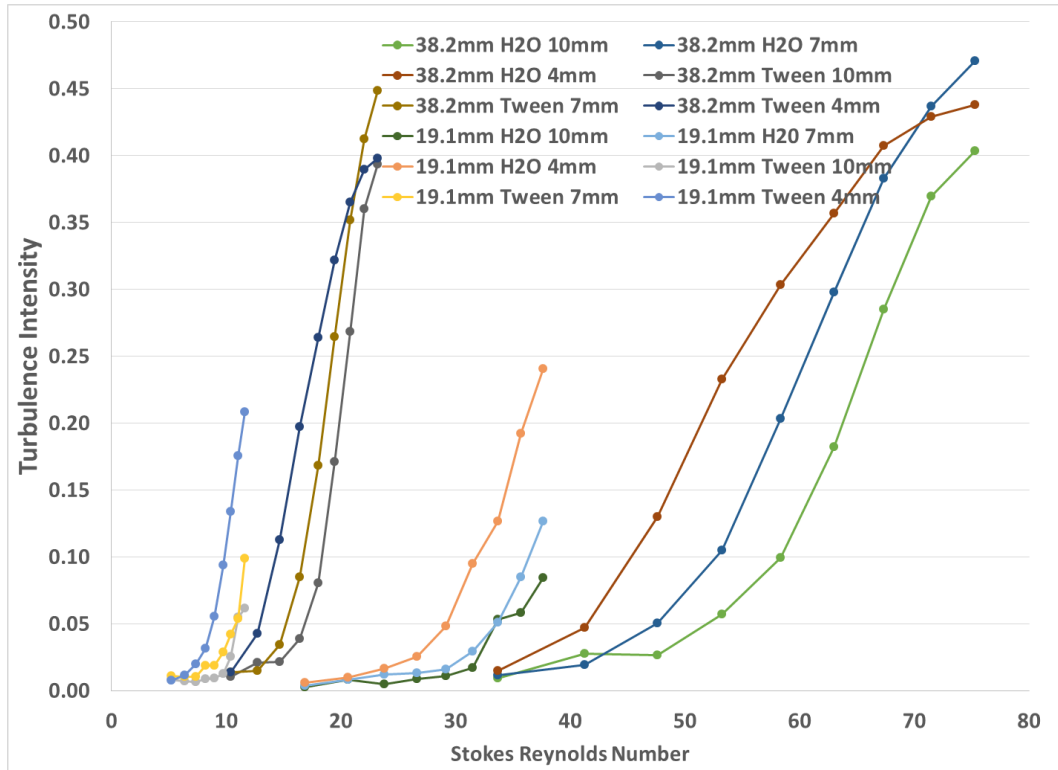
Figure 6.4. Turbulence intensity versus Stokes Reynolds number for 12 data sets.

Slope Ratio significantly affected the angle of the free surface of the wave in the dish. This parameter had not been previously studied for its effect on turbulence in an orbiting petri dish. Figure 6.5 show turbulence intensity versus Slope Ratio. While the plot indicates better correlation than Reynolds, Stokes, or Reynolds Stokes numbers, the correlation is not consistent across dish sizes. Intensities were higher for the data from the 38.1 mm dish data and a lower for the 19.1 mm dish. The Slope Ratio values ranged from about 0 to 2.25 for the larger dish, and the range for the smaller dish was about half that. The turbulence intensity values for the smaller dish were about half that of the larger dish. Asymptotic turbulence intensity values for water trended higher than those from tween by 11.4 %.
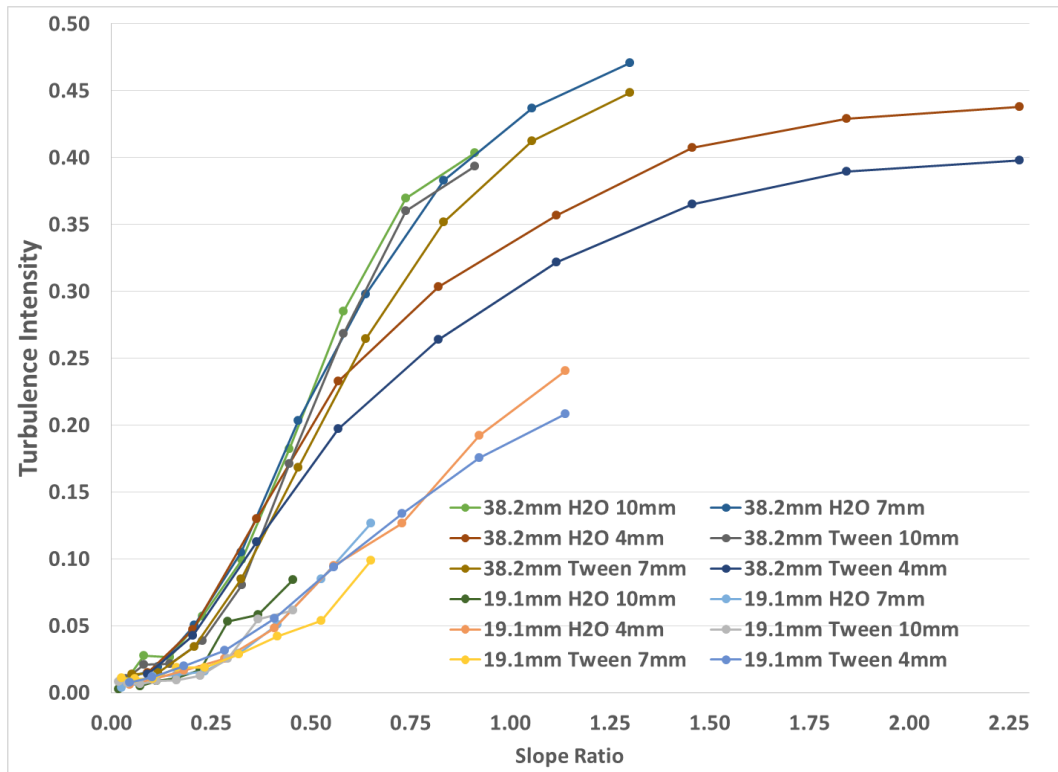
Figure 6.5. Turbulence intensity versus Slope Ratio for 12 data sets.

Weheliye *et al*. (2013), Rodriguez *et al*. (2013), and Ducci *et al*. (2014) showed the Froude number to affect turbulence more than the Reynolds number in orbiting dishes. Figure 6.6 shows turbulence intensity versus Froude number. The Froude number correlates with turbulence intensity best among the five dimensionless parameters examined. Froude numbers were investigated from 0.19 to 3.02. From 0.19 to ~ 1.4, the turbulence intensity values closely overlapped. The maximum variation was 18.9 % across the 12 data sets. Higher than a Froude number of 1.4, the intensities began to separate as turbulence became more fully developed. Froude numbers trended higher by 11.4 % for water than those from tween. Turbulence intensity values for taller resting fluid heights also trended higher. However, each of the curves were not fully developed to where they each flattened out after the asymptote to allow calculation of a percentage difference between turbulence intensity at differing resting fluid heights. This effect was not observed with any of the other dimensionless parameters.

87
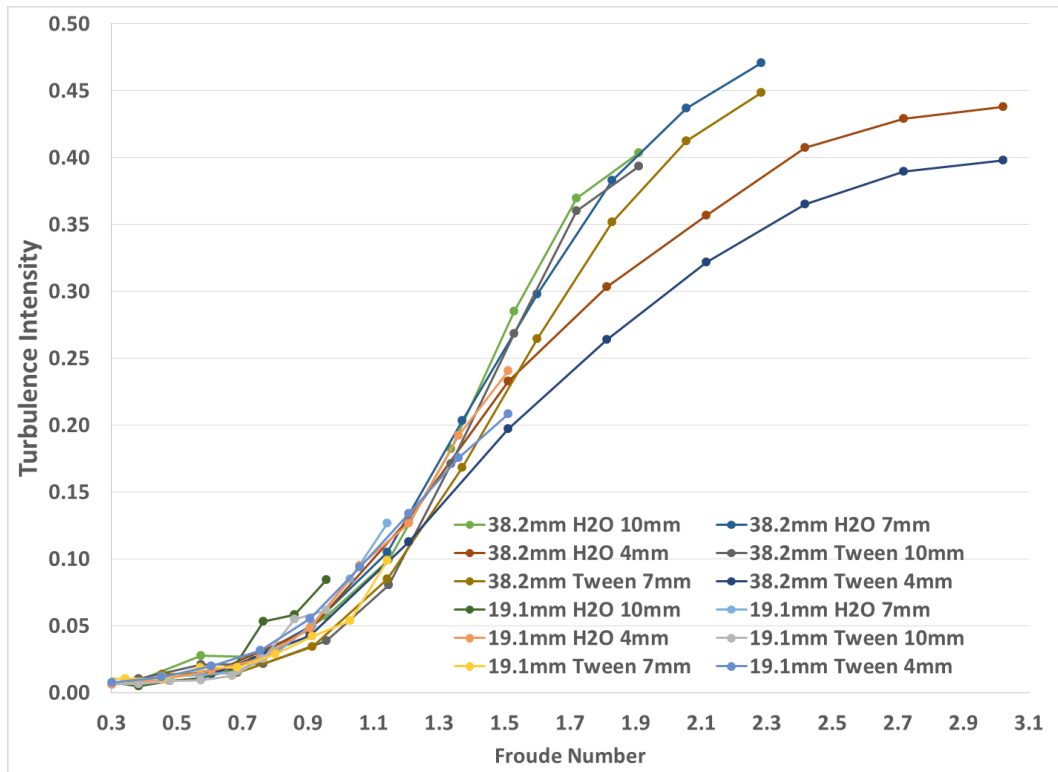
Figure 6.6. Turbulence intensity versus Froude number for 12 data sets.

6.3.2. Turbulence Transition

Froude number was shown to be the defining characteristic dimensionless parameter to determine transition to turbulence. As was detailed in section 6.2, the Froude number where flow ceased to be laminar is determined by locating where turbulence intensity values increase sharply. For laminar cases in Figure 6.1, the average turbulence intensity was consistently low and showed an oscillatory pattern. When entering the transition range the average turbulence intensity became greater and the oscillation became erratic.

Figure 6.7 focuses on the lower region of Froude numbers and adds a trend curve to better see the sharp increase indicating the turbulence transition. Turbulence intensity remained very low, near zero, and changed little with increases in Froude number from Froude numbers 0.19 to 0.69 indicating the region was laminar. Beginning at a Froude number of 0.76, the turbulence intensity increased rapidly with increases in Froude number, indicating the onset of turbulence.
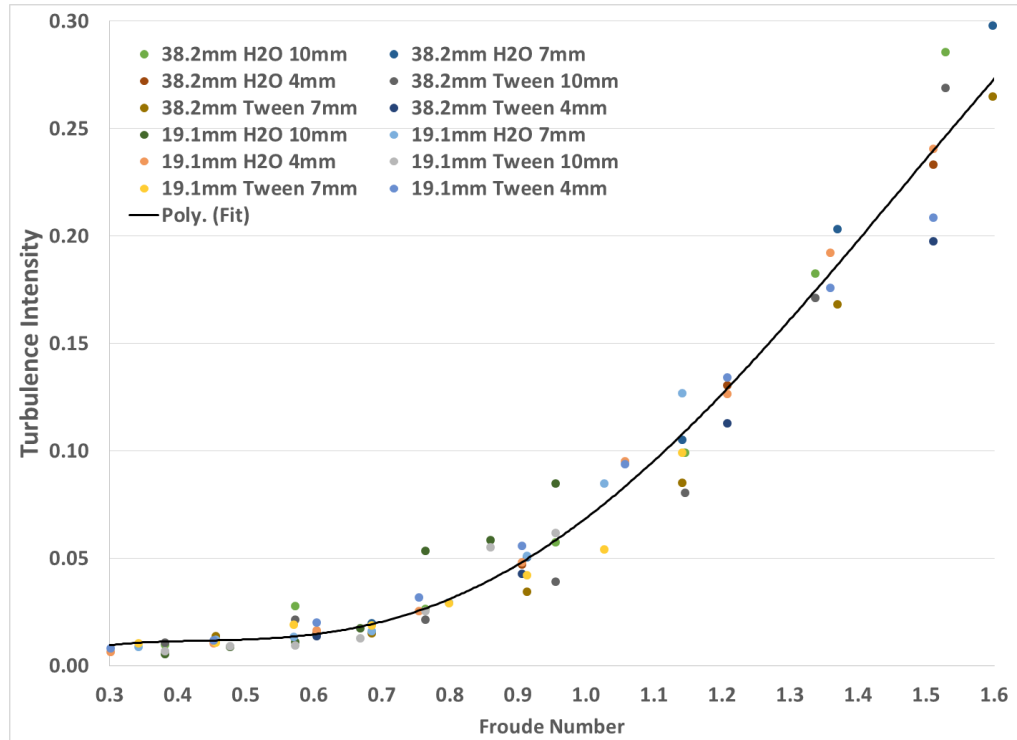
Figure 6.7. Turbulence intensity versus Froude number at transition for 12 data sets.

6.4. TRENDS ASSOCIATED WITH THE TURBULENCE TRANSITION

Contours of velocity magnitude were examined near the bottom of the dish for trends as a function of Froude number. There should be a visible change in the flow pattern as the flow transitions to turbulence and the corresponding Froude number increases. Velocity magnitude contours at 0.5 mm from the bottom of the dish were examined for each of the points in the twelve data sets investigated in tables 4.2-4.5.

Corresponding contours for water and the tween solution were similar for similar Froude numbers. Three distinct flow patterns were observed in these twelve data sets, agreeing with the findings from Gardner and Tatterson's (1992) dye tests on oscillatory flow in a dish. One occurred at low Froude numbers, another occurred at Froude numbers at and directly after the transition region begins, and the final at higher Froude numbers. Figure 6.8 shows a sample image for each of the three flow regimes. At low Froude numbers, there was a large oval-shaped high velocity area near the center, and the velocity decreases toward the

edges. At high Froude numbers, a high velocity crescent shaped region developed near the edge of the dish. At transitory Froude numbers, the high velocity region pushes toward the edge of the dish and forms a U shape.

(a) Low Fr = 0.47   (b) Transitory Fr = 0.76   (c) High Fr = 1.72
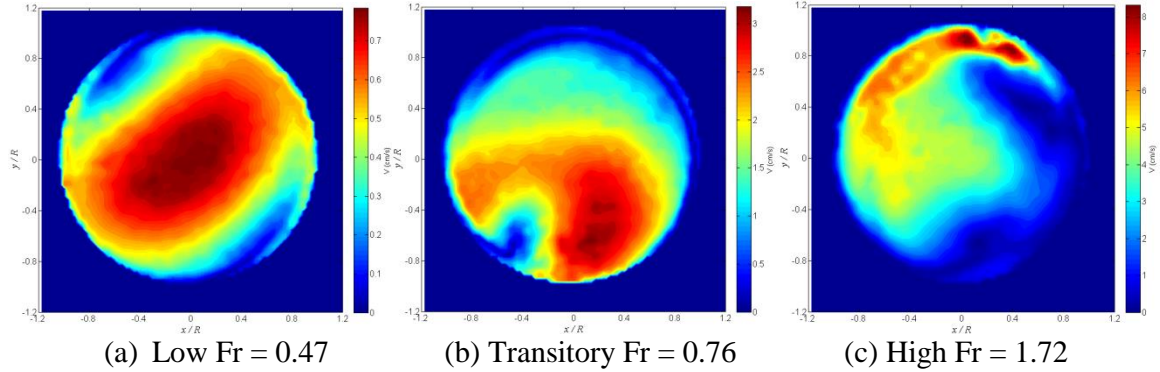
Figure 6.8. Three observed velocity magnitude profiles 0.5mm above the bottom of the dish.

6.5. COMPARISON WITH PREVIOUSLY PUBLIHSED DATA

6.5.1. Development of Parameters Used by Ducci et al. (2014)

A previous group published turbulence data for oscillatory flow in a dish, but used different dimensionless parameters and used dish sizes and fluid heights much larger than those used in these experiments. Ducci *et al.* (2014) examined what they referred to as turbulent kinetic velocities (TKV) for fluids with several viscosities and large dishes to attempt to define turbulence. Instead of the typically used turbulence intensity to approximate turbulence, they used the following expression for TKV:

$$TKV = \frac{\sqrt{\left(\langle u'^2\rangle + \langle v'^2\rangle\right)}}{\pi NR} \tag{78}$$

where N was the speed in revolutions per second and R was the orbital diameter. The TKV's were compared with a Froude number that differed from that used in this study. Their Froude number, defined in Equation 79, was based on orbital diameter instead of dish radius.

$$Fr = \frac{2\pi^2 N^2 R}{g} \tag{79}$$

While this definition of Froude number has been used in past literature, correlation of

velocity magnitudes by various normalization method for several Froude definitions showed that orbital diameter was a poor basis for describing the system, including as part of the Froude number. TKV values did not adequately line up with Equation (79), so they compared them with Froude number divided by critical Froude number as first described by Weheliye *et al*. (2013). Weheliye *et al*. (2013) empirically determined the critical Froude number as the point at which the fluid flow became out of phase and described it by two equations:

$$\frac{h}{a} = \left(\frac{h}{\Delta h}\right)_c Fr_c \cdot a_{ow} \tag{80}$$

$$\left(\frac{h}{\Delta h}\right)_c = \left(\frac{R}{a}\right)^{0.5} \tag{81}$$

where a_{ow} was determined to be 1.4. Ducci *et al*.'s (2014) TKV data showed strong agreement versus Fr/Fr$_c$, although this does not allow one to predict the turbulence transitions without first knowing F$_c$ for each particular case. The equation for Fr/Fr$_c$ was equated to dimensionless parameters used in this work:

$$Fr/Fr_c = \frac{Ra\omega^2}{gH} \cdot 0.7 \left(\frac{R}{a}\right)^{0.5} \tag{82}$$

Fr/Fr$_c$ is equivalent to the Slope Ratio multiplied by 0.7 times the square root of the orbital diameter divided by the dish diameter.

6.5.2. Comparison with Data from Ducci et al. (2014)

Ducci *et al*. (2014) published five sets of TKV data that varied the dish size, fluid viscosity, and fluid height to give the same Reynolds and Froude numbers for each matching case in subsequent tests at the same RPM. A notable difference between their experiments and those of this study was that they used the XZ plane was used to calculate TKV as they were studying vortex development in the Z plane and these experiments were performed in the XY plane.

Ducci *et al.*'s (2014) data were analyzed with the same process from this study to verify the development of turbulence transition with an independent group of flow conditions. Both collections of data (the new data here and Ducci *et al*'s (2014) data) were analyzed versus two parameters: Froude Number as used throughout this work (Figure 6.9) and Fr/Fr_c developed empirically by Weheliye *et al.* (2013) (Figure 6.10).

Both sets of data showed strong agreement of TKV values when plotted vs. Froude number in Figure 6.9. In the range of data from Ducci *et al.*'s (2014), there was an error in TKV values of 23.3%, only 4.3% greater than the error in Figure 6.6 without the additional data. Froude number, as defined here, does not contain a term for orbital radius, and when compared with data across varying orbital radii and at differing flow conditions it remained a strong predictor of turbulence transition.
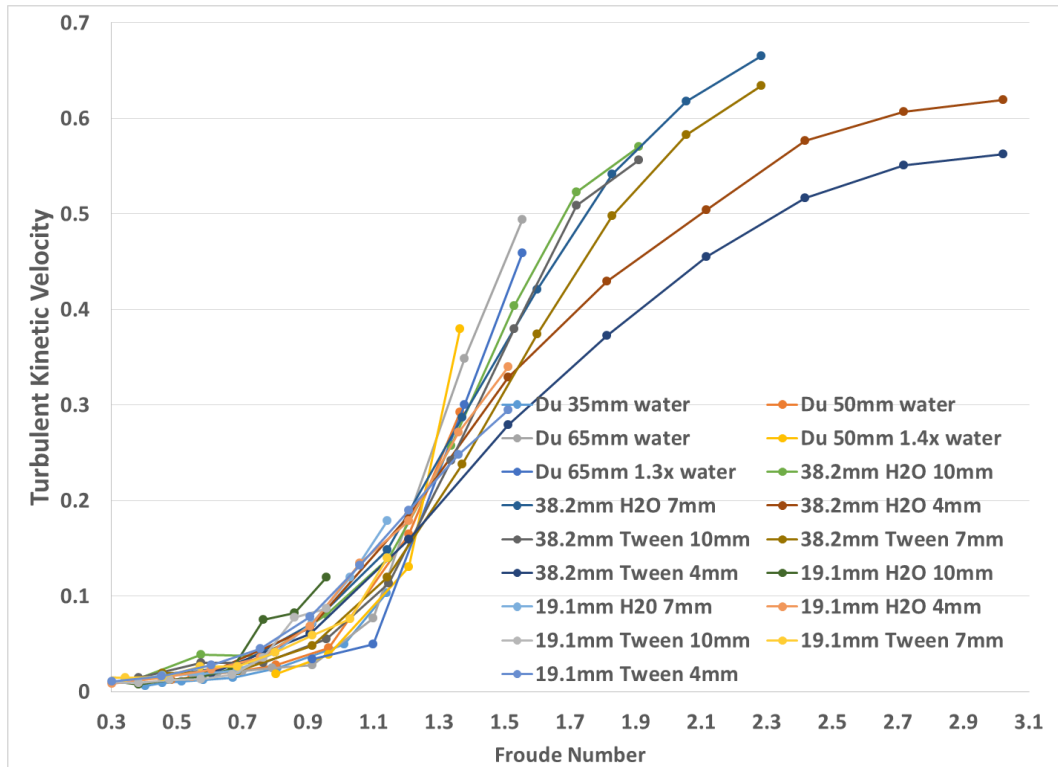
Figure 6.9. All data from Ducci *et al.* (2014) and this work plotted versus Froude number.

Figure 6.10 shows some agreement in TKV values, but not as strong as with the Froude number. In the lower range they agreed well, but there were three distinct groups of

data as the parameter value increased: one group for the 19.1 mm dish, one group for the 38.2 mm dish, and a third group for Ducci *et al.*'s (2014) data. The 19.1 mm and 38.2 mm dish have a similar break to the one observed against the Slope Ratio in Figure 6.5. As was noted in the derivation, Fr/Fr_c is equivalent to the Slope Ratio multiplied by a factor, which explains why dishes of different sizes deviate at different Fr/Fr_c values. Turbulence intensity values plotted versus Fr/Fr_c showed stronger agreement between 19.1 mm and 38.2 mm than when plotted versus Slope Ratio in Figure 6.5. Hence, the extra correlation in Fr/Fr_c, that was the square root of the ratio of diameters, served to improve the validity of the equation for turbulence assessment.
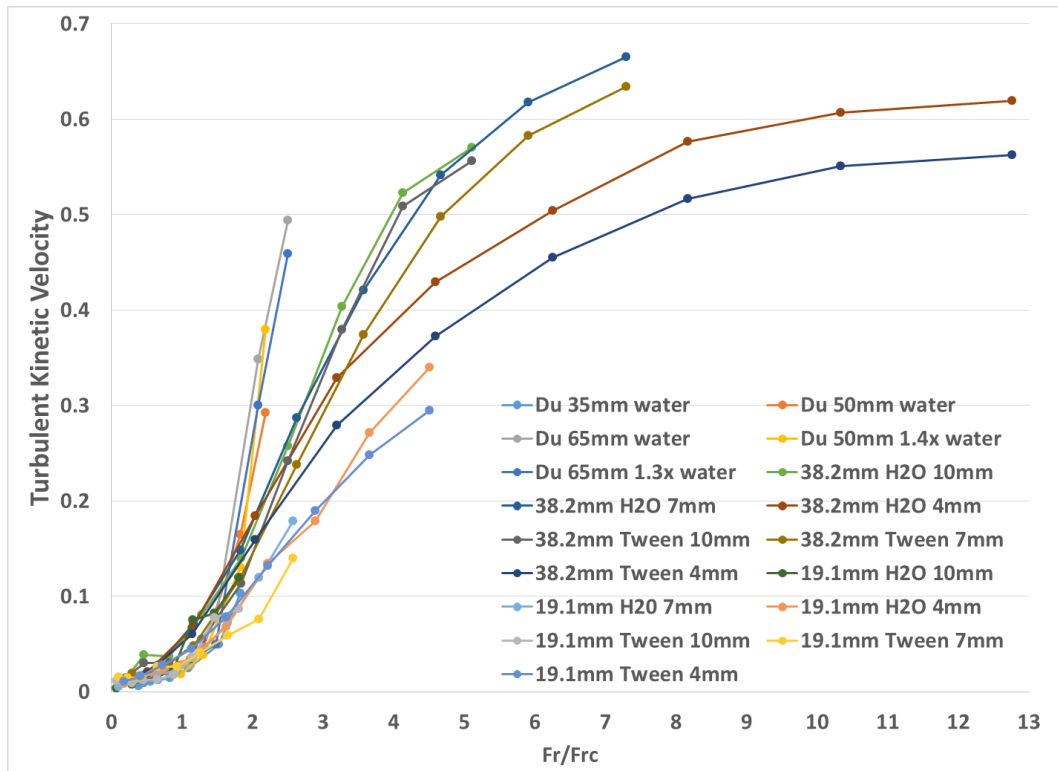
Figure 6.10. All data from Ducci *et al*. (2014) and this work plotted versus Fr/Fr_c.

CHAPTER VII

CONCLUSIONS

A computational model that simulates motion of fluid in a dish on an orbiting shaker apparatus has been developed. It provides a method for determining WSS on the bottom surface of the dish with complete spatial and temporal resolution. As a preliminary primitive validation, the CFD model was compared with WSS values from the literature generated from laser Doppler velocimetry and also with the analytical Stokes second problem solution. The model was reasonably well validated by both methods. The area average WSS magnitudes were 0.10 ± 1.02 dyne/cm^2 higher than the Stokes second problem solution over the full range of orbital speed. The experimental minimum and maximum WSS at 12 mm from the center of the dish were 6 and 16 dyne/cm2, respectively, whereas WSS generated from the computational model ranged from 0.5 to 14 dyne/cm^2. However since laser Doppler velocimetry is a single point measurement, a stronger validation was required.

To perform a more comprehensive validation, experimental PIV measurements and analytical values were compared to computationally derived fluid velocities in orbiting dishes. PIV provided an experimental view over a full slice inside of the dish, providing the most comprehensive validation for a wide variety of cases. Average computational normalized velocity magnitudes examined at a height 0.5 mm above the bottom varied from experimental PIV by an average of 0.3 % and from the analytical solution by 2.4 %. Velocity profiles along the vertical axis agreed well between CFD and the analytical solution. The dimensionless u-component velocities u/U for the six cases varied from the

analytical solution on average by -0.00046 ± 0.0015 and the v-component velocites v/U varied on average by 0.0038 ± 0.0084. Because the analytical solution neglects wall effects, and some amount of wall effects may be present even near the center of the dish, CFD and PIV results were in closer agreement than CFD and the analytical solution, although 2.4 % is still a very minor difference considering the complexity of the model. For the same reason, CFD and PIV results were also in closer agreement than PIV and the analytical solution. Validation of the computational model against both experimental data and analytical solutions provides confidence in the CFD solutions.

Turbulence intensities calculated from PIV were plotted versus several dimensionless parameters in attempt to define a transition to turbulence. Analysis shows the Froude number best described the transition to turbulence in the orbiting petri dish with the transition occurring between 0.69 and 0.86 and on average at 0.78. Three distinct velocity magnitude contour patterns were observed: an area of high velocity at the center at low Froude numbers, a high velocity crescent near the edge at high Froude numbers, and a transitional pattern between the two at and just above the transition in the shape of a 'U'. The Froude number based turbulent transition range held up to other published turbulent kinetic velocity data at operating parameters different from this study. The published data contained larger dishes, higher resting fluid heights, and varied the orbital radius. This expands the Froude numbers usefulness as a turbulence predictor over a wider range of parameters.

CHAPTER VIII

RECOMMENDATIONS

Throughout analysis, Reynolds number was expected to be the determining parameter for the onset of turbulence. This idea was shown to be in error as Froude number was shown to more closely indicate turbulence in an orbiting dish. The effect of Reynolds number still remains unknown since flows at substantially low Reynolds numbers have not been investigated. The flow in an orbiting dish could be considered similar to the swirling flow a mixing vessel, in which the Reynolds transition occurs near a value of 10. Future studies should investigate the effect of Reynolds numbers below this range. It is desirable to perform an analysis which varies Reynolds number while holding the Stokes number, Froude number, and slope ratio at constant values to see what, if any, effect the Reynolds number has on flow in an orbiting dish. It would be ideal to investigate Reynolds number in the range of 0.1 to 10,000. Upon finding the Reynolds transition, the free surface, WSS contours, and plot of WSS versus Reynolds number should be examined. Turbulence intensities can then be determined from PIV measurements to determine if/how Reynolds affects turbulence.

Each of three dimensionless parameters, the Stokes number, the Froude number, and the Slope Ratio, have known effect in the free surface shape as they transition from low to high. It is unknown precisely where each of the transitions will occur in relation to the effects of the other two parameters. Each of the three dimensionless parameters would need to be varied while keeping the other two parameters at two different sets of high or low values to find a transition for that parameter. To comprehensively define the effects of

varying the three dimensionless parameters relative to each other, each of the 27 cases would need to be examined. Having a great number of cases allows investigation of shear values and other phenomena throughout the range of the dimensionless parameter.

Due to limitations of the PIV system, it was not possible to experimentally determine the phase of the peak of the wave with respect to the phase of the orbit. The starting phase was unknown and subsequent captures may or may not share the same phase. For future experiments, it is desirable to add hardware to synchronize the PIV image capture with a specific location in orbit. This would make direct averaging between image pairs plausible and would possibly allow a view of secondary effects such as wave lag associated with high Stokes numbers and to determine if the phase of the wave varies between orbits.

PIV data was recorded with a single camera only allowing for a two dimensional analysis of flow. Ideally, WSS values would be generated directly from PIV. For WSS to be experimentally determined, a 3D-PIV set up utilizing two cameras in stereo would be required. 3D-PIV calculates Z velocities in addition to X and Y velocities. With three planes of data from 3D-PIV, the tensor could be completed to directly calculate WSS.

REFERENCES

1. McCabe WL, Smith JC, Harriott P. Unit Operations in Chemical engineering. New York: McGraw-Hill Book Co.; 1993.

2. Bird RB, Stewart WE, Lightfoot EN. Transport Phenomena: John Wiley & Sons, Inc; 2002.

3. Ohashi T, Sato M. Remodeling of vascular endothelial cells exposed to fluid shear stress: experimental and numerical approach. Fluid Dynamics Research. 2005:40-59.

4. Levesque MJ, Nerem RM. The elongation and orientation of cultured endothelial cells in response to shear stress. J Biomech Eng. 1985;107(4):341-7.

5. Kondapalli J, Flozak AS, Albuquerque ML. Laminar shear stress differentially modulates gene expression of p120 catenin, Kaiso transcription factor, and vascular endothelial cadherin in human coronary artery endothelial cells. J Biol Chem. 2004;279(12):11417-24.

6. McKinney VZ, Rinker KD, Truskey GA. Normal and shear stresses influence the spatial distribution of intracellular adhesion molecule-1 expression in human umbilical vein endothelial cells exposed to sudden expansion flow. J Biomech. 2006;39(5):806-17.

7. Partridge J, Carlsen H, Enesa K, Chaudhury H, Zakkar M, Luong L, et al. Laminar shear stress acts as a switch to regulate divergent functions of NF-kappaB in endothelial cells. FASEB J. 2007;21(13):3553-61.

8. Chotard-Ghodsnia R, Haddad O, Leyrat A, Drochon A, Verdier C, Duperray A. Morphological analysis of tumor cell/endothelial cell interactions under shear flow. J Biomech. 2007;40(2):335-44. PMCID: 1961634.

9. Sirois E, Charara J, Ruel J, Dussault JC, Gagnon P, Doillon CJ. Endothelial cells exposed to erythrocytes under shear stress: an in vitro study. Biomaterials. 1998;19(21):1925-34.

10. Sato M, Ohshima N, Nerem RM. Viscoelastic properties of cultured porcine aortic endothelial cells exposed to shear stress. J Biomech. 1996;29(4):461-7.

11. Sato M, Nagayama K, Kataoka N, Sasaki M, Hane K. Local mechanical properties measured by atomic force microscopy for cultured bovine endothelial cells exposed to shear stress. J Biomech. 2000;33(1):127-35.

12. Zhao F, Chella R, Ma T. Effects of shear stress on 3-D human mesenchymal stem cell construct development in a perfusion bioreactor system: Experiments and hydrodynamic modeling. Biotechnol Bioeng. 2007;96(3):584-95.

13. Papadaki M, McIntire LV, Eskin SG. Effects of shear stress on the growth kinetics of human aortic smooth muscle cells in vitro. Biotechnol Bioeng. 1996;50(5):555-61.

14. Nollert MU, Diamond SL, McIntire LV. Hydrodynamic shear stress and mass transport modulation of endothelial cell metabolism. Biotechnol Bioeng. 1991;38(6):588-602.

15. Sakamoto N, Ohashi T, Sato M. Effects of shear stress on permiability of vascular endothelial monolayer cocultured with smooth muscle cells. JSME International Journal. 2004;47(4):992-9.

16. Zeng Y, Qiao Y, Zhang Y, Liu X, Wang Y, Hu J. Effects of fluid shear stress on apoptosis of cultured human umbilical vein endothelial cells induced by LPS. Cell Biol Int. 2005;29(11):932-5.

17. Jin X, Iwasa S, Okada K, Ooi A, Mitsui K, Mitsumata M. Shear stress-induced collagen XII expression is associated with atherogenesis. Biochem Biophys Res Commun. 2003;308(1):152-8.

18. Kudo SY, R. Machida, K. Ikeda, M. Oka, K. Tanishita, K. Effects of long term shear stress exposure on calcium response and morphology of cultured endothelial cells. JSME International Journal. 2003;46(4):1226-33.

19. Fukushima A, Nagatsu A, Kaibara M, Oka K, Tanishita K. Measurement of surface topography of endothelial cell and wall shear stress distribution on the cell. JSME International Journal. 2001;44(4):972-81.

20. Nagayama K, Fujii M, Kudou S, Tanishita K. Behavior of individual endothelial cell under shear stress. Bioengineering Conference1995. p. 515-6.

21. Dewey CF, Jr. Effects of fluid flow on living vascular cells. J Biomech Eng. 1984;106(1):31-5.

22. Hermann C, Zeiher AM, Dimmeler S. Shear stress inhibits H2O2-induced apoptosis of human endothelial cells by modulation of the glutathione redox cycle and nitric oxide synthase. Arterioscler Thromb Vasc Biol. 1997;17(12):3588-92.

23. Feugier P, Black RA, Hunt JA, How TV. Attachment, morphology and adherence of human endothelial cells to vascular prosthesis materials under the action of shear stress. Biomaterials. 2005;26(13):1457-66.

24. Ley K, Lundgren E, Berger E, Arfors KE. Shear-dependent inhibition of granulocyte adhesion to cultured endothelium by dextran sulfate. Blood. 1989;73(5):1324-30.

25. Owatverot TB, Oswald SJ, Chen Y, Wille JJ, Yin FC. Effect of combined cyclic stretch and fluid shear stress on endothelial cell morphological responses. J Biomech Eng. 2005;127(3):374-82.

26. Langerquist KA, Suvatne J, Barakat AI, editors. Multi-directional floe chamber: Analysis of endothelial cell morphology dependence on different shear forces. Proceedings of the second joint EMBS/BMES conference; 2002; Houston, TX, USA.

27. Hsiai TK, Cho SK, Wong PK, Ing M, Navab M, Reddy S, et al., editors. BioMEMS sensors for real time shear stress on endothelial cell dynamics. Proceedings of the second joint EMBS/BMES conference; 2002.

28. Haritonnidis JH. The measurement of shear stress Advances in fluid mechanics measurements: Springer-Verlag; 1989. p. 229-36.

29. Chiu JJ, Chen LJ, Chen CN, Lee PL, Lee CI. A model for studying the effect of shear stress on interactions between vascular endothelial cells and smooth muscle cells. J Biomech. 2004;37(4):531-9.

30. Inoguchi H, Tanaka T, Maehara Y, Matsuda T. The effect of gradually graded shear stress on the morphological integrity of a huvec-seeded compliant small-diameter vascular graft. Biomaterials. 2007;28(3):486-95.

31. Saarinen MA, Murhammer DW. Culture in the rotating-wall vessel affects recombinant protein production capability of two insect cell lines in different manners. In Vitro Cell Dev Biol Anim. 2000 Jun;36(6):362-6.

32. Elias CB, Desai RB, Patole MS, Joshi JB, Mashelkar R. Turbulent Shear Stress — Effect on Mammalian Cell Culture and Measurement Using Laser Doppler Anemometer. Chemical Engineering Science. 1995:50(15):2431-2440.

33. Berson RE, Purcell MR, Sharp MK, editors. Fluid motion in an orbiting culture dish. World Cong Biomech; 2006 July 30 - Aug 4; Munich, Germany.

34. Yun S, Dardik A, Haga M, Yamashita A, Yamaguchi S, Koh Y, et al. Transcription factor Sp1 phosphorylation induced by shear stress inhibits membrane type 1-matrix metalloproteinase expression in endothelium. J Biol Chem. 2002;277(38):34808-14.

35. Pearce MJ, McIntyre TM, Prescott SM, Zimmerman GA, Whatley RE. Shear stress activates cytosolic phospholipase A2 (cPLA2) and MAP kinase in human endothelial cells. Biochem Biophys Res Commun. 1996;218(2):500-4.

36. Kraiss LW, Weyrich AS, Alto NM, Dixon DA, Ennis TM, Modur V, et al. Fluid flow activates a regulator of translation, p70/p85 S6 kinase, in human endothelial cells. Am J Physiol Heart Circ Physiol. 2000;278(5):H1537-44.

37. Haga M, Yamashita A, Paszkowiak J, Sumpio BE, Dardik A. Oscillatory shear stress increases smooth muscle cell proliferation and Akt phosphorylation. J Vasc Surg. 2003;37(6):1277-84.

38. Dardik A, Chen L, Frattini J, Asada H, Aziz F, Kudo FA, et al. Differential effects of orbital and laminar shear stress on endothelial cells. J Vasc Surg. 2005;41(5):869-80.

39. Anderson JDJ. Computational Fluid Dynamics - A Engineering Tool ? Numerical laboratory computational methods in Fluid Dynamics, ASME. 1976:1-12.

40. Chung TJ. Computational Fluid Dynamics. Cambridge, United Kingdom: Cambridge University Press; 2002.

41. Graves RA. Computational Fluid Dynamics - The coming revolution. Astronautics and Aeronautics. 1982;20(3):20-8.

42. Kopal Z. Tables of supersonic flow around cones. Cambridge: Massachusetts Institute of technology; 1947.

43. Taylor GI, Maccoll JW, editors. The air pressure on a cone moving at high speed. Proceedings of the Royal Society (A); 1933.

44. Fay JA, Riddell FR. Theory of stagnation point heat transfer in dissotiated air Journal of Aeronautical Science. 1958;25(2):73-85.

45. Blottner FG. Chemical nonequilibrium boundary layer. AIAA. 1964;2(2):232-9.

46. Blottner FG. Nonequilibrium laminar boundary layer flow of ionized air. AIAA. 1964;2(11):1921-7.

47. Hall HG, Eschenroeder AQ, Marrone PV. Blunt-nose inviscid airflows with coupled nonequilibrium processes. Journal of the aerospace science. 1962;19(9):1038-51.

48. Anderson JD, Dick E, Degrez G, Grundmann R, Degroote J, Vierendeels J. Computational Fluid Dynamics - an Introduction. 3rd ed. Wendt PDJF, editor: Springer; 2009.

49. ANSYS I. FLUENT 6.2.5. Canonsburg, PA2006.

50. FLUENT I. FLUENT user guide. Lebanon, NH2007.

51. Tu J, Yeoh GH, Liu C. Computational Fluid Dynamics: A computational approach. 1st ed. Burlington, MA: Elsevier; 2008.

52. Bhaskaran R, Collins L. Introduction to CFD basics: Cornell University; 2002.

53. Gerber S, Oevermann M, Behrendt F, editors. An Euler-Lagrange modeling approach for the simulation of wood gasification in fluidized beds. Proceedings of European combustion meeting; 2009.

54. Sakurai A NA, Yamaguchi T, Masuda M, Fujiwara K. A computational fluid mechanical study of flow over cultured endothelial cells. Advances in Bioengineering. 1991;20:289-302.

55. Satcher RL, Jr., Bussolari SR, Gimbrone MA, Jr., Dewey CF, Jr. The distribution of fluid forces on model arterial endothelium using computational fluid dynamics. J Biomech Eng. 1992;114(3):309-16.

56. Yamaguchi T, Hanai S. Measured wall shear stress distribution pattern upstream and downstream of a unilateral stenosis by an electrochemical method. Biorheology. 1987;24(6):753-62.

57. Weston SJ, Wood NB, Tabor G, Gosman AD, Firmin DN. Combined MRI and CFD analysis of fully developed steady and pulsatile laminar flow through a bend. J Magn Reson Imaging. 1998;8(5):1158-71.

58. Yamaguchi T, Yamamoto Y, Liu H. Computational mechanical model studies on the spontaneous emergent morphogenesis of the cultured endothelial cells. J Biomech. 2000;33(1):115-26.

59. Banerjee RK, Back LH, Back MR, Cho YI. Physiological flow simulation in residual human stenoses after coronary angioplasty. J Biomech Eng. 2000;122(4):310-20.

60. Berthier B, Bouzerar R, Legallais C. Blood flow patterns in an anatomically realistic coronary vessel: influence of three different reconstruction methods. J Biomech. 2002;35(10):1347-56.

61. Papathanasopoulou P, Zhao S, Kohler U, Robertson MB, Long Q, Hoskins P, et al. MRI measurement of time-resolved wall shear stress vectors in a carotid bifurcation model, and comparison with CFD predictions. J Magn Reson Imaging. 2003;17(2):153-62.

62. Fukushima SG, H. Tanishita, K. . Shear stress distribution on the surface endothelial cells during flow-induced morphological remodeling. JSME International Journal. 2003;46(4):1275-83.

63. Marshall I, Zhao S, Papathanasopoulou P, Hoskins P, Xu Y. MRI and CFD studies of pulsatile flow in healthy and stenosed carotid bifurcation models. J Biomech. 2004;37(5):679-87.

64. Buschmann MH, Dieterich P, Adams NA, Schnittler HJ. Analysis of flow in a cone-and-plate apparatus with respect to spatial and temporal effects on endothelial cells. Biotechnol Bioeng. 2005;89(5):493-502.

65. Van Tricht I, De Wachter D, Tordoir J, Verdonck P. Comparison of the hemodynamics in 6mm and 4-7 mm hemodialysis grafts by means of CFD. J Biomech. 2006;39(2):226-36.

66. Morbiducci U, Ponzini R, Grigioni M, Redaelli A. Helical flow as fluid dynamic signature for atherogenesis risk in aortocoronary bypass. A numeric study. J Biomech. 2007;40(3):519-34.

67. Smith S, Austin S, Wesson GD, Moore CA. Calculation of wall shear stress in left coronary artery bifurcation for pulsatile flow using two-dimensional computational fluid dynamics. Conf Proc IEEE Eng Med Biol Soc. 2006;1:871-4.

68. Brown A, Meenam B, editors. Investigating the effects of fluid shear forces on cellular responses to profiled surfaces in-vitro: A computational and experimental investigation 2007; Lyon, France.

69. Jung J, Hassanein A. Three-phase CFD analytical modeling of blood flow. Med Eng Phys. 2008;30(1):91-103.

70. Tokuda Y, Song MH, Ueda Y, Usui A, Akita T, Yoneyama S, et al. Threedimensional numerical simulation of blood flow in the aortic arch during cardiopulmonary bypass. Eur J Cardiothorac Surg. 2008;33(2):164-7.

71. Dong X, Wang K. Prediction and simulation on the shear stress and mass transfer in perfused bioreactor I : Circular bioreactor. Chinese Control and Decision Conference. 2008. p. 4237 - 42.

72. Dehlaghi V, Shadpoor MT, Najarian S. Analysis of wall shear stress in stented coronary artery using 3D computational fluid dynamics modeling. Journal of Materials Processing Technology. 2008;I97:I74-I81.

73. Nanduri JR, F.A. P-R, Celik I. CFD mesh generation for biological flows: Geometry reconstruction using disgnostic images. Computers & Fluids. 2009:38:1026-32.

74. Berson RE, Purcell, MR, and Sharp MK. Computationally Determined Shear on Cells Grown in Orbiting Culture Dishes. Advances in Experimental Medicine and Biology. 2008;614:189-198.

75. Zhang X, Bürki CA, Stettler M, Sanctis DD, Perrone M, Disacciati M, Parolini N, DeJesus M, Hacker DL, Quarteroni A, Wurm FM. Efficient oxygen transfer by surface aeration in shaken cylindrical containers for mammalian cell cultivation at volumetric scales up to 1000 L. Biochemical Engineering Journal. 2009:45:41-47.

76. Sargent CY, Berguig GY, Kinney MA, Hiatt LA, Carpenedo RL, Berson BE, McDevitt TC. Hydrodynamic modulation of embryonic stem cell differentiation by rotary orbital suspension culture. Biotechnology and Bioengineering, 2010;105(3), 611-626.

77. Warboys CM, Berson RE, Mann GE, Pearson JD, and Weinberg PD: Acute and chronic exposure to shear stress have opposite effects on endothelial permeability to macromolecules, American Journal of Physiology - Heart and Circulatory Physiology. 2010;298(6), H1850-H1856.

78. Thomas JMD, Chakraborty A, Sharp MK, Berson RE. Spatial and temporal resolution of shear in an orbiting petri dish. Biotechnology Progress. 2011;27:460-465.

79. Potter CM, Lundberg MH, Harrington LS, Warboys CM, Warner TD, Berson RE, Moshkov AV, Gorelik J, Weinberg PD, Mitchell JA. Role of Shear Stress in Endothelial Cell Morphology and Expression of Cyclooxygenase Isoforms. Arterioscler Thromb Vasc Biol., 2011;31(2), 384-391.

80. Chakraborty A, Chakraborty S, Thomas JMDT, Jala V, Bodduluri H, Sharp MK, Berson RE. Effects of Biaxial Oscillatory Shear Stress on Endothelial Cell Proliferation and Morphology. Biotechnol Bioeng. 2012;109:3:695-707.

81. Rotta J. Die Aerodynamische Versuchsant in Göttingen, ein Werk, Ludwig Prandtls. Vandenhoek & Ruprecht, Göttingen. 1990.

82. Foreman JW, George EW, Lewis RD. Measurement of Localized Flow Velocities in Gases with a Laser Doppler Flowmeter. Applied Physics Letters. 1965:7(4):77.

83. Grant I. Selected papers on particle image velocemitry SPIE Milestone Series MS99. SPIE Optical Engineering Press, Bellingham, Washington. 1994.

84. Raffel M, Willert C, Kompenhans J. Particle image velocimetry a practical guide. Springer-Verlag, Berlin Heidelberg, 1998.

85. van de Hulst HC. Light Scattering in Small Particles. John Wiley & Sons, Inc., New York. 1957.

86. Hecht E, Zajac A. Optics. Addison-Wesley Pub. Company, Massachussets. 1974.

87. Adrian RJ. Statistical properties of particle image velocimetry measurements in turbulent flow. Laser Anemometry in Fluid Mechanics III. Springer-Verlag, Berlin Heidelberg, 1988.

88. Keane RD and Adrian RJ. Theory of cross-correlation analysis of PIV images. Appl. Sci. Res. 1992:49:191-215.

89. Westerweel J. Digital particle image velocemitry – theory and application. Ph.D. dissertation. Delft University Press, Delft. 1993.

90. Papoulis A. Probability, Random Variables and Stochastic Processes. McGraw Hill, New York. 1991.

91. Kim HM and Kizito JP. Stirring Free Surface Flows Due to Horizontal Circulatory Oscillation of a Partially Filled Container. Chem. Eng. Comm. 2009:196:1300–1321.

92. Salek MM, Sattari P, Martinuzzi RJ. Analysis of Fluid Flow and Wall Shear Stress Patterns Inside Partially Filled Agitated Culture Well Plates. Annals of Biomedical Engineering. 2011;40(3):707-728.

93. Weheliye W, Yianneskis M, Ducci A. On the Fluid Dynamics of Shaken Bioreactors—Flow Characterization and Transition. AIChE Journal. 2013;59(1):334-344.

94. Rodriguez G, Weheliye W, Anderlei T, Micheletti M, Yianneskis M, Ducci A. Mixing time and kinetic energy measurements in a shaken cylindrical bioreactor. Chemical Engineering Research and design. 2013:91:2084-2097.

95. Reclari M, Dreyer M, Tissot S, Obreschkow D. Wurm FM, Farhat M. Surface wave dynamics in orbital shaken cylindrical containers. Physics of Fluids. 2014:26: 052104-1-11.

96. Klöckner W, Tissot S, Wurm F and Büchs J. Power input correlation to characterize the hydrodynamics of cylindrical orbitally shaken bioreactors. Biochemical Engineering Journal. 2012:65:63-69.

97. Thomas JMD, Chakraborty A, Berson RE, Shakeri M, Sharp MK. Validation of a CFD model of Orbiting Culture Dish with PIV and Analytical Solutions. AIChE Journal. 2016

98. Hino M, Sawamoto M, Takasu S. Experiments on Transition to Turbulence in an Oscillatory Pipe-Flow. Journal of Fluid Mechanics. 1975; 75:193-207.

99. Akhavan R, Kamm RD, Shapiro AH. An investigation of transition to turbulence on bounded oscillatory flow .1. experiments. Journal of Fluid Mechanics. 1991:25:395-422.

100. Akhavan R, Kamm RD, Shapiro AH. An investigation of transition to turbulence on bounded oscillatory flow .2. numerical simulations. Journal of Fluid Mechanics. 1991:25:395-422.

101. Eckman DM, Grothberg JB. Experiments on transition to turbulence in oscillatory pipe flow. Journal of Fluid Mechanics. 1991:222:329-350.

102. Zhao TS and Cheng P. Experimental Studies on the onset of turbulence and frictional losses in an oscillatory turbulent pipe flow. Journal of Heat and Fluid Flow. 1996:17:356-362.

103. Vittori G and Verzicco R. Direct simulation in an oscillatory boundary layer. Journal of Fluid Mechanics. 1998:371:207-232.

104. Sherwin JS and Blackburn HM. Three-dimensional instabilities and transition of steady and pulsatile axisymmetric stenotic flows. Journal of Fluid Mechanics. 2005:533:297-327.

105. Trip R, Kuik DJ, Westerweel J, Poelma C. An experimental study of transitional pulsatile pipe flow. Physics of Fluids. 2012:24:014103.

106. Gardner J and Tatterson G. Characteristics of Mixing in shaker table containers. Biotechnology and Bioengineering. 1992:39:794-797.

107. Ducci A, Weheliye W. Orbitally Shaken Bioreactors—Viscosity Effects on Flow Characteristics. AIChE Journal. 2014:60(11):3951.

108. Berson RE, Purcell MR, Sharp MK, "Fluid motion in an orbiting culture dish," World Congress of Biomechanics, Munich, Germany, Jul 30 – Aug 4, 2006.

109. Thomas JMD. Fluid Dynamics Analysis of Oscillating Flow in a Petri Dish. Master's Thesis. University of Louisville. 2007.

110. Chakraborty A. Fluid Dynamic Analysus of Flow in Orbiting Dishes and the Effects of Flow on Shear Stress and Endothelial cellular Responses. PHD Dissertation. University of Louisville. 2011.

111. Rance, P. and Warren, N. 1968. The inception movement of course material is oscillatory flow. Proceedings of the 11th Conference in Costal Engineering. 487-491.

112. You, Z. 1999. The inception of sheet flow in oscillatory flow. Ocean Engineering. 26:227-285.

113. Wilson, David B. 1987. Kelvin and Stokes A Comparative Study in Victorian Physics.

114. Hinds, W. 1998. Aerosol Technology: Properties, Behavior and Measurement of Airborne Particles, Second Edition. New York: John Wiley & Sons, Inc.

115. Brown, D. and Lambert, A. 2004. Oxford Dictionary of National Biography. Oxford: Oxford University Press.

116. Finney, R., Weir, M., Giordano, F. 2003. Thomas's Calculus Updated Tenth Edition. Boston:Addison Wesley. 2.

APPENDIX

A. <u>Nomenclature</u>

a	=	cylinder radius
A_S	=	surface area
d_c	=	characteristic dimension
f	=	frequency of rotation
F_S	=	shear force
g	=	gravitational acceleration
H	=	mean fluid height
h	=	enthalpy
I	=	turbulence intensity
m	=	mass
R	=	orbital radius
Re	=	Reynolds number
Si	=	entropy
S_m	=	source term for the addition of mass
U	=	velocity
u	=	x-velocity
v	=	y-velocity
y	=	height
ρ	=	fluid density
τ	=	shear stress
τ_ω	=	maximum wall shear stress
TKV	=	turbulent kinetic velocity
μ	=	fluid viscosity
ν	=	kinematic viscosity
ω	=	angular velocity

B. <u>Algorithm for Determining Projected Intervals</u>

A test was performed on a cylinder with a radius of 1.75 cm and a height of 0.8 cm in

FLUENT to find optimum projected intervals. The results showed that 50 projected intervals

resulted in 297050 cells and produced the best combination of fast convergence and accurate

results. This base case is used to scale the ideal projected interval to any case. An iterative

method is used to find the projected interval at a given set of cylinder dimensions. First, the

number of cells on the face is calculated by multiplying the number of cells on the face of the base case (5941) by the radius of the new cylinder, dividing by the radius of the base case, and finally multiplying by a scale factor. The scale factor is an arbitrary value that is used for iteration. Next, the number of projected intervals is calculated by multiplying the number of projected intervals in the base case by the height of the new cylinder, dividing by the height of the base case and multiplying by the arbitrary scale factor. The number of cells in the cylinder is then calculated by multiplying the number of cells in the face by the number of projected intervals. The correct number of projected intervals for the cylinder is determined by varying the scale factor until the number of cells reach 300,000.

C. Example User Defined Function

To insert motion into a case in FLUENT, a C language based program is used. For the orbital dish system of study, the code seen in Figure 108 is used to add oscillatory motion to the cylinder. The real radius in line six corresponds to the orbital radius, while w in line seven is the orbital speed.

```
#include "udf.h"
DEFINE_CG_MOTION(rotor_motion, dt, cg_vel, cg_omega, time, dtime)
{
real w,angle;
real offset = 0.;
real radius = 0.012;
w = 28.5774;
NV_S (cg_omega, =, 0.0);
NV_S (cg_vel, =, 0.0);
angle = w*time + offset;
cg_vel[0] = -radius * w * sin(angle);
cg_vel[1] = radius * w * cos(angle);
        }
```

D. Example Batch File

A batch file is used is need to run a case on a node of Adelie. The batch file opens FLUENT, tells the server what nodes to run on, and sets the location of the inputfile and the

outputfile. Line three tells the number of nodes to use, line five sends an e-mail upon case

completion, and line eight tells FLUENT to open the 3D version.

```
#!/bin/bash
#PBS -q dualcore2
#PBS -l nodes=1:ppn=1
#PBS -m e
#PBS -M jmthom27@louisville.edu
INPUT_FILE=/scr/JMDT/thesis/stokes/stokes10/inputfile_uss
OUTPUT_FILE=/scr/JMDT/thesis/stokes/stokes10/outputfile
DIM=3d
PROG="/apps/Fluent.Inc/bin/fluent "
PROGARGS="$DIM -g -i $INPUT_FILE"
echo Running on:
cat $PBS_NODEFILE
NPROCS=`wc -l < $PBS_NODEFILE`
echo This job uses $NPROCS processors
hostname
$PROG $PROGARGS > $OUTPUT_FILE 2>&1
```

E. Example Input File

The input file tells FLUENT where to open the case and data files, how to solve the

case, and where to write the results. Lines one and two tell FLUENT where to read the initial

case and data file. Line five tells FLUENT the number of time steps. Line six gives the

maximum number of iteration per time step. Lines seven and eight tell FLUENT where to

write the results once iterations are complete.

```
rc /scr/JMDT/thesis/stokes/stokes10/10stokes5.cas
rd /scr/JMDT/thesis/stokes/stokes10/10stokes5.dat
solve
d
859
50
wc /scr/JMDT/thesis/stokes/stokes10/10stokes0864.cas
wd /scr/JMDT/thesis/stokes/stokes10/10stokes0864.dat
quit
exit
yes
```

F. <u>MATLAB Code to Generate Radial-Tangential Plot</u>

```
clear all; close all; clc; %format short;

h = 0.15;
R = 0.3; % mm

filer = 'D:\dissertation!!!\fluent_pics\froude_hshs\froude_0.050hshs_right.txt';
fidr = fopen(filer,'r');
nrpm = strfind(filer,'rpm');

tline = fgetl(fidr);
data = (fscanf(fidr,'%g %g',[7,inf])).'; fclose(fidr);
x = -data(:,2)*1e3/R; y = data(:,3)*1e3/R; %z = data(:,4)*1e3;
wss = data(:,5); xwss = data(:,6); ywss = data(:,7); %ZWSS = data(:,8);

xmin = min(x); xmax = max(x);
ymin = min(y); ymax = max(y);

x = x+(abs(xmin)-abs(xmax))/2;
y = y+(abs(ymin)-abs(ymax))/2;

xmin = min(x); xmax = max(x);
ymin = min(y); ymax = max(y);

wssmin = min(wss);
wssmax = max(wss);
wssmin = mean(wss);

WSS = TriScatteredInterp(x,y,wss);
XWSS = TriScatteredInterp(x,y,xwss);
YWSS = TriScatteredInterp(x,y,ywss);

dx = (xmax-xmin)/100;
dy = (ymax-ymin)/100;
[xi,yi] = meshgrid(xmin:dx:xmax,ymin:dy:ymax);

indout = find(sqrt(xi.^2+yi.^2) >= 1);

WSSi = WSS(xi,yi);
XWSSi = XWSS(xi,yi);
YWSSi = YWSS (xi,yi);

WSSi(indout) = 0;
XWSSi(indout) = 0;
YWSSi(indout) = 0;

WSSi(isnan(WSSi)) = 0;
XWSSi(isnan(XWSSi)) = 0;
```

```
YWSSi(isnan(YWSSi)) = 0;

figure(1),
contourf(xi,yi,WSSi,50,'LineColor','None'); hold on;
colormap jet;
xlabel('\it x / R','FontName','Times','FontSize',14); ylabel('\it y /
R','FontName','Times','FontSize',14);
axis square;
axis([xmin,xmax,ymin,ymax])
set(gca,'FontSize',12);
set(gca,'XTick',-1.0:0.5:1.0);
set(gca,'YTick',-1.0:0.5:1.0);
hc = colorbar;
ylabel(hc,'WSS (Pa)')

theta = 0:2*pi/99:2*pi;
j=0;
for rho = [0.2:0.2:0.8],
    j = j + 1;
    [Xr,Yr] = pol2cart(theta,rho);

    WSSr = WSS(Xr,Yr);
    XWSSr = XWSS(Xr,Yr);
    YWSSr = YWSS(Xr,Yr);

    XWSS_mat(j,:)= XWSSr;
    YWSS_mat(j,:)= YWSSr;

    figure(1),
    plot(Xr,Yr,'-k'); hold on;

    figure(2),
    %plot(theta,WSSr,'-k'); hold on;
    plot(XWSSr,YWSSr,'-k'); hold on;
    xlabel('X WSS (dyne/cm2)','FontName','Times','FontSize',14);
    ylabel('Y WSS (dyne/cm2)','FontName','Times','FontSize',14);
    %axis([0,2*pi,0.95*min(WSSr(:)),1.05*max(WSSr(:))])
    set(gca,'FontSize',12);
end
axis square;

filew = strcat(filer(1:end-4),'_YWSS-elipall','.xlsx');
xlswrite(filew,[XWSS_mat,YWSS_mat]')
```

G. <u>MATLAB Code to Generate Velocity Magnitude from PIV</u>

```
clear all; close all; clc;
scrsz = get(0,'ScreenSize');

respiv = (38.1*2)/1694;
xc = (170+round(1694/2))*respiv;
yc = (2048-(200+round(1694/2)))*respiv;
R = 1694/2*respiv;

direct =
uigetdir('D:\PIV_stuff\tween\PIVfiles\cellshear6_vis11cp_fh10mm_rpm150_ls0p5mm_dt020
00us','Select .vec files');

directory = strcat(direct,'\*');

if(~strcmp(directory,'\*'))
    [stat,mess] = fileattrib(directory);
end

datfiles = [];
for i=1:size(mess,2)
    filename = mess(i).Name;
    if(strcmp(filename(end-3:end),'.vec'))
        datfiles = [datfiles; i];
    end;
end;
nf = size(datfiles,1);

np = 4;

j = 0;
VelMax = []; VelMean = [];
for i = 1:nf,
    j = j + 1    ;
    filepiv = mess(datfiles(i)).Name;
    ndt = strfind(filepiv,'_dt');
    dt = 1e-6*(str2num(filepiv(ndt+3:ndt+7))); % sec
    fid = fopen(filepiv);
    header = fgetl(fid);
    C = textscan(fid,'%f %f %f %f %d','delimiter',','); fclose(fid);
    x = C{1}*respiv - xc; y = C{2}*respiv - yc; u = C{3}*respiv/dt; v = C{4}*respiv/dt; CHC
= C{5};
    n = sqrt(size(x,1));
    X = reshape(x,n,n);
    Y = reshape(y,n,n);
    U = reshape(u,n,n);
    V = reshape(v,n,n);
```

```
   indx2 = find(CHC == -2);
   xp = x(indx2);
   yp = y(indx2);
   up = u(indx2);
   vp = v(indx2);

   hold off

   indx5 = find(CHC == 5);
   Veli = sqrt(u(indx5).^2+v(indx5).^2);
   VelMax(j) = max(Veli(:));
   VelMean(j) = mean(Veli(:));

end

figure,
plot(VelMax/10,'o-b');
xlabel('Image Number)')
ylabel('Maximum Velocity Magnitude (cm/s)')

figure,
plot(VelMean/10,'o-b');
xlabel('Image Number)')
ylabel('Mean Velocity Magnitude (cm/s)')

[mean(VelMean), mean(VelMax)]/10
```

H. <u>MATLAB Code to Generate Turbulence Intensity from PIV</u>

```
clear all; close all; clc;
scrsz = get(0,'ScreenSize');

direct =
uigetdir('D:\PIV_stuff\tween\PIVfiles\cellshear6_vis11cp_fh07mm_rpm030_ls0p5mm_dt350
00us','Select .vec files');
dish_size = 1.5;

if dish_size == 3.0
respiv = (38.1*2)/1694;
xc = (170+round(1694/2))*respiv;
yc = (2048-(200+round(1694/2)))*respiv;
R = 1694/2*respiv;
elseif dish_size == 1.5
respiv = 38.1/1639;
xc = (170+round(1639/2))*respiv;
yc = (2048-(170+round(1639/2)))*respiv;
R = 1639/2*respiv;
end
```

```matlab
directory = strcat(direct,'\*');
if(~strcmp(directory,'\*'))
   [stat,mess] = fileattrib(directory);
end

datfiles = [];
for i=1:size(mess,2)
   filename = mess(i).Name;
   if(strcmp(filename(end-3:end),'.vec'))
      datfiles = [datfiles; i];
   end;
end;
nf = size(datfiles,1);

np = 4;

j = 0;
uMean = []; vMean = []; tkej = []; tkeMean = [];
for i = 1:nf,
   j = j + 1   ;
   filepiv = mess(datfiles(i)).Name;
   ndt = strfind(filepiv,'_dt');
   dt = 1e-6*(str2num(filepiv(ndt+3:ndt+7))); % sec
   nrpm = strfind(filepiv,'rpm');
   rpm = (str2num(filepiv(nrpm(end)+3:nrpm(end)+5))); % sec
   omega=rpm/60*6.2831853;
   fid = fopen(filepiv);
   header = fgetl(fid);
   C = textscan(fid,'%f %f %f %f %d','delimiter',','); fclose(fid);
   x = C{1}*respiv - xc; y = C{2}*respiv - yc; u = C{3}*respiv/dt; v = C{4}*respiv/dt; CHC
= C{5};
   n = sqrt(size(x,1));
   X = reshape(x,n,n);
   Y = reshape(y,n,n);
   U = reshape(u,n,n);
   V = reshape(v,n,n);

   indx2 = find(CHC == -2);
   xp = x(indx2);
   yp = y(indx2);
   up = u(indx2);
   vp = v(indx2);


   indx5 = find(CHC == 5);
   uj = u(indx5);
   ubar = mean(uj(:));
   vj = v(indx5);
   vbar = mean(vj(:));
```

114

```
    tkej = sqrt((u(indx5)-ubar).^2+(v(indx5)-vbar).^2)/(.0095*3.14159265359*2*(rpm/60));
    tkeMean(j) = mean(tkej(:));

end

mean(tkeMean)/10000

figure('Position',[scrsz(1),scrsz(2),scrsz(3),scrsz(4)]),
plot(tkeMean/10000,'o-b');
xlabel('Image Number')
ylabel('Mean Normalized TKV')
axis([0,80,0,0.2])
```

CURRICULUM VITA

NAME: Jonathan Michael D Thomas

ADDRESS: J.B. Speed School of Engineering

             Chemical Engineering Department

             University of Louisville, Louisville, KY, US

DOB: Louisville, Kentucky – July 12, 1984

EDUCATION
& TRAINING: B.S., Chemical Engineering
                         University of Louisville
                         2002-2006

                         M.Eng. Chemical Engineering
                         University of Louisville
                         2006-2007

                         Ph.D., Chemical Engineering
                         University of Louisville
                         2007-2016

AWARDS:

- Engineering Graduate Fellowship, University of Louisville
  Aug 2007 – July 2009
- Teaching Assistant, University of Louisville
  Aug 2009 – Aug 2010

AFFILIATIONS:

- American Institute of Chemical Engineers (AICHE)
- Tau Beta Pi
- Golden Key

- Phi Eta Sigma

PUBLICATIONS:

- **Thomas JMD**, Chakraborty A, Sharp MK, Berson RE. "Comparison Of Computational, Analytical And Experimental Resolution Of Wall Shear Stress In An Orbiting Petri-Dish", Biotechnology Progress, Aug 2010.
- Russ DC, **Thomas JMD**, Miller QS, Berson RE, "Predicting Power for a Scaled-Up Non-Newtonian Biomass Slurry", Chemical Engineering & Technology 38(1), 1-9, (2015).

SELECTED NATIONAL MEETING PRESENTATIONS

- Chakraborty, **Thomas**, Jones, Chakraborty, Jala, Bodduluri, Sharp, and Berson: "Directional Oscillatory Shear Index in Conventional and Novel Culture Dishes", Annual AICHE, Atlanta, GA, November, 2014.
- **Thomas** and Berson: "Closed Loop Waste to Fuel at the University of Louisville" AASHE, Nashville, TN, October, 2013.
- Rezania, **Thomas**, Chakraborty, and Berson: "Mass Transfer in High Solids Biomass Slurries" Annual AICHE, Pittsburgh, PA, October, 2012.
- Rezania, **Thomas**, Chakraborty, and Berson: "Dispersion in a Resonating Acoustic Mixer" Annual AICHE, Pittsburgh, PA, October, 2012.
- Russ, **Thomas**, Miller, and Berson: "Mixing of Lignocellulosics in Stirred Tank Reactors", 33rd Symposium on Biotechnology for Fuels and Chemicals, Seattle, WA, May, 2011.
- Russ, **Thomas**, Miller, and Berson: "Industrial-Scale Mixing of High Solids Biomass Slurries " Annual AICHE, Minneapolis, MN, October, 2011.
- Chakraborty, Thomas, Sharp, and Berson: "Fluid Dynamic Analysis of Flow in Orbiting Dishes" Annual AICHE, Minneapolis, MN, October, 2011.
- **Thomas**, Chakraborty, Shakeri, Sharp, and Berson: "Wall Shear Stress in an Orbiting Culture Dish using CFD with PIV Validation", NAMF Mixing XXII, Victoria, BC, Canada, June, 2010.
- Rezania, **Thomas**, and Berson: "Saccharification of Concentrated Biomass Slurries in a Resonating Acoustic Mixer", 32nd Symposium on Biotechnology for Fuels and Chemicals, Clearwater Beach, Florida, May, 2010.
- **Thomas**, Chakraborty, Sharp, and Berson: "Comparison of Computed and Measured Wall Shear Stress in an Orbiting Cell Culture Dish" Annual AICHE, Nashville, TN, November, 2009.
- **Thomas**, Chakraborty, Sharp, and Berson: "Oscillatory Fluid Shear Stress in Orbiting Dishes and its Effect on Endothelial Cells", Annual AICHE, Philadelphia, PA, November, 2008.